Steam Generator Tube Integrity Program

Annual Report
October 1997 - September 1998

Argonne National Laboratory
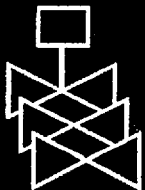
AVAILABILITY NOTICE

Availability of Reference Materials Cited in NRC Publications

NRC publications in the NUREG series, NRC regulations, and *Title 10, Energy,* of the *Code of Federal Regulations,* may be purchased from one of the following sources:

1. The Superintendent of Documents
   U.S. Government Printing Office
   P.O. Box 37082
   Washington, DC 20402–9328
   <http://www.access.gpo.gov/su_docs>
   202–512–1800

2. The National Technical Information Service
   Springfield, VA 22161–0002
   <http://www.ntis.gov/ordernow>
   703–487–4650

The NUREG series comprises (1) brochures (NUREG/BR-XXXX), (2) proceedings of conferences (NUREG/CP-XXXX), (3) reports resulting from international agreements (NUREG/IA-XXXX), (4) technical and administrative reports and books [(NUREG-XXXX) or (NUREG/CR-XXXX)], and (5) compilations of legal decisions and orders of the Commission and Atomic and Safety Licensing Boards and of Office Directors' decisions under Section 2.206 of NRC's regulations (NUREG-XXXX).

A single copy of each NRC draft report is available free, to the extent of supply, upon written request as follows:

Address: Office of the Chief Information Officer
Reproduction and Distribution
 Services Section
U.S. Nuclear Regulatory Commission
Washington, DC 20555–0001
E–mail: <DISTRIBUTION@nrc.gov>
Facsimile: 301–415–2289

A portion of NRC regulatory and technical information is available at NRC's World Wide Web site:

 <http://www.nrc.gov>

All NRC documents released to the public are available for inspection or copying for a fee, in paper, microfiche, or, in some cases, diskette, from the Public Document Room (PDR):

NRC Public Document Room
2120 L Street, N.W., Lower Level
Washington, DC 20555–0001
<http://www.nrc.gov/NRC/PDR/pdr1.htm>
1–800–397–4209 or locally 202–634–3273

Microfiche of most NRC documents made publicly available since January 1981 may be found in the Local Public Document Rooms (LPDRs) located in the vicinity of nuclear power plants. The locations of the LPDRs may be obtained from the PDR (see previous paragraph) or through:

 <http://www.nrc.gov/NRC/NUREGS/
 SR1350/V9/lpdr/html>

Publicly released documents include, to name a few, NUREG-series reports; *Federal Register* notices; applicant, licensee, and vendor documents and correspondence; NRC correspondence and internal memoranda; bulletins and information notices; inspection and investigation reports; licensee event reports; and Commission papers and their attachments.

Documents available from public and special technical libraries include all open literature items, such as books, journal articles, and transactions, *Federal Register* notices, Federal and State legislation, and congressional reports. Such documents as theses, dissertations, foreign reports and translations, and non-NRC conference proceedings may be purchased from their sponsoring organization.

Copies of industry codes and standards used in a substantive manner in the NRC regulatory process are maintained at the NRC Library, Two White Flint North, 11545 Rockville Pike, Rockville, MD 20852–2738. These standards are available in the library for reference use by the public. Codes and standards are usually copyrighted and may be purchased from the originating organization or, if they are American National Standards, from—

American National Standards Institute
11 West 42nd Street
New York, NY 10036–8002
<http://www.ansi.org>
212–642–4900

DISCLAIMER

Steam Generator Tube Integrity Program

Annual Report
October 1997 - September 1998

Prepared by
D. R. Diercks, S. Bakhtiari, K. E. Kasza, D. S. Kupperman,
S. Majumdar, J. Y. Park, W. J. Shack

Argonne National Laboratory
9700 South Cass Avenue
Argonne, IL 60439

J. Muscara, NRC Project Manager

Steam Generator Tube Integrity Program:
Annual Report October 1997-September 1998

by

D. R. Diercks, S. Bakhtiari, K. E. Kasza, D. S. Kupperman,
S. Majumdar, J. Y. Park, and W. J. Shack

Abstract

This report summarizes work performed by Argonne National Laboratory on the Steam Generator Tube Integrity Program during the period October 1997 through September 1998. The program is divided into five tasks: (1) Assessment of Inspection Reliability; (2) Research on In-Service-Inspection (ISI) Technology; (3) Research on Degradation Modes and Integrity; (4) Integration of Results, Methodology, and Technical Assessments for Current and Emerging Regulatory Issues; and (5) Program Management. Under Task 1, progress is reported on the assembly of a steam generator tube mock-up for round-robin studies on currently practiced nondestructive evaluation (NDE) procedures. Progress is also reported on the evaluation of NDE techniques for characterizing the tubes going into the mock-up and on the development of protocols and procedures for the round-robin. In addition, results are reported on the EC inspection of deplugged tubes obtained from the Duke Power Company's McGuire Nuclear Station. Under Task 2, results are reported on numerical and experimental results on the response of a bobbin coil probe to axial notches in calibration-standard tubes. Progress is also reported on the evaluation of multivariate linear and nonlinear models for the correlation of eddy current data with tube structural integrity. In Task 3, progress is reported on the production of cracked tubes for the steam generator tube mock-up. The facility checkout, shakedown, and performance qualification of the Pressure and Leak-Rate Test Facility are described, and the results of initial pressure and leak-rate tests on notched tubes, circular-hole tubes, and tubes containing laboratory-produced stress corrosion cracks are reported. In addition, a series of finite-element analyses was conducted for multiple colinear cracks with various ligament widths, a test matrix was developed for the pressure and leak-rate testing of tubes with axial machined notches, a literature survey is being completed on the current understanding of the mechanisms of the initiation, growth, arrest, and reinitiation of stress corrosion cracks, and the tubes removed from the McGuire steam generators are being decontaminated. Under Task 4, the results of eddy current and ultrasonic examinations of electrosleeved tubes are reported, and residual stresses in these tubes have been measured by neutron diffraction techniques. The results of a critical review of the corrosion and cracking behaviors of electrosleeved tubes are also summarized.

Contents

Figures

Tables

Executive Summary

Assessment of Inspection Reliability

The steam generator (SG) mock-up has been assembled and placed on its platform. Assessment of the first configuration of the SG mock-up tube bundle has been completed. Borescope examinations of all columns were carried out, and minor amounts of debris resulting from the assembly procedure were cleared. Acquisition of bobbin coil and motorized rotating pancake coil data from all 400 columns was completed. A comparison of eddy current (EC) signals from flaws in the mock-up with signals from field flaws indicates that flaw signals are a good representation of field signals.

Eddy current scans of cracks in tubes are being made with various artifacts added (support plate, magnetite, copper, and sludge). Comparisons of (EC) signals from tubes with and without magnetite have been made. Differences in EC signals between clean tubes and tubes with magnetite could be observed. The data are being stored on optical disks for future reference.

The effort to assess the capability for estimating maximum crack depth using a +Point™ coil on Argonne-grown inner-diameter (ID) stress corrosion cracks continued with the destructive analysis of two more tubes. An example of the difficulty of sizing relatively shallow cracks is discussed. The difficulty in sizing cracks is related to relatively poor signal-to-noise ratios and distortion of the EC indications.

Workshops were held with industry experts for the SG nondestructive evaluation (NDE) round-robin exercise. The first workshop was held August 26-27, 1997, and the second was held March 18, 1998. Input was sought from the experts on the protocol and procedures to be used for the round-robin. Following those two meetings, an NDE Task Group was organized to provide input on the Argonne SG mock-up NDE round robin. This group met the last week of September 1998, at Argonne National Laboratory (ANL) to provide input for the development of an inspection plan for round-robin testing of the mock-up.

A meeting was held with Pacific Northwest National Laboratory (PNNL) staff on June 29-30, 1998, to discuss their experience and expertise on the acquisition and analysis of round robin data. The topics included evaluation of detection, sizing data, test design, receiver operating characteristic (ROC) analysis, errors in regression analysis, and specific problems related to SG round-robins. Technical discussions also covered (a) objectives for probability of detection (POD) confidence limits, (b) placing of artifacts on tubes, (c) number of flawed tubes that need to be destructively analyzed to have confidence in estimates of true state, and (d) the extent to which copper needs to be plated on test sections.

A significant effort has been made to establish the accuracy of profiling deep cracks. Some of the axial outer diameter (OD) profile data were used to correctly predict the failure of tubes in the Pressure and Leak-Rate Test Facility at ANL.

Eddy current signals from deplugged tubes of retired steam generator D at the Duke Power McGuire nuclear station were compared with signals from previous inspections (December

1995 and August 1994). In all cases, the bobbin coil voltages increased with time. Factors that could result in increased EC voltage include crack growth, wider crack opening, or a change in deposits. In addition, as a result of the presence of new signals from probes similar to those used before and the availability of new +Point™ data (not taken during the previous inservice inspection), new crack calls from relatively small EC signals were made. A review of some earlier EC data indicated that these new calls would not have been made with the data available during previous inspections. The preliminary conclusion is that new calls made on the deplugged tubes would not have been made previously because (a) the EC signals appeared after the December 1995 ISI or (b) the EC signals were too small to be called flaw indications with the probes used at that time but have grown enough to be detectable now.

While the amplitude of the EC signal may change for reasons other than crack growth, the change in length of the indication is more likely to be related to actual change in crack length. The length change of the crack in R39 C46 has been estimated. Analysis of the data suggests that the crack lengthened somewhat during the time the tube was plugged.

Research on ISI Technology

Studies carried out under Task 2 have been concerned primarily with electromagnetic (EM) modeling and data analysis. Numerical and experimental results are first presented in Section 3.1 on the response of bobbin coil probes to axial notches in calibration-standard tubes. Section 3.2 deals with the continued evaluation of multivariate linear and nonlinear models for the correlation of EC readings with tube structural integrity.

Bobbin coil probe responses from reference indications commonly used to calibrate EC NDE results were analyzed by using EM modeling. Single-point calculations were carried out earlier to determine absolute bobbin coil output voltage from drilled holes and axial notches of various sizes. Results have been updated to include full-length calculations for the differential coil configuration on a more limited set of flaw lengths. Experimental data have also been presented to verify the theoretical findings. All test cases pertain to bobbin coil response at two frequencies that represent the usable lower and upper bound for inspection of 22.2-mm (0.875-in.)-diameter Alloy 600 tubing. Based on the results of this study on ideal flaw geometries, some basic inferences are made regarding the expected probe sensitivities to realistic flaws and on the use of holes and notches for the calibration of EC readings.

Results are also provided on the evaluation of linear and nonlinear multivariate analysis techniques for construction of models to better describe potential relationships between EC signals and tube structural integrity. This study utilizes bobbin coil data from selected model boiler and pulled tube specimens from the alternate repair criteria (ARC) data base on the outer diameter stress corrosion cracking (ODSCC) mode of degradation at tube support plate (TSP) intersections. Analyses of these limited data set suggest that a renormalization procedure based on independent energy scaling of the inspection results may improve the overall correlation between EC indications and tube failure pressure when the sample set includes both laboratory-grown and field-induced flaws.

Finally, comparative studies with multiple linear regression and neural network models using the same data set are presented. The results generally indicate comparable prediction accuracy for the two multivariate analysis techniques. However, the performance of more

elaborate nonlinear models such as neural networks (compared to that of conventional multiple linear regression techniques) is expected to improve with the incorporation of a larger number of test specimens into the training sample set.

Research on Degradation Modes and Integrity

Laboratory-induced cracking has been produced in hundreds of 22.2-mm (7/8-in.)-diameter Alloy 600 tubes under accelerated (chemically aggressive) conditions. Some of these cracked tubes will be used to evaluate NDE equipment and techniques for the SG tube mock-up and for pressure and leak-rate testing. The stress corrosion cracks produced in these tubes have six different basic configurations, namely circumferential cracks at the inner and outer (ID and OD) surfaces, axial cracks at the ID and OD, and skewed cracks at the ID and OD. In some cases, multiple and segmented cracks have been produced. The cracks are detected by visual inspection and confirmed by nondestructive EC tests. Additional facilities for the production of laboratory cracks were also designed and constructed.

The Pressure and Leak-Rate Test Facility was completed during this reporting period and underwent extensive checkout, shakedown, and performance qualification testing; testing on actual flawed tubes began in May 1998. The facility can operate at temperatures up to 343°C (650°F), pressures up to 21 MPa (3000 psi), and pressurized-water flow rates up to 1520 L/min (400 gal/min). The facility incorporates several features necessary to obtain prototypical data under stable, controlled conditions. Safe control of facility pressure and temperature was verified under conditions of both a step change and a gradual change in leak flow rate over the range 0-760 L/min (0-200 gpm) with at most a <1% rise above the desired set point at pressure set point levels ranging from 0-19 MPa (0-2800 psi) for room and elevated temperature operation.

An initial series of tests was conducted on 22.2-mm (7/8-in.)-diameter Alloy 600 tubes with sharp-edged circular orifice throughwall holes using room- and high-temperature water. These tubes had hole diameters of 6.35 mm (1/4 in.), 3.175-mm (1/8 in.), and 0.794 mm (1/32 in.). The observed leak rates at room temperature were 216, 56.0, and 2.76 L/min (57.0, 14.8, and 0.73, 14.8, gpm), respectively, for a nominal differential pressure of 17.2 MPa (2500 psi). The 3.175-mm-diameter hole at 17.2 MPa (2500 psi) exhibited an average jet velocity of 112 m/s (366 ft/s). These high jet velocities can produce significant lateral thrust, and the 3.175-mm (1/4-in.)-diameter hole specimen was bent ≈10° from its axis as a result of this thrust. The two other specimens with smaller-diameter holes leaked at lower flow rates at this same pressure and hence were subjected to lower jet thrust, resulting in no observable bending.

The flow rate through the 3.175-mm (1/8-in.)-diameter hole in a test using 282°C (540°F) water was compared with that observed at room temperature. A standard correlation for a sharp-edged circular orifice was found to predict both the room- and elevated-temperature flow rate quite well for a discharge coefficient C of 0.6. In addition, three tubes with geometrically identical 38.1-mm (1.5 in.)-long, 0.20-mm (0.0075-in.)-wide 80% TW axial OD EDM flaws were tested at room temperature. Two of these tubes had the same as-received heat treatment and provided a check on data reproducibility, and the remaining tube was sensitized (solution-heat-treated at 1100°C for 10 min. and aged at 600°C for 48 h) prior to testing to evaluate the influence of this heat treatment on flaw failure behavior. The sensitized tube exhibited a

reduced failure pressure, an increased flow area, and a larger hole after failure. The heat treatment used to promote SCC thus weakens the tubes and changes their leak and rupture characteristics somewhat.

Tests were also conducted on four Alloy 600 tubes with laboratory-produced tight axial ODSCC of nominal length 12.7 mm (0.5-in.). These tests were designed to gain information on flaw stability under the constant temperature and pressure conditions associated with normal SG operation and main steam line break conditions. These pressure plateaus were held for at least 2 h (depending on the leak rate and the amount of water in the blowdown vessel), with extended duration holds at intermediate pressures if flaw tearing, as indicated by a sudden increase in flow, was observed. Two tubes were tested at room temperature and the remaining two tubes at 282°C.

All four SCC flaws had one or two subregions of pretest throughwall penetration (pinholes) as determined by bubble testing. However, none of the flaws exhibited detectable water leakage at pressures below 8.3 MPa (1200 psi) or during the 2-h (or greater) hold times at 8.3 MPa. Flaws in three of the four tubes exhibited crack ligament tearing under constant temperature and pressure conditions, resulting in increasing leak rates under constant pressure. Posttest inspection revealed that flaws in three of the tubes opened significantly in width along their entire length, even into the extremities of the Y branches at each end of the main flaw. This opening occurred at pressures of <17.2 MPa (2500 psi) and resulted in flow rates of 23-38 L/min (6.0-10.0 gpm) or more. The fourth tube, for which the EC amplitude of ≈4 V was considerably lower, opened only slightly and exhibited a leak rate of 1.66 L/min. (0.44 gpm). Additionally, the first three three tubes had several posttest secondary cracks emanating from the main crack pattern, and the region around the flaws was raised noticeably (puckered). The flaw with the lower EC voltage did not exhibit this behavior.

A series of finite-element analyses was conducted for multiple collinear cracks with various ligament widths to develop a test matrix for specimens with complex cracks that will be tested in the Pressure and Leak-Rate Test Facility. Ligament failure pressures were 15.5. 19.0, and 29.0 MPa (2.25 ksi, 2.75 ksi, and 4.2 ksi) for ligament widths of 1.27, 2.54, and 6.35 mm (0.05, 0.1, and 0.25 in.), respectively. For ligament widths ≥6.35 mm (≥0.25 in.), each of the two 12.7-mm (0.5-in.)-long cracks fail unstably at a pressure 29.0 MPa (4.2 ksi), i.e., the two cracks do not interact.

A test matrix for specimens with a single axial machined flaw has been developed for leak and failure testing. In addition, a literature survey is being prepared on our current understanding of mechanisms of initiation, arrest and reinitiation of stress corrosion cracks in PWR steam generator. More than 200 publications have been reviewed for the initial draft report to be published in June 1999.

Portions of 11 individual tubes were pulled from McGuire Unit 1 steam generator D, as were two tube sheet samples containing 8 and 12 tubes, respectively. Two TSP sections containing ≈45 and ≈25 tube intersections, respectively, were also removed from the first TSP level of steam generator B. These samples arrived at ANL on December 4, 1997, and were placed in special storage because of their relatively high radiation field. Additional shielding was added to the glovebox where decontamination and sample handling were to be carried out, and the glovebox ventilation system was upgraded.

Decontamination of the McGuire tubes was then initiated. Initial attempts using liquid detergent and water were unsatisfactory, and a commercial decontamination solution was subsequently employed. After extended treatments with this solution, satisfactory results were achieved. As expected, the levels of fixed contamination on the tubes is reduced only slightly by the decontamination procedure, but the level of loose contamination is typically reduced by a factor of 100 or more. Decontamination of the McGuire tubes is continuing.

Development of Methodology and Technical Requirements for Current and Emerging Regulatory Issues

Eddy current and ultrasonic examination of electrosleeved tubes with electrodischarge machined (EDM) notches has been carried out at ANL. This study is being used to help assess the capability of ultrasonic techniques, in comparison to that of EC techniques, to detect and characterize defects in tubes repaired by the electrosleeving process. This effort is necessary to determine the adequacy of detection when a crack does not intersect the parent tube OD to form a strong ultrasonic reflector. Higher-angle-beam ultrasonic (UT) NDE, including use of surface waves, should be explored for detection of cracks that do not form corner reflectors.

Argonne's Pulsed Neutron Source has been used to estimate fabrication-induced residual stresses in the sleeve and parent material of an electrosleeved Alloy 600 flaw-free 30-cm (12-in.)-long 22.2-mm (7/8-in.)-diameter tube. Compressive hoop and axial residual stresses approximately 100 MPa (15 ksi) in magnitude, with relatively large uncertainties, were calculated from strain measurements for the Alloy 600 parent tube material. Tensile residual stresses of $\approx$100 MPa (15 ksi) were calculated for the nickel sleeve material with similar uncertainties. Although these stresses are relatively small, they could have an effect (although perhaps small) on fatigue strength.

An experiment with an electrosleeved tube was carried out to answer the question of whether a normal-incidence longitudinal ultrasonic wave would reflect off the electrosleeve parent-tube interface. A detectable echo from the interface would allow sleeve thickness to be determined and provide a reference for characterizing the depth of detectable cracks in either the parent tube or electrosleeve. The reflection coefficient at the nickel/Alloy 600 interface is $\approx$5%, and as a result the echo from the Ni/Alloy 600 mismatch would be extremely difficult to detect. Experiments with normal-incidence longitudinal ultrasonic waves at $\approx$10-15 MHz showed no discernible echo from the interface. Sophisticated signal processing and deconvolution techniques would have to be applied to the ultrasonic data to reveal echoes from the Ni/Alloy 600 interface.

A comprehensive critical review of the corrosion and cracking behaviors of tubes repaired by the electrosleeve process was completed during the reporting period. It was concluded that there are substantial data and experience to indicate that Ni, and the nanophase Ni electrosleeve material in particular, are highly resistant to corrosion and SCC in a variety of environments. However, the variety and complexity of environments on the secondary side of steam generators makes it very difficult to assert with a high degree of certainty that these materials are immune to cracking in all of these environments.

Acknowledgments

Acronyms and Abbreviations

ABB	ASEA Brown-Boveri
ANL	Argonne National Laboratory
ARC	alternate repair criteria
ASME	American Society of Mechanical Engineers
BC	bobbin coil
BCL	Battelle Columbus Laboratories
CDS	computerized data screening
COA	crack opening angle
CODSCC	circumferential outer-diameter stress corrosion crack/cracking
DAS	data acquisition system
DE	destructive examination
EC	eddy current
EDM	electrodischarge machining
EM	electromagnetic
EPRI	Electric Power Research Institute
FBH	flat-bottom hole
FEA	finite-element analysis
FEM	finite-element method
FTI	Framatome Technologies, Inc.
ID	inner diameter
IDSCC	inner diameter stress corrosion cracking
IGA	intergranular attack
IGSCC	intergranular stress corrosion cracking
INEEL	Idaho National Engineering and Environmental Laboratory (formerly Idaho National Engineering Laboratory, or INEL)
IPNS	(Argonne) Intense Pulsed Neutron Source
ISG-TIP-2	International Steam Generator Tube Integrity Program—2
ISI	in-service inspection
LODSCC	longitudinal outer-diameter stress corrosion crack/cracking
LOOT	leave-one-out training
LS	least squares
MAI	multiple axial indication
MAWP	maximum allowable working pressure
MLR	multiple linear regression
MRPC	motorized rotating pancake coil
MSLB	main steam line break
NDE	nondestructive evaluation
NN	neural network
NRC	U.S. Nuclear Regulatory Commission
OD	outer diameter
ODSCC	outer-diameter stress corrosion crack/cracking
PLS	partial least squares
PNNL	Pacific Northwest National Laboratory
POD	probability of detection
PWR	pressurized water reactor

PWSCC	primary-water stress corrosion cracking
ROC	receiver operating characteristic
RR	round-robin
RT	room temperature
SCC	stress corrosion cracking
SG	steam generator
S/N	signal-to-noise ratio
SS	stainless steel
SSE	site-specific examination
TGSCC	transgranular stress corrosion cracking
TS	tube sheet
TSP	tube support plate
TTS	top of tube sheet
TW	throughwall
UT	ultrasonic testing

1 Introduction

The objective of this program is to provide the experimental data and predictive correlations and models needed to permit the U.S. Nuclear Regulatory Commission (NRC) to independently evaluate the integrity of steam generator (SG) tubes as plants age and degradation proceeds, new forms of degradation appear, and new defect-specific management schemes are implemented. The areas addressed by the program include assessment of procedures and equipment used for in-service inspection (ISI) of SG tubes, and recommendations for criteria and requirements to improve the reliability and accuracy of ISI; validation and improvement of correlations and models that are used to evaluate integrity and leakage of degraded SG tubes; and validation and improvement of correlations and models that predict the generation and progression of degradation in SG tubes as a function of aging, including the effects of the operational environment such as temperature, dry-out and concentration conditions, stresses, and primary- and secondary-side water chemistry.

The studies in this program focus primarily on Alloy 600 SG tubing in the mill–annealed condition, because this tubing material is (and will be) present in plants where SGs have not been replaced and because it is more susceptible to cracking than replacement materials such as thermally treated Alloy 600 or 690. Although most SGs that use mill–annealed Alloy 600 will probably require eventual replacement, the behavior of this material will be of concern for many more years. Thermally treated Alloy 600 and 690 will also be tested. Although these alloys are expected to be much less susceptible to degradation than mill–annealed Alloy 600, we must still be able to predict their behavior.

The bulk of the materials used in the program will be exposed to simulated operating conditions and more aggressive environments representing accelerated conditions during laboratory testing. Because of the necessity to use accelerated conditions and because service degradation, tubing conditions, and in-service operating and inspection conditions cannot always be faithfully represented in laboratory conditions and specimens, this program has obtained and will use service-degraded tubing for correlation with and validation of experimental data, integrity and degradation predictive models, and inspection capability. Comparisons are being made with the morphology and character of service–degraded flaws to help ensure that the flaws produced in the laboratory and used for studies on inspection reliability, pressurization, and leak-rate testing will be as realistic as possible. The reliability of flaw detection and accuracy of flaw sizing data will be assessed by typical ISI personnel, procedures, and equipment.

This program is divided into four technical tasks and one management task:

1. Assessment of Inspection Reliability,

2. Research on ISI Technology,

3. Research on Degradation Modes and Integrity,

4. Integration of Results, Methodology, and Technical Assessments for Current and Emerging Regulatory Issues,

5.   Program Management.

This annual report describes program activities and results from October 1997 through September 1998.

2   Assessment of Inspection Reliability (D. S. Kupperman and S. Bakhtiari)

The objective of the inspection task is to evaluate and quantify the reliability of current and emerging inspection technology for current-day flaws, i.e., establish the probability of detection (POD) and the capability to accurately size cracks.   Both eddy current (EC) and ultrasonic testing (UT) techniques will be evaluated.   The results of the NDE will be validated by inspection and destructive evaluation of service-degraded tubing.

A steam generator mock-up is being assembled for round-robin (RR) studies using currently practiced techniques and commercial teams.   The mock-up will also be used as a test bed for evaluating emerging technologies for the ISI of SG tubes.   The RR test will include both EC and UT methods.   Teams will report the flaw types, sizes, and locations, as well as other commonly used parameters such as voltage responses from the EC tests.

2.1 Steam Generator Tube Mock-Up Facility

2.1.1   Tube Bundle

The SG mock-up has been assembled in its initial configuration and placed on its platform (Fig. 2.1), and the assessment of this first configuration was completed.   As a result of this assessment, the mock-up design was modified somewhat, and the configuration shown schematically in Fig. 2.2 will be used for the RR tests.   A key modification was the addition of a third tube support plate (Level I).   The mock-up will be upgraded by the addition of more flawed tubes and artifacts (magnetite, sludge, and some copper).

In assessing the initial configuration of the mock-up, borescope examinations of all columns were carried out.   Polyethylene shavings from the divider plates that were produced during assembly interfered somewhat with the movement of the probes in several cases.   A tool was made to remove the shavings generated during the assembly.   In addition, slight tube misalignments were discovered and corrected with a specially designed tool.   Bobbin coil and motorized rotating pancake coil (MRPC) probes then moved smoothly through all but two of the 400 columns.   Those two columns showed significant resistance to movement of a bobbin coil resulting from misalignment of the four tubes between the top two levels H and I.   This misalignment required the mock-up to be dismantled so that the misaligned test sections could be adjusted for smooth probe travel.   Eddy current signals from flaws and artifacts taken with the tube bundle assembled were as expected.

Acquisition of bobbin coil and MRPC data from all 400 columns was completed.   A comparison of EC signals from flaws in the mock-up with signals from field flaws indicates that flaw signals are a good representation of field signals.   All EC data, including +Point™ data, were accumulated with two in-line standards: an ASME standard with simulated tube
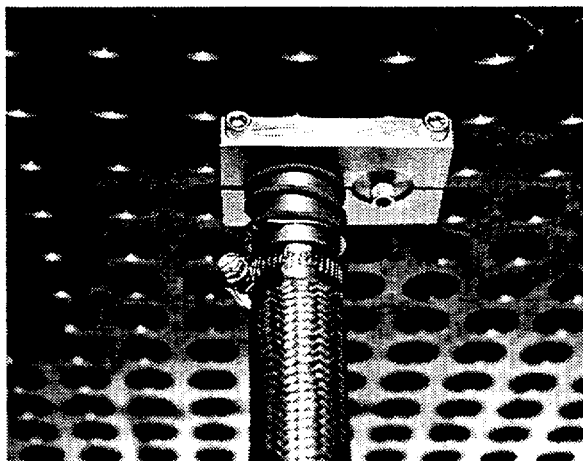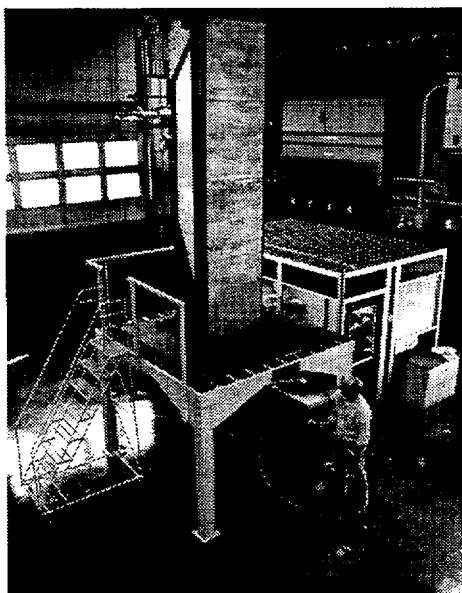
Fig. 2.1.   *Steam generator mock-up on stand (top), and view from underneath (bottom) showing conduit with eddy current probe connected to base plate.*

Back plate:
Carbon steel
(Drwng SGT17)

Carbon steel tubes,
914-mm (36-in.)-
long, 19.68-mm
(0.775-in.)-ID

Mechanical
slip fit
for Alloy 600
tubes

I

H

G

F

E

D

C

B

A

Polyethylene
plate

Alloy 600, 22.2-mm
(7/8-in.)-diameter
tube sections (3600)
are 305-mm(12-in.)
-long

Tube support plates:
Carbon steel
22.2-mm (3/4-in.)-
thick (Drwng SGT11)

Divider plates (9):
Polyethylene
22.2-mm (3/4-in.)-
thick (Drwng SGT13)

Spacer plate: Aluminum
6.3-mm (1/4-in.)-thick (Drwng SGT18)

Simulated tube
sheet 152-mm
(6-in.)-
carbon-steel-
collar, over
Alloy 600 tube]

Eddy current
probe

Tube bundle base plate: Carbon steel
12.7-mm(1/2-in.)-thick(Drwng SGT15)

Tube bundle support plate: Carbon steel
25.4-mm (1-in.)-thick

Fig. 2.2. *Schematic diagram of mock-up tube bundle (total height 3.7 m [12 ft]).*

support plate (TSP) and a standard with 18 axial and circumferential ID and OD notches. These data were stored on an optical disk for future reference. In addition, Eddynet95 software, multiparameter regression analysis, and neural network software programs will be used to analyze flaw data from the mock-up. This initial effort with the assembled mock-up has provided significant information that will help in the preparation of the final version of the RR protocol. This exercise has also resulted in some modification of the fixtures used to insert the probes in order to improve data acquisition speed.

2.1.2 Artifacts

A significant effort has been made to reproduce the EC signals and distortions from artifacts found in the field. For example, several schemes for simulating magnetite in the tube bundle have been assessed. Tests have been carried out with (a) magnetite applied to the tube support plate (TSP) area in the form of a paste, (b) magnetite packed into the crevice as a loose powder, (c) a ferrofluid (magnetite suspended in a fluid) in the crevice, and (d) the use of magnetic video tape wrapped around the tube in the crevice. The ferrofluid easily fills the crevice, which is then sealed at both ends with a putty-like material. Comparisons of EC signals from tubes with and without magnetite have been made. Based on the results of these evaluations, magnetite in the crevices will be simulated primarily by the use of magnetic video tape, although ferrofluid will be used in some crevices.

Small differences in EC signals between clean tubes and tubes with magnetite could be observed. In addition, rings cast with a material simulating sludge (copper and magnetite) have being fabricated. Eddy current scans of cracks in tubes are being made routinely with various artifacts added (support plate, magnetite, copper, and sludge). An example of how the artifacts affect the EC Lissajous figure from a bobbin coil is shown in Fig. 2.3. The Lissajous figure varies for a notch as the scans are made with (a) no artifact, (b) magnetite, (c) copper ring, (d) ferrite ring, and (e) sludge ring. The data are being stored on optical disks for future reference.

A device for denting tubes has been provided by Framatome Technologies, Inc. (FTI). The denting device continues to be used to make dents in heat-treated test sections. The deformations from the dents range from one to nine mils, with dent voltages ranging from a few tenths of a volt to several volts when scanned with a bobbin coil. Cracks will be grown through the dents following EC examination of the test sections.

Progress has been made in the effort to copper plate Alloy 600 test sections. The use of copper sulfate at a few hundred degrees Fahrenheit with the Alloy 600 tube immersed in solution and an iron rod in contact with the tube leads to a visible thin copper film. Efforts to copper plate Alloy 600 test sections continue, as progress to date has not been entirely satisfactory.

The idea of using epoxy markers at the end of each test section to allow unambiguous indication of circumferential position has been tried. Clear signals were generated if the epoxy is at least 1 in. from the end of the tube. No obstruction of the probes was noted when small epoxy markers were present. A special tool has been designed to clear epoxy that causes restriction of movement of the bobbin or pancake probes.
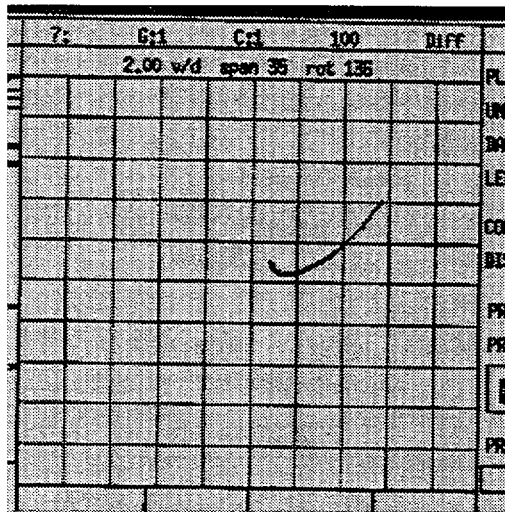
(a)
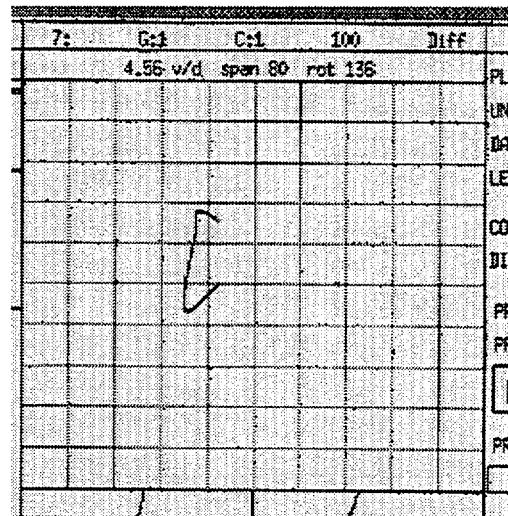
(b)
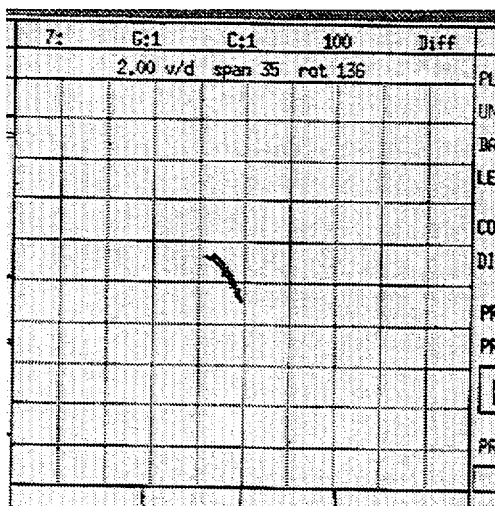
(c)
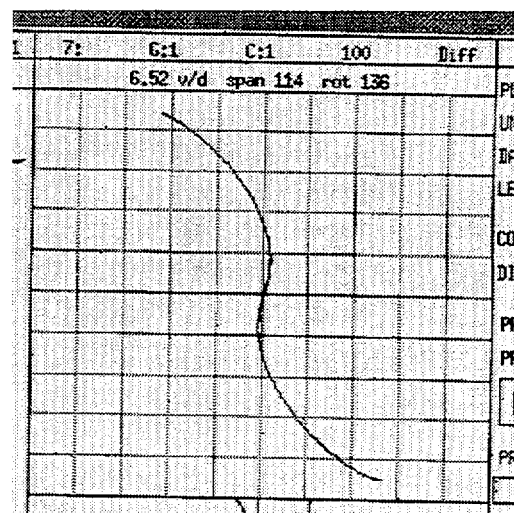
(d)

Fig. 2.3. Variation in differential bobbin coil Lissajous figures from axial OD notch (at 100 kHz) with (a) no artifact, (b) magnetite ring, (c) copper ring, and (d) ferrite ring.

A mixture of magnetite and copper make up the sludge simulation. All of the flaw-free test sections at the tube sheet level of the mock-up require sludge as an artifact. The preparation of these test sections has been completed.

The effect on the EC signal from oxide coatings on crack surfaces was assessed by examining (before and after oxide coating was present) five test sections with cracks prepared at Argonne. Morphology and depth of the cracks varied. The test sections were examined with an MRPC probe. Variations in EC signal resulting from this initial effort to produce an oxide coating appear to be small, if present at all. Figure 2.4 shows the 3-D map of the EC signal
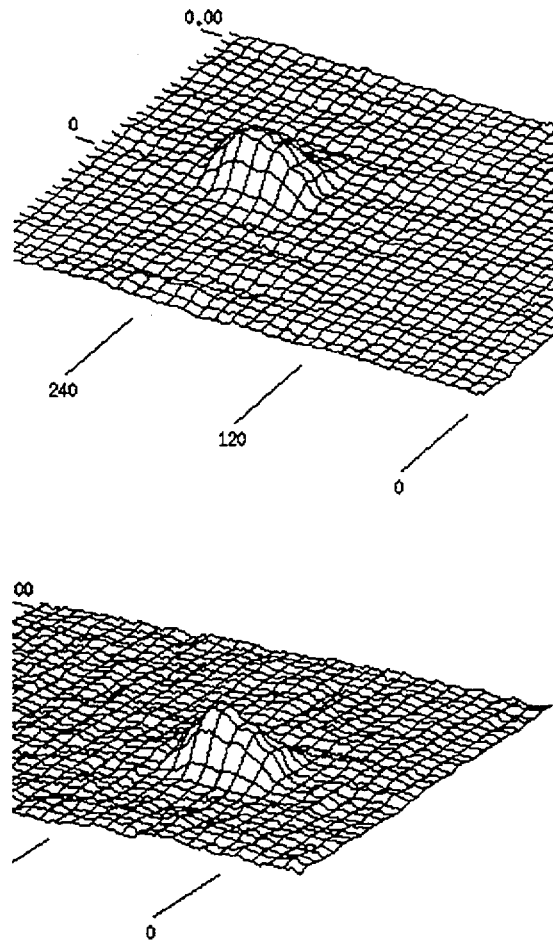
Fig. 2.4.   *Comparison of 3-D presentations of eddy current signal from +Point Coil at 300 kHz for OD circumferential crack in Alloy 600 test section without (top) and with (bottom) a small amount of oxide coating. Change in eddy current signal from presence of coating, if any, are slight.*

amplitude as a function of position from a +Point coil at 300 KHz for an OD circumferential crack. The shape of the EC signal profile is essentially the same. The phase angle also showed only a small (<5°) shift as a result of the oxidation treatment, with the shift being in the direction of an apparently very slightly deeper indication. Similar results were found for the other four cracked test sections. A planned longer exposure should result in the corroding of contacts between the faces of the cracks, leading to an increase in EC signal. For that test, Alloy 600 tubes with axial ODSCC will be placed under PWR water chemistry (300°C and oxygen at the ppb level) for about two months.

Part of the plan to carry out the round robin involves the preparation of a color-coded flaw map indicating the proposed locations for flawed test sections and artifacts. The initial map has been completed. A separate sheet is provided for each of the nine tube bundle levels.
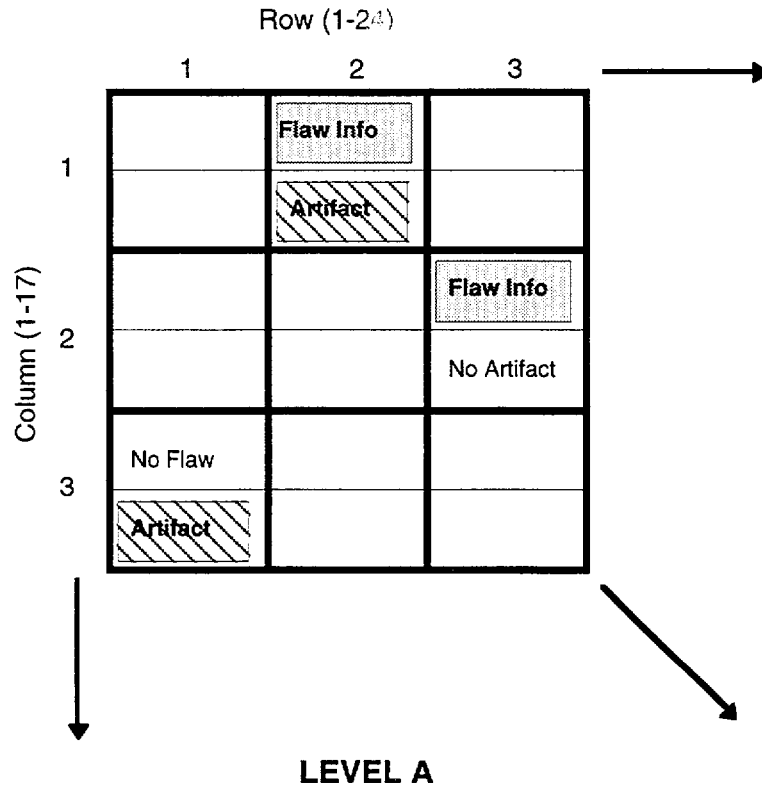
Fig. 2.5. *Schematic representation of section of flaw map at specified level "A" (one of nine levels, A through I).*

Each level contains 400 30-cm (12-in.)-long Alloy 600 test sections. Each test section is represented by a box, with the color-coded flaw information in the top half and the color-coded artifact information in the lower half (Fig. 2.5). In addition, a separate color-coded sheet has been made for each row. These sheets allow each tube (consisting of the nine test sections through which a probe passes) to be represented, enabling one to observe the flaws and artifacts the probe should "see" as it moves through the nine levels of a tube as it traverses from the bottom to the top of the mock-up (Fig. 2.6).

2.1.3 Flaw Sizing

The effort to assess the capability for estimating maximum crack depth using a +Point™ coil on ANL-grown stress corrosion cracks (SCC) continued with the destructive analysis of more tubes. Although good success has been achieved in estimating the maximum depth of IDSCC for cracks greater than 60% TW, shallow cracks are difficult to size. An example of the difficulty of sizing relatively shallow cracks is presented here. The Lissajous figure at 200 kHz for a crack estimated by destructive analysis to be 34% throughwall (TW) is shown in Fig. 2.7a. The phase angle (for maximum depth) is very close to that for a 20% TW axial ID electrodischarge-machined (EDM) notch (Fig. 2.7b). As a result, the crack is undersized. This analysis was carried out on a clean tube (no artifacts) with +Point™ at 200 kHz, but the result

To Top of Mock-up

ROW 1

Level (A - I)

C

B

A

No Flaw

Artifact

1   2   3

Column (1-17)
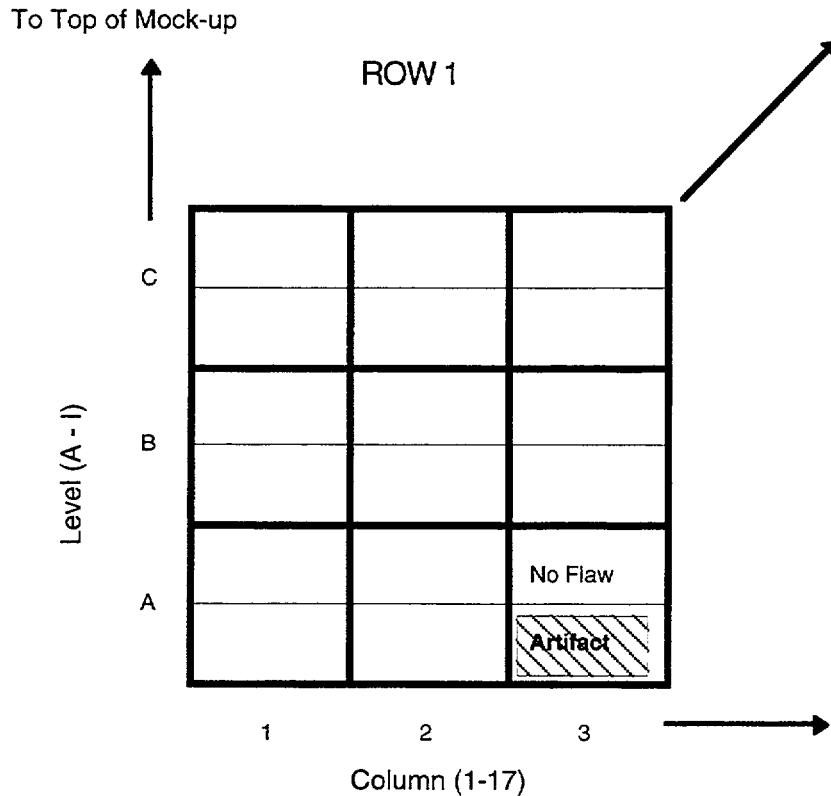
Fig. 2.6.   *Schematic representation of section of mock-up at specified*
row "1" (one of 24 rows).

at 400 kHz was similar. The difficulty in sizing cracks is related to relatively poor signal-to-noise (S/N) ratios and distortion of the eddy currents. In addition, as can be seen in the selected segments of Fig. 2.7 (indicated by the dotted lines), the amplitude of the 20% TW notch is much greater than that of the 34% TW crack. The isometric plot at 200 kHz is shown in Fig. 2.8.

2.2 Round-Robin Protocol and Procedures

2.2.1   Round-Robin Workshops

Two workshops were held with industry experts to discuss the steam generator NDE RR exercise. The first workshop was held August 26-27, 1997, and the second was on March 18, 1998. Input was sought from experts on the protocol and procedures used in actual field inspections. We needed input to be assured that the RR is carried out with procedures as close as possible to those used in the field. Representatives from Zetec, FTI, EPRI, Duke Power, Northern States Power, Aptech, Westinghouse, PNNL, and the NRC attended the workshops. Key items for discussion were procedures, reporting requirements, information to be provided to participants, important parameters in artifact simulations, handling of human factors, standards to be provided, possibility of special inspections for specific flaws, sizing, destructive analysis, and requirements for participating teams.

34% TW LIDSCC
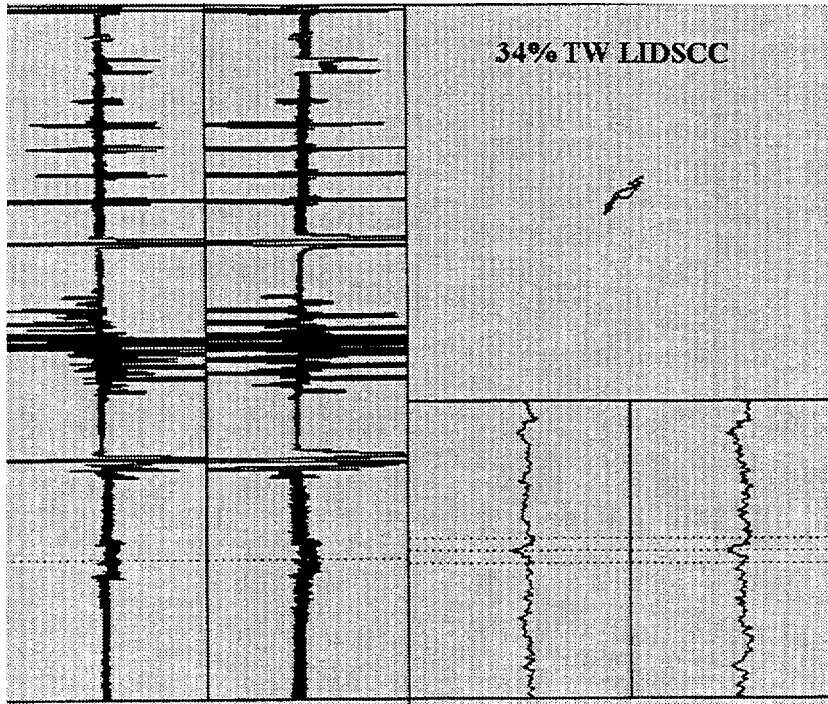
Fig. 2.7a. *Lissajous figure for +Point™ coil at 200 kHz for crack estimated from destructive analysis to be 34% TW.*

20% TW ID Axial EDM Notch
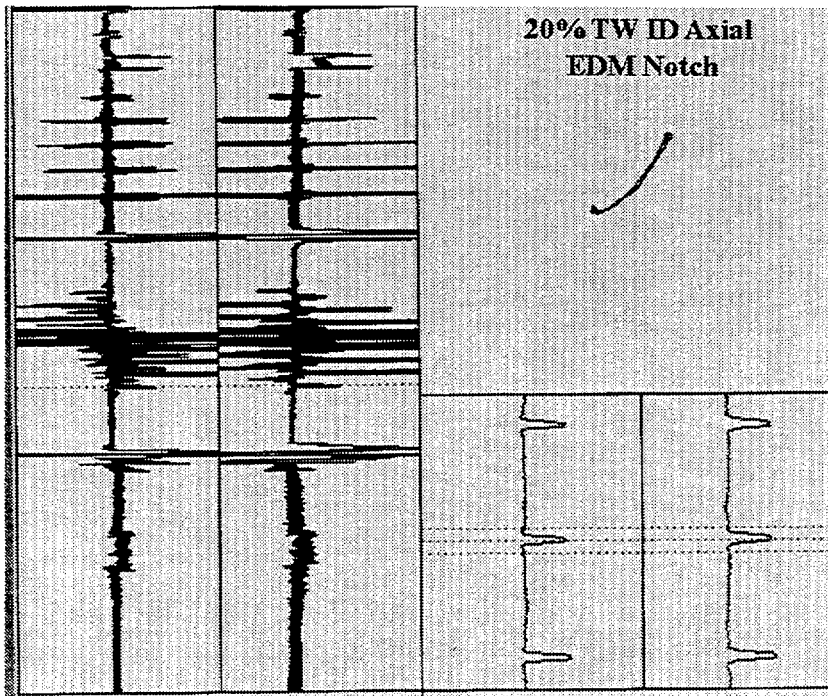
Fig. 2.7b. *Lissajous figure for +Point™ coil at 200 kHz for 20% TW axial ID EDM notch.*
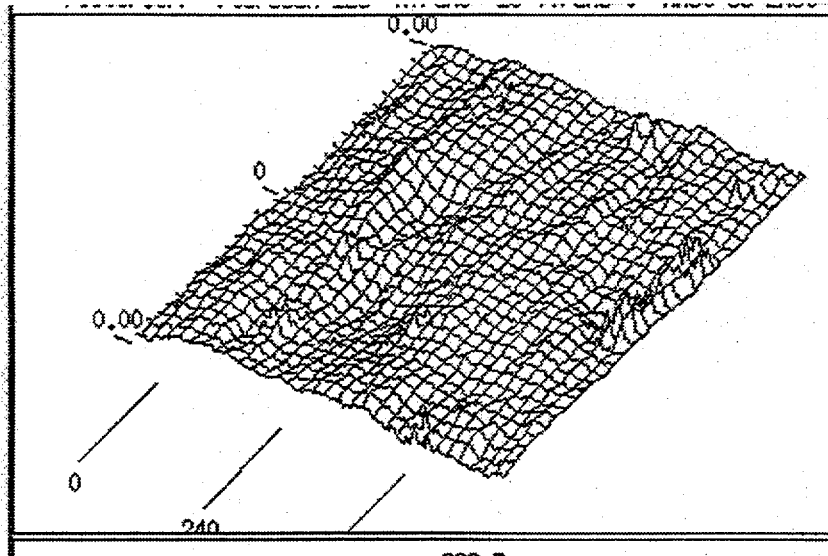
Fig. 2.8.   *Isometric (c-scan) using +Point™ coil at 200 kHz for tube with axial IDSCC (shown in Figs. 2.4a and b). Axis of tube extends from lower left toward upper right.*

Written and verbal comments regarding the RR protocol workshop were received in response to our request for input. Many of the items of interest are discussed below. The items below are divided into opinions by industry experts and conclusions and decisions made for the program.

Opinions expressed by industry experts:

1. Industry experts expressed the opinion that they should provide input on the protocol and procedures of the RR in order to derive the maximum benefit from the exercise.

2. Several industry experts suggested that because of the numerous existing ISI procedures, a generic procedure for the mock-up be prepared rather than using an existing procedure for a specific nuclear steam generator.

3. Several industry experts expressed the opinion that the mock-up inspection plan be based on information regarding damage mechanisms and the tube bundle geometry. If information on types and locations of tube bundle defects is limited, a bobbin coil (BC) examination followed by a +Point™ exam of selected sites would not be sufficient. An extensive inspection would be required (e.g., 100% +Point™) under those conditions.

4. Several industry experts suggested that primary and secondary analysts be evaluated separately and then in combination with resolution analysts (possibly two operating as a team). Computerized data screening (CDS) as a secondary analyst could be used on the mock-up with some modification of the existing commercial software.

5. Some industry experts expressed the opinion that a training procedure and a site-specific examination (SSE) be prepared for the participants in the RR (similar to that provided before field examinations). This would simulate the field practice of providing examples of

defects that are expected at the specific plant site. Training could be carried out by using raw data stored on an optical disk.

6. Industry experts expressed the opinion that the RR protocol incorporate the PWR Steam Generator Examination Guidelines: Revision 5, along with training and site-specific exams (SSE). They also suggested that the SSE be carried out using EC data on an optical disk with examples of the different kinds of flaws in the mock-up. The data on this disk could be supplemented with field data. Data from the 20-tube set that is a subset of mock-up test sections could provide some examples of what is in the mock-up tube bundle. Those tubes were examined and destructively analyzed to establish a correlation between NDE and metallographic results. Other examples from mock-up test specimens could also be used, as long as there is no indication of the flaw location.

8. Industry experts discussed which standards might be used for inspection of the mock-up, expressing the opinion that standards with roll transitions or dents may not be required because of the large signals and familiar conditions. Reproducing sludge can be done by using magnetite and copper.

9. An opinion was expressed by the industry experts that if only one acquisition procedure is used, EC data could be collected once and analyzed by several teams independently.

10. Several industry experts recommended that after mock-up inspections are completed, tubes could be tested under pressure to determine the failure-initiating defect. The profile of the failure initiating crack could be determined from fractographic examination after failure. This approach helps to avoid some of the problems associated with interpreting a series of metallographic cross sections.

11. One industry expert suggested that the ends of the test sections in the mock-up tube bundle be notched, or marked in some way, to provide a circumferential reference to aid in correlating NDE to destructive examination results.

12. One industry expert suggested that a valuable result of the RR would be to learn how effective the resolution analyst feedback is. It was also suggested that one benefit of the RR might be the ability to separately evaluate technique and personnel capability.

After discussions between ANL staff and the NRC program manager related to the above items, the following conclusions and decisions were made for the program:

1. Results will be reported in terms of POD vs. maximum depth, length, and average depth. While profiling is very time-consuming and expensive, some tubes will be pressure-tested to provide some information on crack depths and profiles from examination of the failed tubes.

2. The shakedown of the mock-up and RR procedures will be carried out by a small group of NDE industry experts who volunteered for this task. This shakedown effort would eliminate problems propagating through the entire exercise that could reduce the value of the RR. A shakedown exercise could also lead to positive modifications of the protocol, training, and SSE. A nondisclosure agreement will maintain the confidentiality of the data from the mock-up.

3. Magnetite-filled epoxy markers will be placed at the end of each test section to provide a circumferential reference point for both rotating and array probes.

4. An "NDE Task Group" will be formed with members nominated by the participants of the Second USNRC International Steam Generator Tube Integrity Research Program (ISG-TIP-2). The purpose of the task group will be to follow the RR exercise and provide input on the NDE work. One of the first activities would be to provide input on the protocol and procedure for the RR. The protocol would be developed following EPRI guidelines for inspection using qualified techniques for the various flaws similar to that done for ISI of SG tubes in the field. Several procedures will be employed to allow development of POD for the various probes and techniques that could be used to inspect the same flaws and locations in different SGs.

5. After considering opinions from industry experts, a BC inspection will be carried out for 100% of the tubes in the mock-up. The results from the BC inspection might lead to further evaluation with MRPC, depending on the details of procedures developed for the mock-up. In addition, specific inspections will be conducted at the top of tube sheet (TTS) and TSP locations by using qualified techniques for these locations and corresponding flaw types. Reporting of data may be carried out using the standard three-letter code currently used for ISI (e.g., MAI for multiple axial indication). If more detail is wanted, it must be specified very clearly in the procedure. EC data will be used to develop POD and sizing-accuracy information for different procedures and flaw types.

Following these two meetings, an NDE Task Group was organized to provide input on the ANL steam generator mock-up NDE round-robin. This group met during the last week of September 1998 at ANL. The objective of this meeting was to gather the information needed to develop an inspection plan for RR testing of the mock-up. The mock-up is being treated as a real operating steam generator, and an inspection plan consistent with industry practices and guidelines is being developed. Representatives from EPRI, Framatome technologies, Inc., Westinghouse, ABB-CE, Northern States Power, Duke Power, and Commonwealth Edison participated in this meeting.

During the September meeting of the NDE Task Group, various aspects of the RR were addressed. Input from the NDE Task Group was provided on (a) data acquisition, including instructions for recording and reporting of data; (b) data analysis, including procedures for sizing and selection of standards; (c) training of teams; and (d) site-specific testing of personnel. The make-up of the mock-up and the degradations were discussed. Input on a qualified inspection procedure for each degradation was provided. Input was also provided for a plan ("Site Applicability") to establish that the various EC NDE techniques to be used during the round robin apply to the mock-up configuration and degradation. Documentation that will be required for destructive analysis of the mock-up test sections was also discussed, as was data-base management for handling the acquired data.

During the meeting, EPRI eddy current data from field flaws were downloaded to ANL computers to compare with signals from flaws to be included in the mock-up. Signals from the ANL flaws and the sludge pile simulation were judged to be representative of field data. Issues that still need to be resolved include compensating for changes in EC signals resulting from sensitization of tubes with cracks and determining the best method for simulating magnetite on the tubes.

2.2.2 Statistical Analysis

A meeting was held with PNNL on June 29-30, 1998, to discuss the statistical requirements and analysis of the RR data. The meeting began with a tutorial (with handout) by Pat Heasler on statistical analyses for RR data. The topics included evaluation of detection, evaluation of sizing, test design, receiver operating characteristic (ROC) analysis, errors in regression analysis, and specific problems related to SG RRs. A presentation was made on the simple linear and spline logistic regression models that would most likely be used for RR data analysis, particularly for analyzing POD. An initial grading unit was suggested for data analyses. The grading unit could then be reduced to see if the POD changes. For test sections with many cracks, the grading may have to be carried out by evaluating degraded area reported.

Technical discussions covered (a) objectives for POD confidence limits, (b) placing of artifacts on tubes, (c) number of flawed tubes that need to be destructively analyzed to have confidence in estimates of true state, and (d) the extent to which copper should be plated on test sections.

One possibility for evaluating the data would be to place results for each grading unit into one of four categories: (a) good test section called good (correct negative; C-), (b) good test section called flawed (false positive; F+), (c) flawed test section called good (false negative; F-) and (d) flawed test section call flawed (correct positive; C+)

A discussion was carried out on whether tubes from McGuire could be added to the mock-up if loose contamination can be eliminated. McGuire test sections would have to be confined to tubes dedicated to 19.1-mm (3/4-in.)-diameter test sections. Inserts could be put in the polypropylene spacers to accommodate the smaller-diameter test sections and still maintain a good mechanical fit. It was decided not to include the McGuire samples in the mockup, but input from these samples will be used to validate results from the laboratory specimens.

Pat Heasler of PNNL provided a preliminary analysis of the effect of sizing errors in true state on POD and sizing regression fits. Errors in true state sizing ranging from 2.5 to 15% TW were considered. The sample size considered was 100 flaws and 50 blanks. The POD analyses for "good" and "average" POD curves were calculated. The "good" curve will be more severely influenced by the error in true state. Curves, with confidence limits, of POD versus flaw size for a variety of sizing errors were provided. Errors in true state sizing exceeding 10% TW may result in unacceptably high uncertainties in the POD curve developed.

2.3 Eddy Current Profiles of SCC

A significant effort has been made to establish the accuracy of profiling deep cracks. Some of the axial OD profile data were used to predict the failure of tubes in ANL's Pressure and Leak-Rate Test Facility. For the initial effort, EC signals from two tubes that were subsequently tested were examined in order to obtain the crack profile before failure. The phase angle from the Lissajous pattern at various points along the crack, generated by a +Point coil, was compared to the phase angle from EDM notches of depths 40, 60, 80 and 100% TW using the same coil. The estimates of percent TW were made every millimeter as long as reasonable S/N ratios were evident. As a result, the entire profile of the crack could not be made, and only the deepest part of the crack has been profiled. Amplitudes for the EC

signal dropped off dramatically at points beyond those plotted. For SGL-195 (using a frequency of 300 kHz), two peaks in the profile are visible, with a maximum depth of about 90% TW and an average depth of approximately 85% TW over a span of 10 mm (Fig. 2.9). For the second test section, SGL-177, the deepest part of the crack is shorter than in SGL-195, although the maximum EC depth of 90% TW is about the same as for SGL-195 (Fig. 2.10). In the case of SGL-177, the profiles are plotted for both 200 and 300 kHz so one can see the effect of frequency on profiling. The average of the two curves is plotted as a continuous line. The results for SGL-195 and SGL-177 are consistent with the predicted depth based on the failure pressures and on dye penetrant examination before pressure testing. Note that small cracks deeper than indicated by the EC profile are expected. However, those small tight cracks will not be seen in the EC profile, and their presence will not significantly affect the failure pressure.

Additional profiling with EC data from cracked tubes that were failed in the Pressure and Leak-Rate Test Facility has been carried out. For smaller signals and where phase analysis is not effective (depth < 60-70% TW in these cases), a depth was established from the phase analysis at a relatively deep point, and depth was then correlated with signal amplitude using straight linear extrapolation to 0% TW. As a result, the entire EC profile of the crack could be made. However, one should again note that it is probable that very small cracks associated with the main crack will not be resolved, although they may affect BC voltages. For test section SGL-104 (using a frequency of 300 kHz), a peak in the profile is evident at a maximum depth of ≈93% TW (Fig. 2.11). The magnetically biased BC phase of 77° suggests a maximum depth of ≈80% TW, less than the +Point maximum. Based on the crack profile, the estimated failure pressure (initiation of leakage) is in agreement with the actual failure pressure of 16.2 MPa (2350 psi).

Eddy current crack depth as a function of position was also determined for test section SGL-219 using phase and amplitude analysis at 300 kHz with a +Point coil and EDM notches for calibration. The profile shows a maximum depth of ≈90% TW, with a dip in the profile to ≈70% TW. The magnetically-biased BC phase of 85° suggests a maximum depth of ≈75% TW, less than the +Point maximum depth (Fig. 2.12). The BC voltage (using a 100/400 kHz mix with the voltage for the four ASME 20% TW holes set to 2.75 V) was significantly lower than for test section SGL-104 (6.3 vs. 9.2 V) even though the maximum depths and lengths are approximately the same. The lower voltage may be the result of greater contact between the crack faces.

A fifth test section, SGL-225, was also analyzed; it had two axial ODSCC cracks separated by ≈5 mm. This separation was sufficient to allow each crack to be analyzed separately. Figure 2.13 shows the profiles of both cracks. The maximum depths are 80 and 90% TW, with both showing a dip in the profile at about the same axial position.

The predictions of failure pressure based on the crack profiles have been consistent with actual failure pressure for tubes SGL-195, SGL-177 and SGL-104 (see Section 4.8.2).

2.4 NDE of McGuire Tubes

Eddy current signals from deplugged tubes of retired steam generator D at the Duke Power McGuire nuclear station were compared with EC signals of previous inspections (December
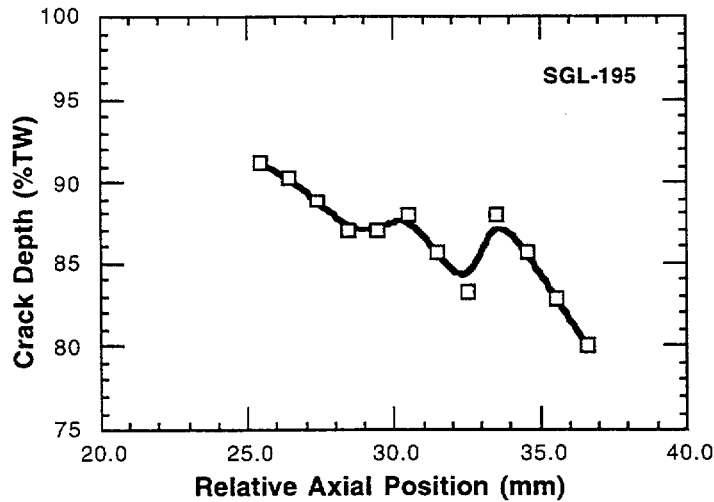
Fig. 2.9.   Axial OD crack depth as a function of position for test section SGL-195 using phase
analysis at 300 kHz with a +Point coil and EDM notches for calibration. Only eddy
current signals with good S/N ratios were analyzed. Signals from ends of crack had
much lower amplitude than signals near the middle. Solid line represents smooth
curve fit to measurements.
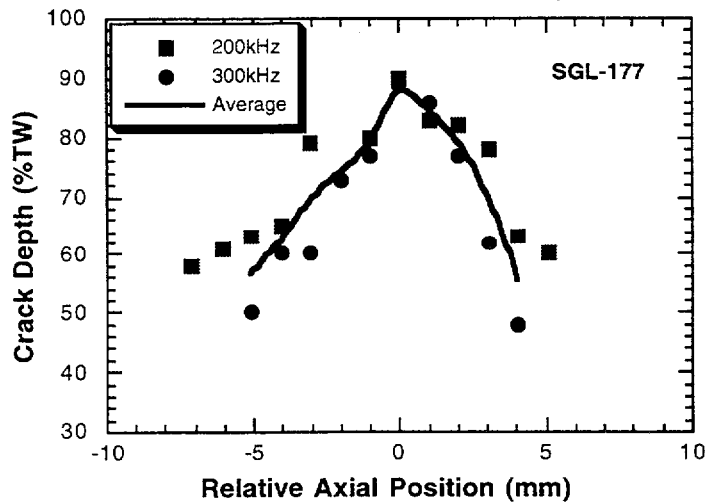
Fig. 2.10.   Axial OD crack depth as a function of position for test section SGL-177 using phase
analysis at 200 and 300 kHz with a +Point coil and EDM notches for calibration.
Only eddy current signals with good S/N ratios were analyzed. Signals from ends
of crack had much lower amplitude than signals near the middle, and thus depth
estimates were not made beyond the region shown in figure.
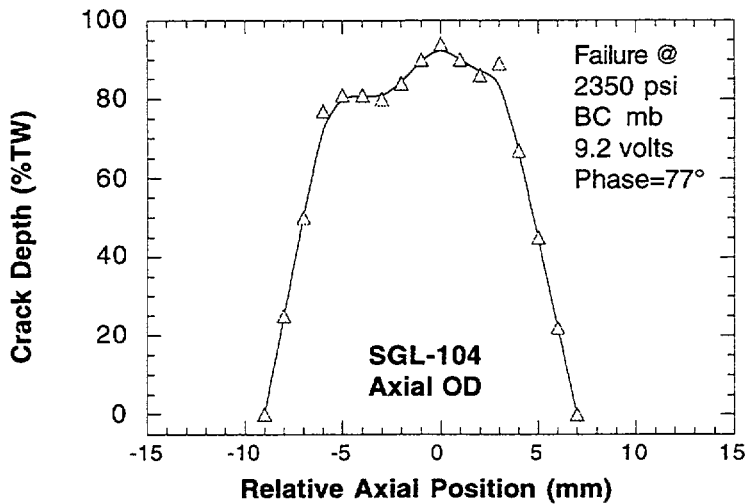
Fig. 2.11. *Eddy current crack depth as a function of position for test section SGL-104 using phase and amplitude analysis at 300 kHz with a +Point coil and EDM notches for calibration. Only eddy current signals with good S/N ratios were used for depths over 70% TW. Signal amplitude was used for shallower parts of crack. Small cracks deeper than indicated by the eddy current profile are expected. However, those small tight cracks will not be resolved in the EC profile, and their presence will not significantly affect failure pressure. Solid line represents smooth curve fit to measurements.*
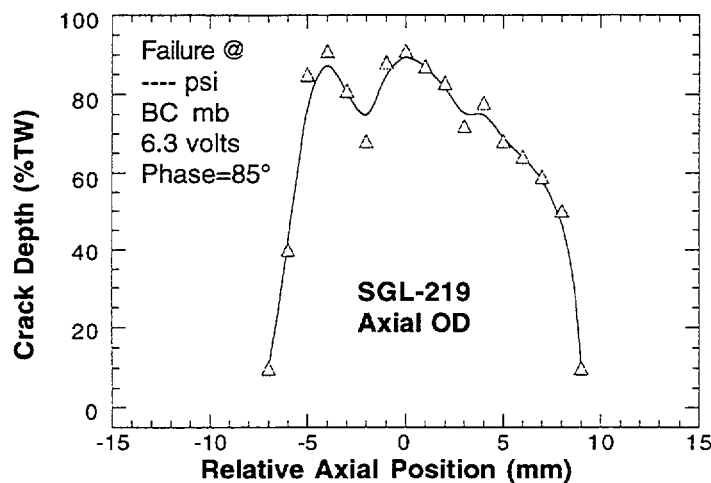
Fig. 2.12. *Eddy current crack depth as a function of position for test section SGL-219 using phase and amplitude analysis at 300 kHz with a +Point coil and EDM notches for calibration. Only eddy current signals with good S/N ratios were used for depths over 70% TW. Signal amplitude was used for shallower parts of crack. Small cracks deeper than indicated by eddy current profile are expected. However, those small tight cracks will not be resolved in the EC profile, and their presence will not significantly affect failure pressure.*
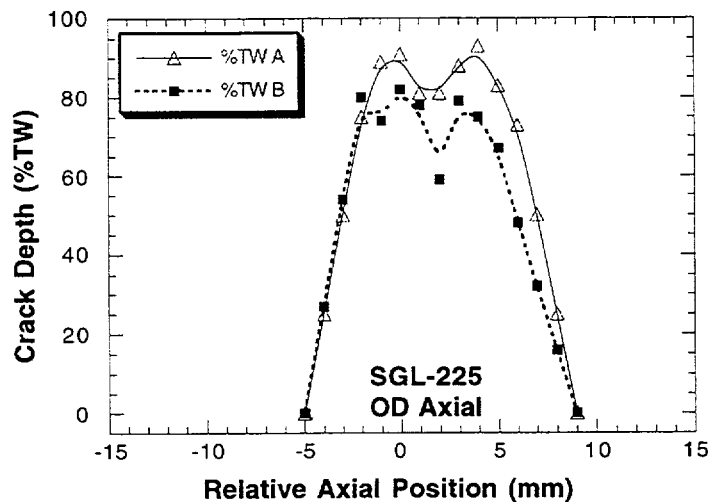
Fig. 2.13. *Eddy current crack depth as a function of position for test section SGL-225 using phase and amplitude analysis at 300 kHz with a +Point coil and EDM notches for calibration. Only eddy current signals with good S/N were used for depths over 60% TW. Signal amplitude was used for shallower parts of crack. Two axial OD cracks, separated by 5 mm, were analyzed at the same time. Small cracks deeper than indicated by eddy current profile are expected. However, those small tight cracks will not be resolved in the EC profile, and their presence will not significantly affect failure pressure*

1995 and August 1994). The present data were acquired using the same types of probes, standards, and procedures that were used during earlier outages. In all cases, the BC voltages for flaw indications increased during the time the tubes were plugged.[1] Possible causes include crack initiation, crack growth, wider crack opening, or a change in deposits. In addition, as a result of the availability of new +Point™ data (not taken during previous ISI), new crack calls from relatively small EC signals were made. A review of some earlier EC data indicated that these new calls would not have been made with the data available during previous inspections. The preliminary conclusion is that new calls made on the deplugged tubes would not have been made previously because (a) the EC signals initiated after the December 1995 ISI or (b) the EC signals were too small to be called flaw indications with probes used at that time but have grown enough to be detectable now.

The growth of an EC signal attributed to an SCC can be seen in Figs. 2.14 and 2.15. In Fig. 2.14, the arrow on the c-scan plot points to an EC signal at the top of the tube sheet (TTS) in tube R39 C46 generated by a 2.92-mm (0.115-in.)-diameter motorized rotating pancake coil (MRPC). This indication was called an SCC in August 1994. Figure 2.15 shows the TTS in July 1997 after the tube was deplugged. These data were also taken with a 2.92-mm (0.115-in.)-diameter MRPC. The signal has grown considerably relative to the roll transition for one or more of the reasons suggested above.

A multiple axial indication was also called by ANL in July 1997 in a tube that was not previously plugged. The 2.92-mm (0.115-in.)-diameter MRPC isometric plot from 1995 is
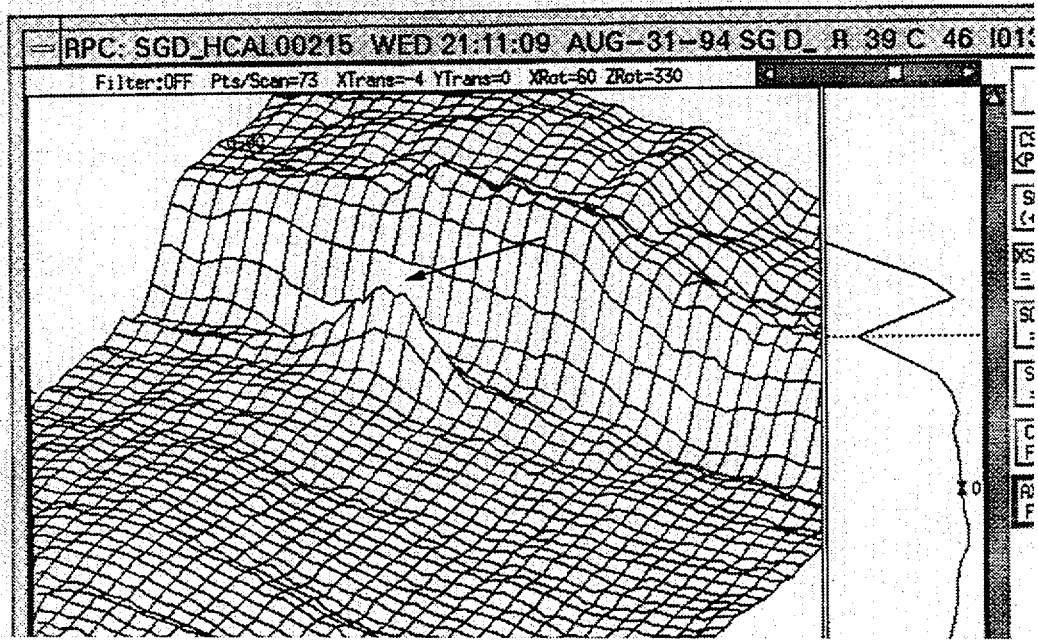
Fig. 2.14.   C-scan plot from 0.115 MRPC; arrow points to indication at top of tube sheet (TTS) in tube R39 C46. This indication was called an SCC in August 1994. Tube axis is from lower left to upper right, with 360° of tube shown.
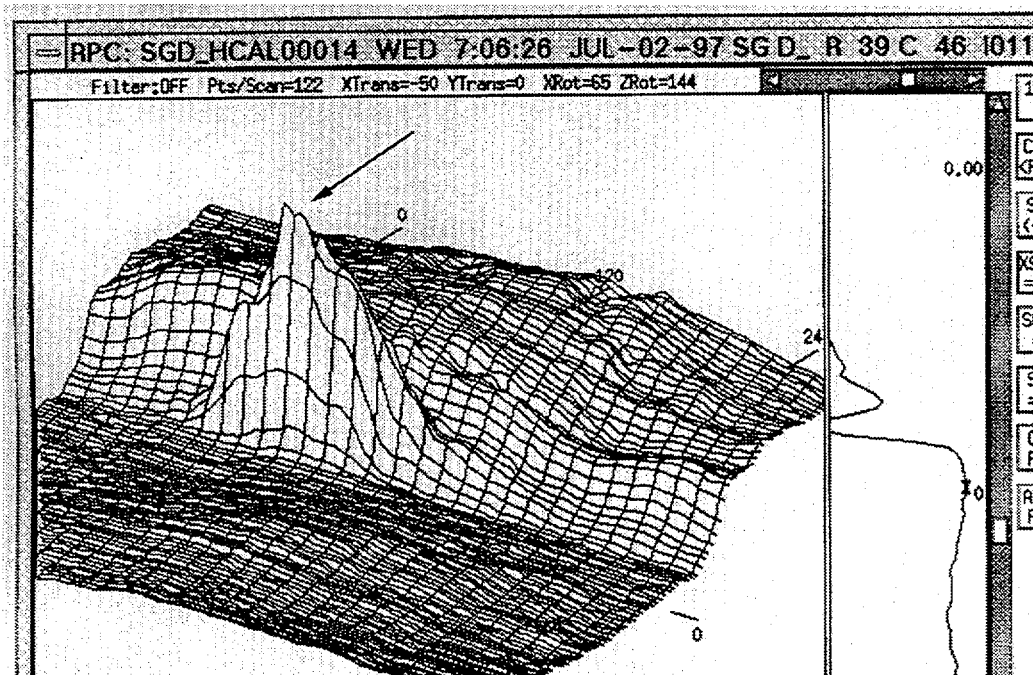
Fig. 2.15.   C-scan plot of same region shown in Fig. 2.14 taken with a 2.92-mm (0.115-in.)-diameter MRPC in July 1997 after tube was deplugged. Signal (arrow) has grown considerably relative to roll transition. Tube axis is from lower left to upper right, with 360° of tube shown.
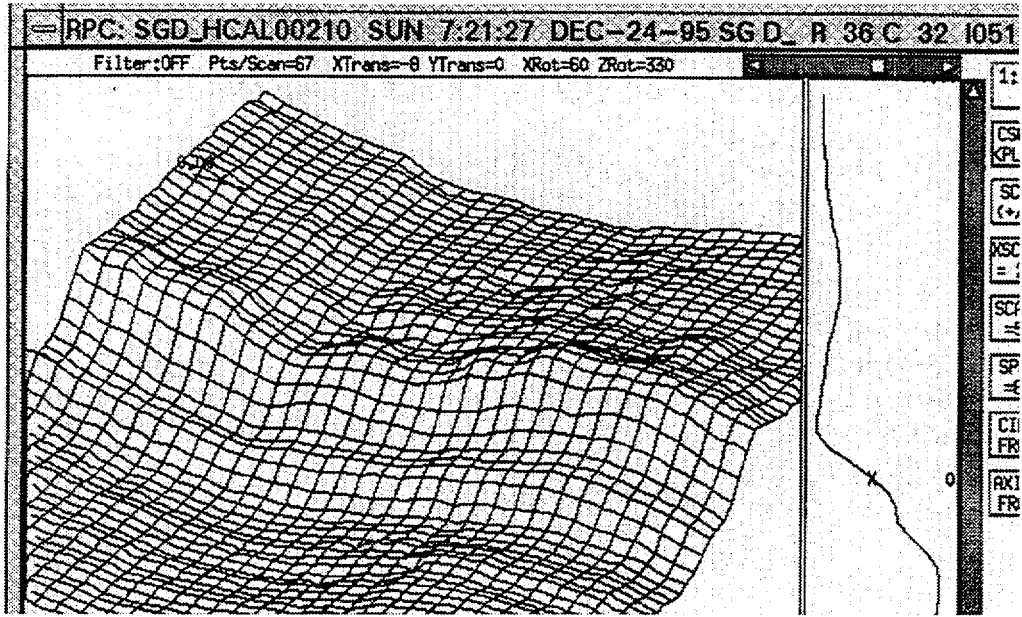
Fig. 2.16. *1995 c-scan plot of TTS of tube R36 C32 made with a 2.92-mm (0.115-in.)-diameter MRPC. No indication around roll transition was called at that time, and tube was not plugged. Tube axis is from lower left to upper right, with 360° of tube shown.*

presented in Fig. 2.16. No indication around the roll transition was called at that time. The MRPC result from 1997 is presented in Fig. 2.17. With the help of the +Point™ data, the call this time is MAI (multiple axial indication). The value of additional data from a +Point™ coil can be seen in Fig. 2.18, where multiple axial indications in and around the roll transition can be seen more clearly. While these indications are relatively small, they are another example of observable EC signal growth between inspections.

While the amplitude of the EC signal may change for reasons other than crack growth, the change in length of the EC indication is more likely to be related to actual change in crack length. The length change of the crack in R39 C46 seen in Fig. 2.14 has been estimated. The beginning and ends of the EC signal that can be attributed to the crack are, in this case, subject to some interpretation. Figure 2.19 shows the range of uncertainty and best guess for the crack lengths in 1994 before plugging and in 1997 after unplugging. Analysis of the data suggests the crack grew somewhat in length during the time the tube was plugged. The best estimate is that crack extended in length from 15 to 23 mm (0.6 to 0.9 in.). The estimated lengths with uncertainty are 15 ± 2.5 mm (0.6 ± 0.1 in.) and 23 ± 5 mm (0.9 ± 0.2 in.).
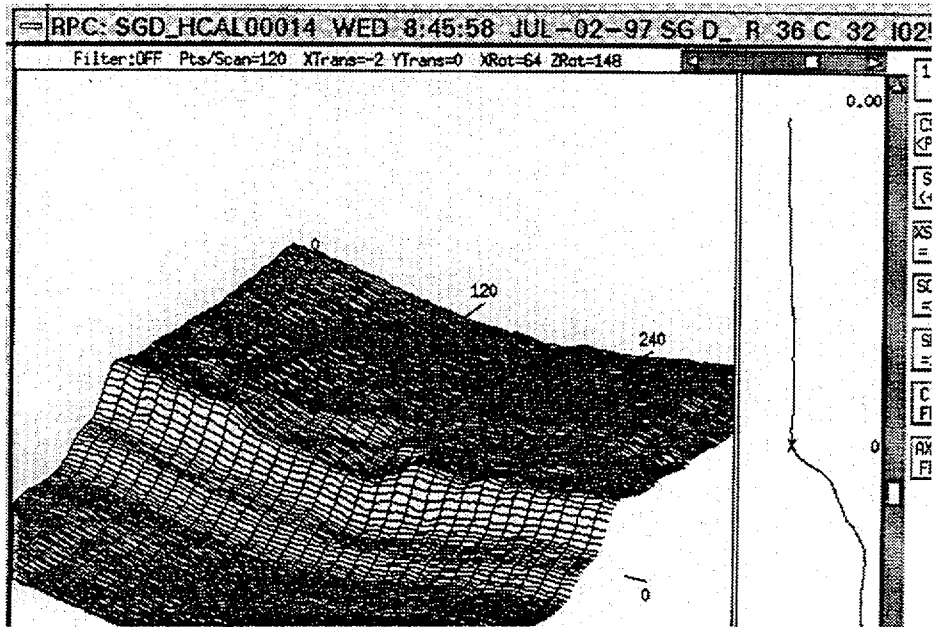
Fig. 2.17. *C-scan plot of same region shown in Fig. 2.16, made in 1997 with 2.92-mm (0.115-in.)-diameter MRPC. Multiple axial indication (MAI) was called.*
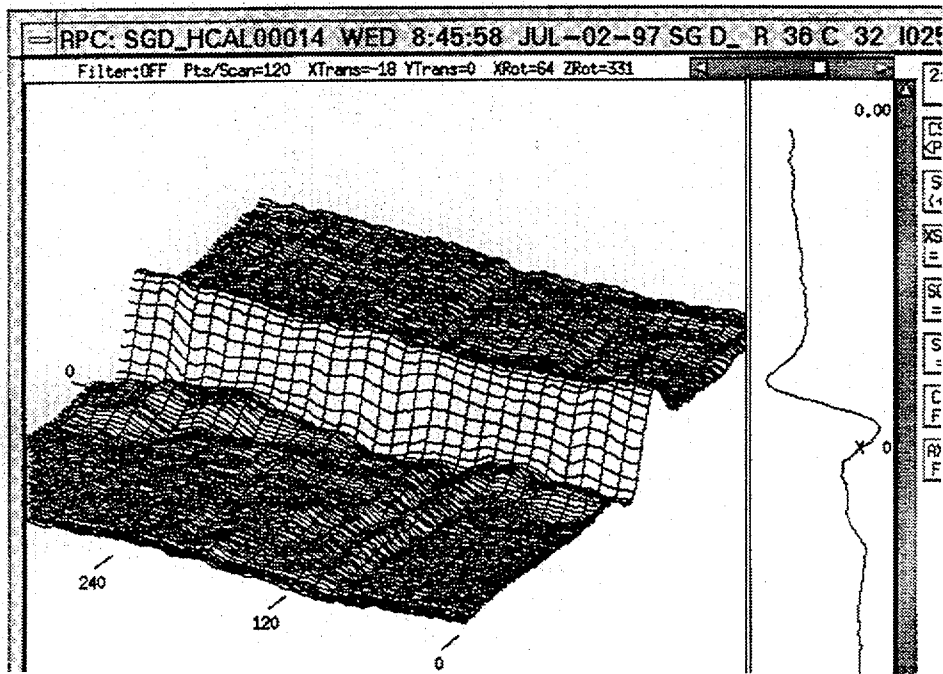
Fig. 2.18. *1997 c-scan image of same region shown in Figs. 2.16 and 2.17 made with +Point™ coil; call again is MAI. Value of additional data from +Point™ coil can be seen here, where multiple axial indications in and around roll transition can be seen more clearly than in Fig. 2.17.*
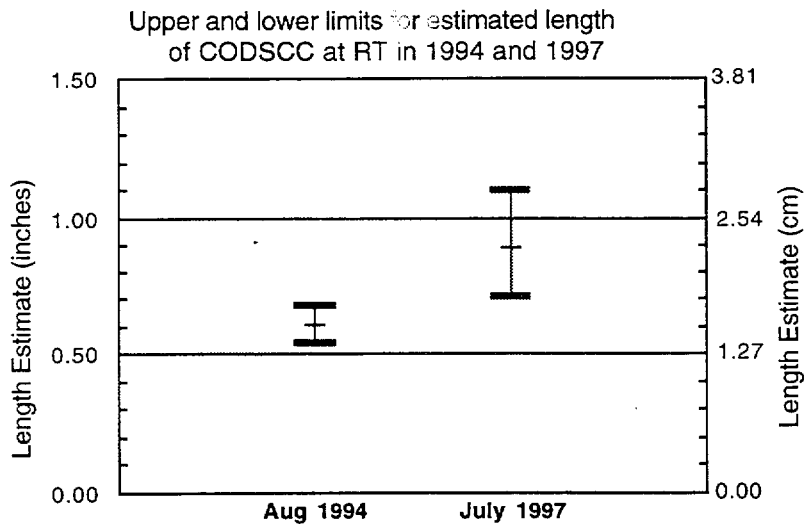
Fig. 2.19.   Estimated length with range of uncertainty for circumferential outer diameter stress corrosion crack (CODSCC) at top of tube sheet in tube 39-46 of McGuire retired steam generator before (August 1994) and after (July 1997) plugging.

3 Research on ISI Technology (S. Bakhtiari and D. S. Kupperman)

The objective of this task is to evaluate advanced NDE and signal analysis techniques for the reliable ISI of original and repaired SG tubes. Improved correlations between EC probe response and flaw morphology, leak rate, and failure pressure will be developed and validated. In addition, the reliability of the voltage parameter and other EC parameters and techniques will be evaluated with respect to their range of applicability.

The present research studies on improved ISI of SG tubes focus on four primary areas: (a) implementation of analytical methods for prediction of EC response as a function of probe design, flaw characteristics, and material properties; (b) development of effective signal analysis procedures; (c) development of flaw imaging and display methods for simple and accurate flaw characterization; and (d) evaluation of improved probe designs that use directional arrays so that defects of arbitrary orientation can be examined simultaneously. The reliability and effectiveness of improved inspection techniques and the robustness of potential correlations will ultimately be substantiated through laboratory testing of the SG tube bundle mock-up and of SG tubes that contain various flaw morphologies. Final validation will also utilize in–service-degraded SG tubes.

A description of Task 2 activities carried out during the present reporting period is presented here. In continuation of earlier electromagnetic (EM) simulation studies on the determination of bobbin coil (BC) probe response to axial notch size, numerical and experimental results are presented in Section 3.1. This work was carried out to help quantify the expected probe output voltage and sensitivity to typical machined flaws in calibration-standard tubes. Numerical results have been normalized to allow direct comparison with calibrated experimental data. As a follow-up to earlier investigations to study potential correlations between BC probe readings and tube structural integrity, analysis results are presented in Section 3.2 on two separate multivariate modeling approaches, namely a standard multiple linear regression and a neural network structure. Representative results are shown for different training set configurations that were used to assess the prediction capability of each modeling approach. Observations regarding the applicability of each technique are also discussed in this section.

3.1 Bobbin Coil Response to Axial Notches

In continuation of earlier theoretical modeling studies, numerical and experimental results are presented next on the effect of axial notch size on BC response. All data pertain to the conventional 18.3-mm (0.72-in.)-diameter coil used for ISI of 22.2-mm (0.875-in.)-diameter Alloy 600 SG tubes. This work was carried out to quantify the expected probe sensitivity to crack size and to further help in related studies on the determination of potential correlations between BC signal amplitude and tube integrity (i.e., mechanical properties).

3.1.1 EM Modeling

Preliminary results of finite-element calculations on the effect of ideal crack depth and length on absolute BC signal amplitude were presented in a previous report.[1] Results of this study have been updated to include the differential coil configuration and to compare with

experimental results on EDM notch standards. The simulated flaw geometries consisted of drilled hole and axial notches. These defects are present in ASME and other calibration standard tubes and routinely serve as reference indications for the calibration of BC signal. The four 20% OD flat-bottom holes (FBHs) placed at 90° intervals around the tube circumference in an ASME standard are conventionally used to normalize BC signal amplitude. Machined notches, on the other hand, are utilized when more accurate characterization of SG tube cracking is of primary interest. All simulated test cases in this study pertain to manufactured defects on 22.2-mm (0.875 in.)-diameter Alloy 600 tubing with a nominal wall thickness of 1.27 mm (0.05 in.) and estimated conductivity ρ of 100.0 $\mu\Omega$-cm. Simulated OD axial EDM notches varied in depth from 20 to100% TW. The probe modeled is a conventional 18.3-mm (0.72-in.)-diameter BC. Simulations were carried out at frequencies f = 100 and 400 kHz, which represent typical usable limits for the detection of small degradations in thin-wall tubing.

Figure 3.1 depicts longitudinal and transverse cross sections of a BC located symmetrically under an OD-initiated discontinuity. For the initial test-case results presented here, the 20% TW OD holes have a diameter of 4.76 mm (≈0.187 in.). Simulated axial notches varied in depth between 20% and 100% TW, with lengths ranging from 6.35 mm (0.25 in.) to 50.8 mm (2.0 in.). For all test cases, the axial flaw width W was taken to be 0.125 mm (0.005 in.). The BC's length and height were taken to be 1.27 mm and 1.53 mm, respectively. With reference to Fig. 3.1, the coil's initial axial position z = 0 was designated to be the middle of the defect. Due to the symmetry of the problem, only 1/8 of the problem space was modeled.

Figures 3.2(a) and (b) depict the distribution of current density at f = 100 kHz for a single 20% TW OD hole and a 6.35-mm (0.25-in.)-long axial notch with the coil positioned in the middle of the discontinuity at z = 0. In both cases, the redistribution of circumferentially induced current flow around the defect indicates good depth of penetration at this frequency for the detection of OD tubing discontinuities. In this case, with the axial extent of the two defect geometries being comparable, it is expected that the much larger volume of the FBH would result in a substantially stronger perturbation of induced currents, thus giving rise to a much larger change of probe impedance. With skin depth attenuation being a function of frequency and distance from the ID surface, the sensitivity and consequently the variation of coil input impedance drops rapidly with increases in these parameters. Consequently, it is expected that the accuracy in calculation of the numerical results would be affected in a similar manner.

To compare voltage responses from different flaw geometries, a series of simulations was carried out to determine variations of impedance components as a function of probe position. The results were then normalized to have a 4 V peak-to-peak differential and 2 V absolute peak amplitude for the 20% TW OD FBHs at f = 400 kHz. Figure 3.3 shows sample calculations for the normalized BC differential and absolute signals at f = 100 and 400 kHz for the ASME holes. The responses are shown in terms of both the impedance trajectory and variation of signal magnitude as a function of position, with the center of the OD discontinuity located at z = 0. A more complete selection of predicted impedance plane trajectories is provided in Ref. 1.
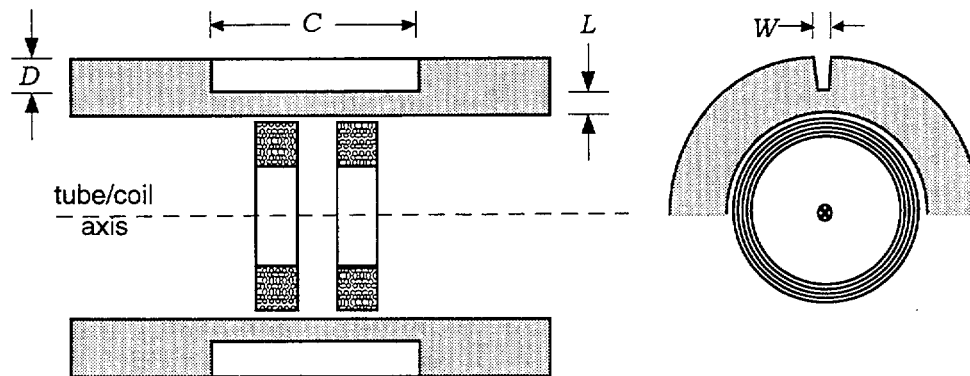
Fig. 3.1. Cross-sectional geometry of differential bobbin coil inside a tube with four symmetric OD discontinuities of length C and width W.

3.1.2 Effect of Axial Notch Size on Bobbin Probe Signal Amplitude

As described previously,[1] a series of single-point calculations was made to determine the maximum signal amplitude of an absolute coil for various notch depths and lengths. The notch lengths considered were C = 6.35 mm (0.25 in.), 12.7 mm (0.5 in.), 19.05 mm (0.75 in.), 25.4 mm (1.0 in.), 38.1 mm (1.5 in.), and 50.8 mm (2.0 in.). The flaw depths from the OD were taken to be 20-100% TW. Figure 3.4(a) and (b) display the result of the analyses at f = 100 and 400 kHz, respectively. In these figures, the signal amplitudes were normalized with respect to that obtained for the 50.8-mm (2.0 in.), 100% TW notch at each frequency. The voltage amplitude $V^{(C,D)}$ for a notch of length C and OD depth D (in % TW) can be expressed in terms of its normalized voltage $\hat{V}^{(C,D)}$ and that of a reference notch $\hat{V}_0$ of length C_0 and depth D_0 with an arbitrary calibrated voltage V_0 as:

$$V^{(C,D)} = \frac{\hat{V}^{(C,D)}}{\hat{V}_0} V_0. \tag{3.1}$$

Full-length differential coil simulations were done for three different notch lengths and at discrete axial positions. The notch lengths analyzed were C = 6.35 mm (0.25 in.), 12.7 mm (0.5 in.), and 25.4 mm (1.0 in.). All other parameters were kept the same as the absolute coil case. Figure 3.5 shows the numerical results for the differential BC amplitude response as a function of depth for the simulated notches for C = 25.4 mm (1 in.).

As expected, the signal amplitude drops exponentially as a function of defect depth for both coil configurations. Also, the response to OD flaws is smaller at the higher frequency in all cases, and this difference becomes significantly larger for shallower flaws. Although the resistive and reactive signal components display different responses as a function of position, the maximum signal magnitude for all test cases occurs in the center of the defect. Due to higher conduction loss at higher frequencies, the drop in the signal amplitude is much faster at the higher frequency as the OD notch depth is reduced.
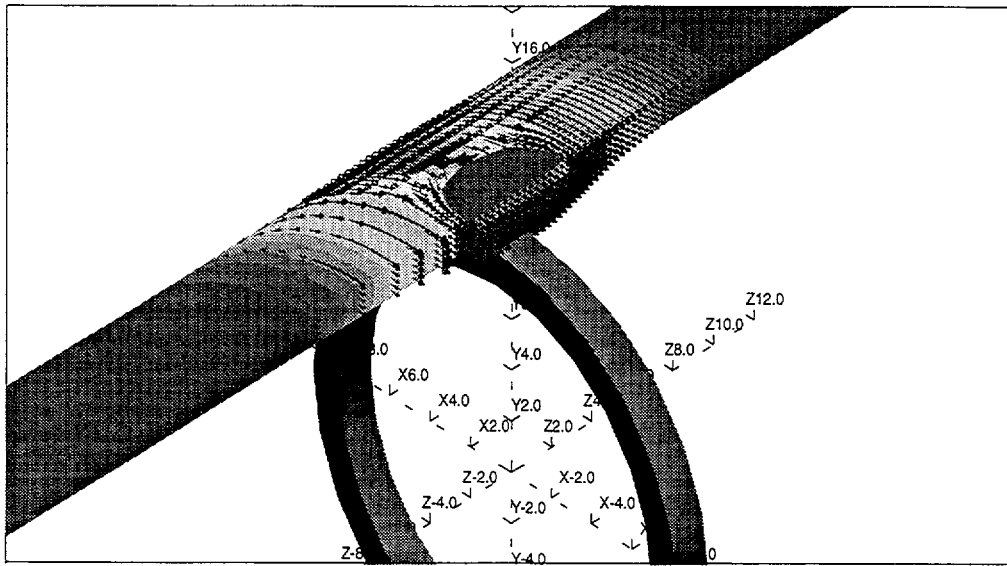
(a)
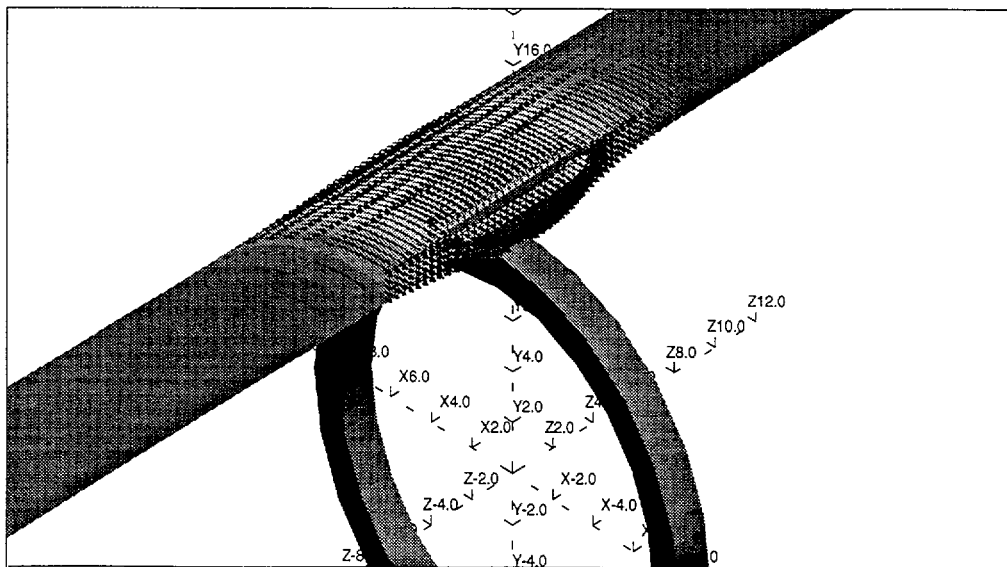
(b)

Fig. 3.2.   Distribution of current density at f = 100 kHz induced by absolute bobbin coil on 22.2-mm (0.875-in.)-diameter Alloy 600 tube with 20% TW OD (a) FBH with diameter of 4.76 mm (0.187 in.), and (b) axial notch of length C = 6.35 mm (0.25 in.) and width of W = 0.125 mm (0.005 in.). Arrow size and orientation show intensity and direction of induced current at each location, respectively.
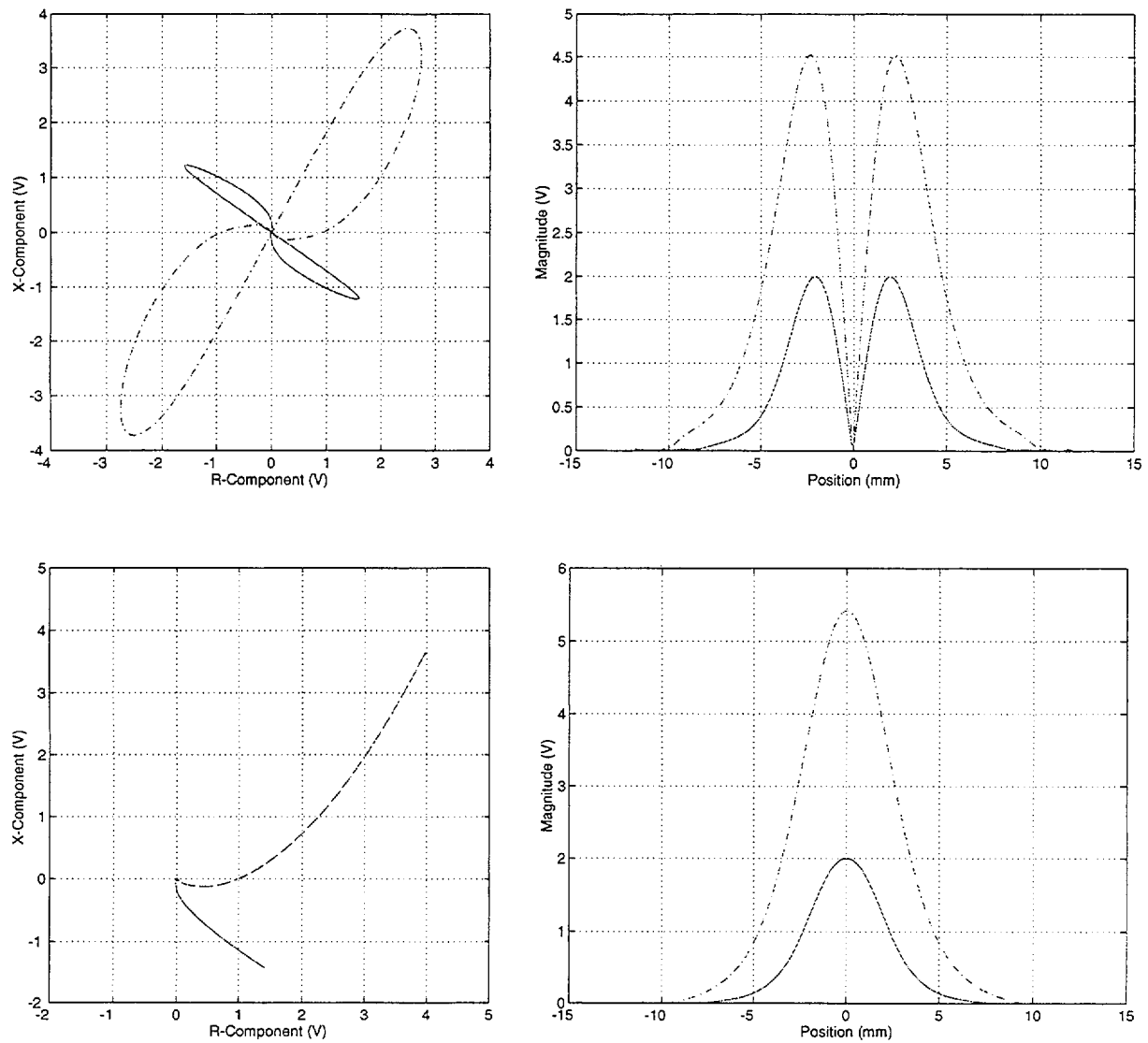
Fig. 3.3.   *Differential (top) and absolute (bottom) bobbin probe impedance trajectory (left) and signal amplitude (right), in volts, at f = 400 kHz (solid line), and f = 100 kHz (dashed line) for four 20% ASME standard OD FBHs placed 90° apart around tube circumference.*
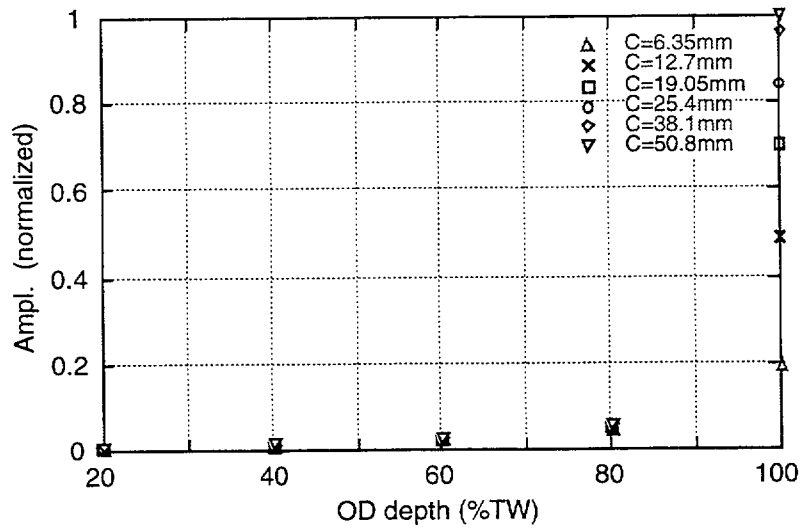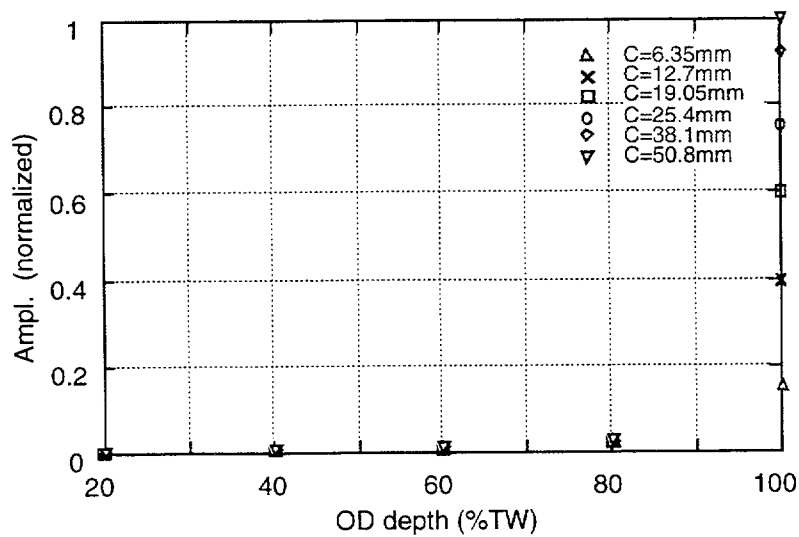
Fig. 3.4.   Predicted normalized (with respect to 50.8-mm [2.0-in.]–long notch) peak amplitude variation of 18.3-mm (0.72-in.)-diameter absolute bobbin coil as a function of depth and length for 0.127-mm (0.005-in.)-wide axial notch at (a) f = 100 kHz, and (b) f = 400 kHz.
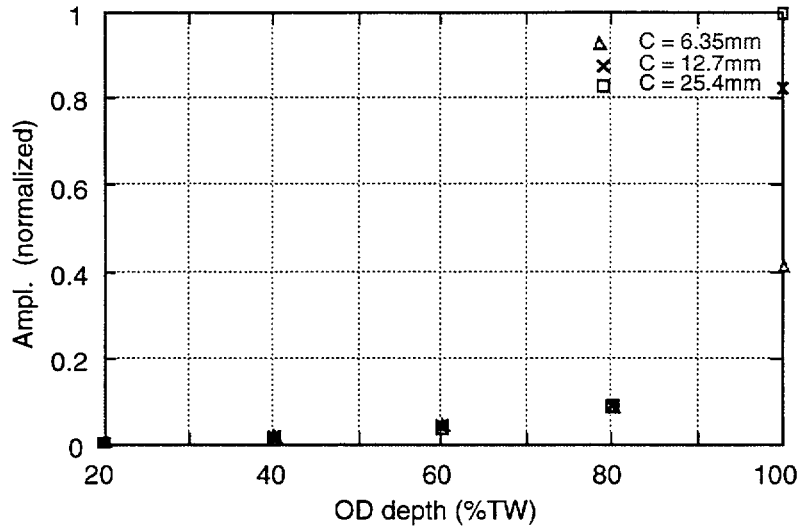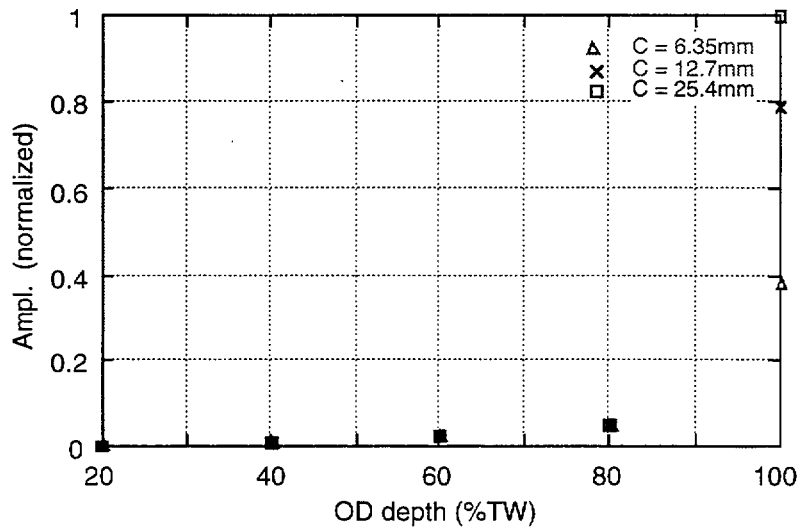
Fig. 3.5. *Predicted normalized (with respect to 25.4-mm [1.0-in.]–long notch) peak-to-peak amplitude variation for 18.3-mm (0.72-in.)-diameter differential bobbin coil as a function of depth and length for 0.127-mm (0.005-in.)-wide axial notch at (a) f = 100 kHz, and (b) f = 400 kHz.*

Although the reference voltage V_0 could be calculated by FEM, to minimize the differences between simulated and actual coil geometries, tube, and flaw dimensions, the predicted voltages were scaled using the measured values for a 6.35-mm (0.25-in.)-long axial EDM notch from an available tube standard. According to the specification sheet for the standard, the notch width was estimated to be ≈0.152-0.203-mm (0.006-0.008 in.) wide. Multiple frequency EC readings were made with a 18.3-mm (0.72-in.)-diameter magnetically biased BC using a MIZ-30 acquisition instrument. The calibration for the measurements was done by setting the 400 kHz differential signal amplitude for four 20% TW OD FBHs from an ASME standard to 4 V (peak-to-peak). Figures 3.6 and 3.7 show the predicted variation of the amplitude as a function of notch length for absolute and differential coils after scaling the normalized values in Fig. 3.4 and 3.5 by the measured voltage from the 6.35-mm (0.25-in.)-long axial EDM notch.

3.1.3 Comparative Studies: Theory and Experiment

To check the validity of the predicted trends for the absolute and differential BC responses as a function of axial crack depth and length, measurements were made on an EDM notch standard. The 22.22-mm (0.875-in.)-diameter Alloy 600 tube contained five sets of axial flaws with lengths between ≈5.08 and 25.4 mm (0.2 and 1 in.). For each flaw length, there are five OD notches with nominal depths of ≈20 to 100% TW. Average measured depths according to the specification sheet are recorded as ≈19.6, 38.2, 57.8, 76.6, and 100% TW, with up to 2% variation for a given flaw length. The average wall thickness is 1.33 mm (0.0525 in.). Calibration for the measurements was again done by setting the 400 kHz differential signal amplitude for four 20% TW OD drilled holes from an ASME standard to 4 V (peak-to-peak). Amplitude for all other channels were then referenced with respect to the 400 kHz channel. To reduce measurement errors, EC readings on the same tube were made four times, each time rotating the tube 90° about its axis and averaging out the recordings. Figures 3.8(a) and (b) show a single recording of the absolute and differential channel traces at $f = 100$ and 400 kHz. EC results were calibrated off-line by using an automated data manipulation algorithm.

Figure 3.9 and 3.10 show the variation of the measured signal amplitudes as a function of notch depth for the absolute and differential coils, respectively. The measurement results are generally in good agreement with the numerical results of Figs. 3.4 and 3.5, considering the differences between simulated and machined flaw geometries, tube, and coil dimensions. Figures 3.11 and 3.12 are plots of the measured amplitude as a function of notch length. Predicted results for these cases were shown in Figs. 3.6 and 3.7, respectively.

Analyses of the results indicate that the effect of simulated crack length on BC probe amplitude is much more significant for deep OD flaws approaching 100% TW. The signal amplitude saturates as the crack length increases. This saturation occurs much faster for the differential than the absolute coil configuration. For a given depth, the effect of length plays a more important role for deeper OD flaws and levels off toward a constant value as the length is increased. Consequently, the effect of length on BC signal amplitude for shallow OD flaws becomes more difficult to resolve, especially at higher frequencies. This suggests that a single-point voltage-based criterion for the determination of OD degradation extent could result in unreliable estimates for nonvolumetric flaws.
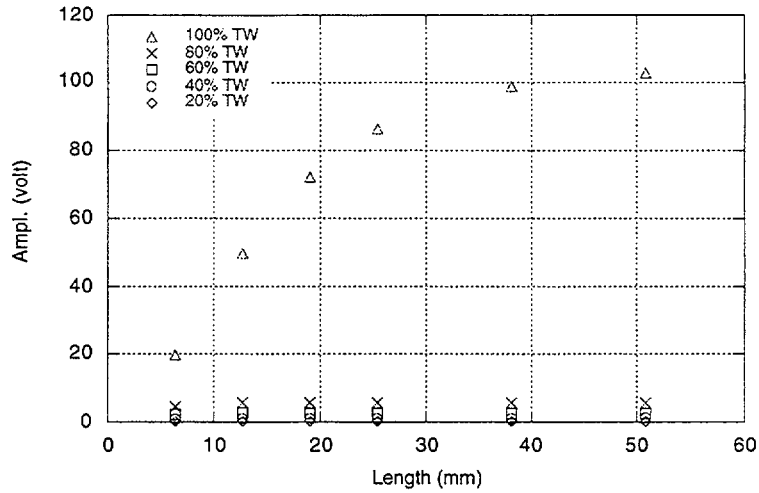
(a)
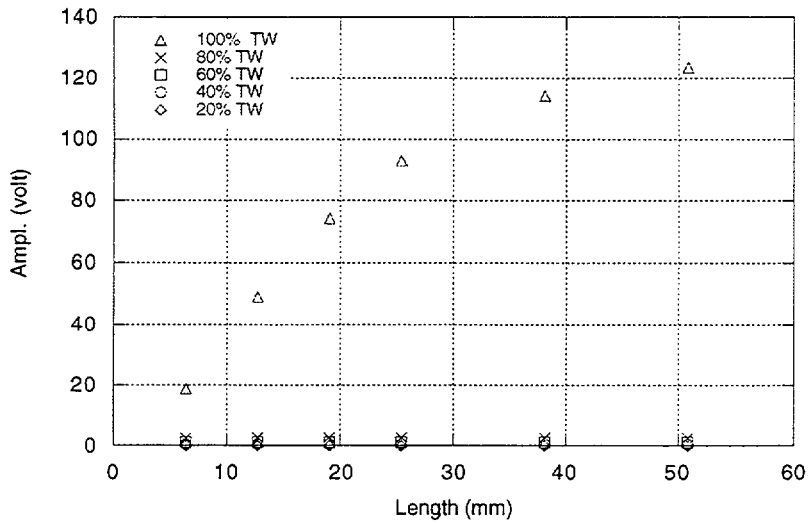
(b)

Fig. 3.6.   *Predicted peak signal amplitude variation (in volts) of 18.3-mm (0.72-in.)-diameter absolute BC as a function of length and depth for 0.127-mm (0.005-in.)-wide axial notch at (a) f = 100 kHz and (b) f = 400 kHz. Simulated data from Fig. 3.4 were scaled in reference to measured amplitude from 6.35-mm (0.25-in.)-long axial EDM notch in calibration-standard tube.*
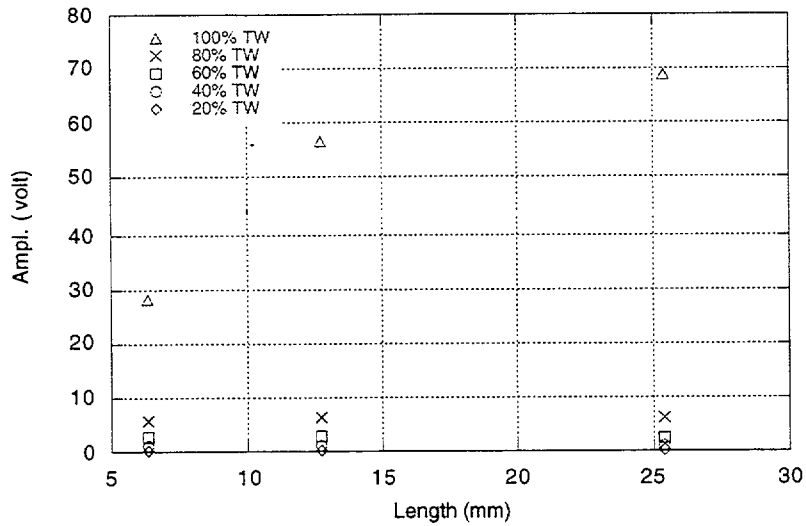
(a)
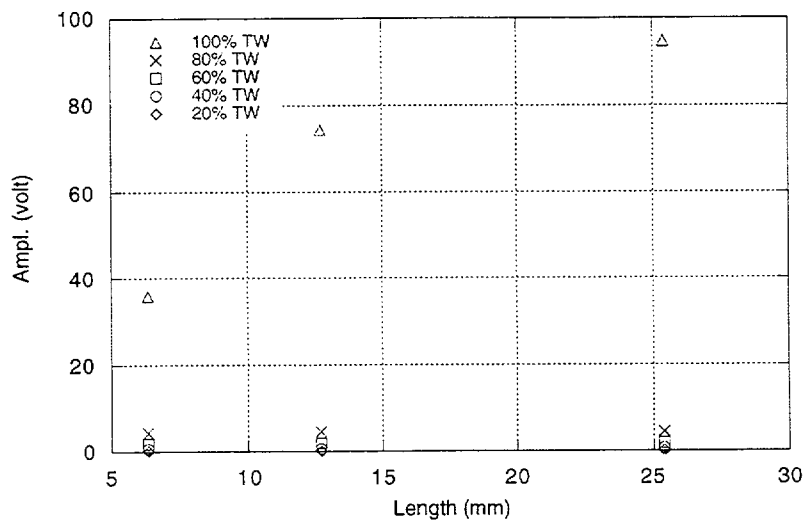
(b)

Fig. 3.7.   *Predicted peak-to-peak signal amplitude variation (in volts) of 18.3-mm (0.72-in.)-diameter differential BC as a function of length and depth for 0.127-mm (0.005-in.)-wide axial notch at (a) f = 100 kHz and (b) f = 400 kHz. Simulated data from Fig. 3.5 were scaled in reference to measured amplitude from 6.35-mm (0.25-in.)-long axial EDM notch in calibration-standard tube.*
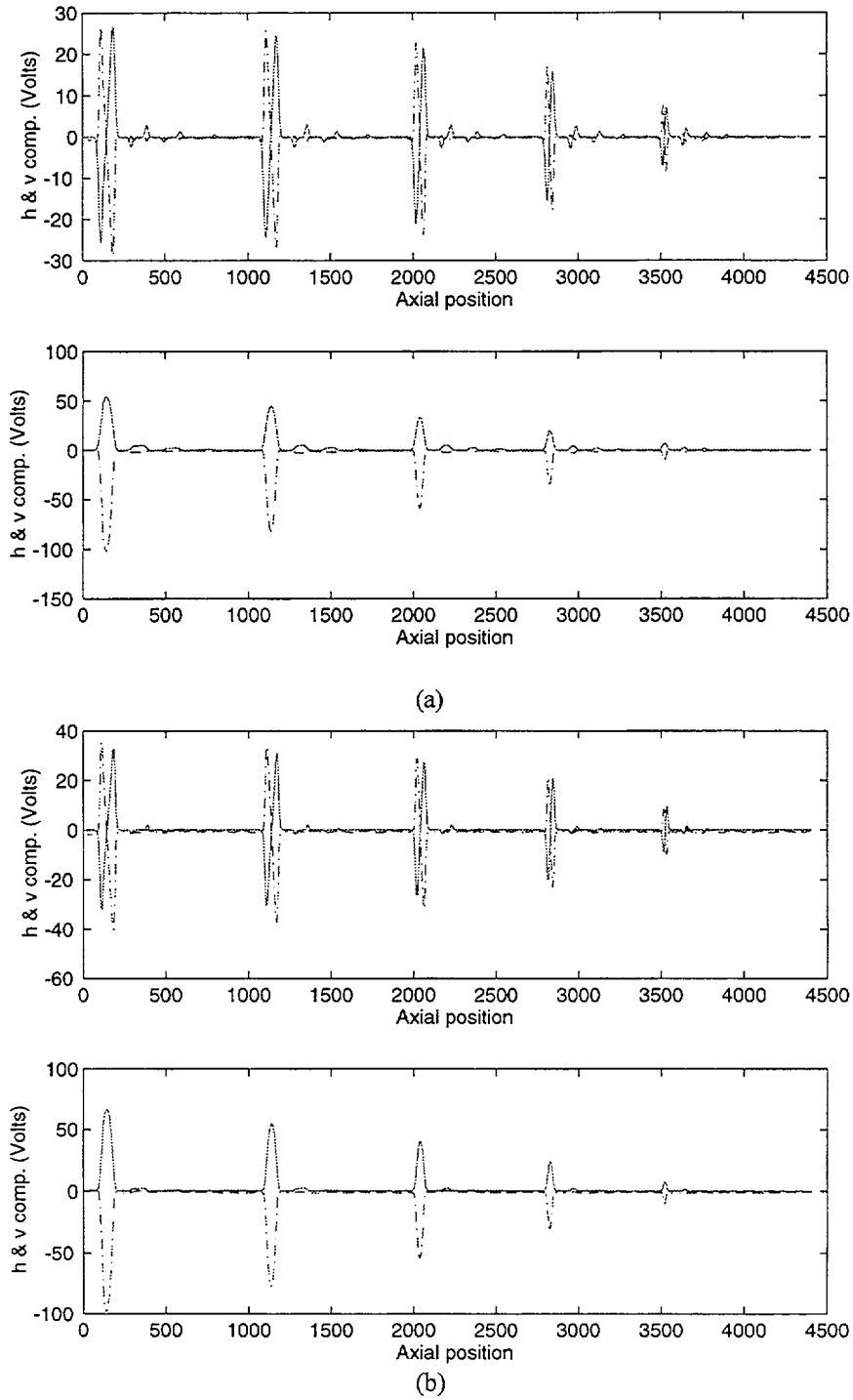
Fig. 3.8.   Differential (top) and absolute channel (bottom) readings at (a) f = 100 kHz, and
(b) f = 400 kHz with 18.3-mm (0.72-in.)-diameter magnetically biased bobbin coil
on EDM standard with five sets of axial EDM notches ranging in depth from
≈20% to 100% TW.   Nominal notch lengths in each set were 5.08 mm (0.2 in.),
10.16 mm (0.4 in.), 15.24 mm (0.6 in.), 20.32 mm (0.8 in.), and 25.4 mm (1.0
in.).
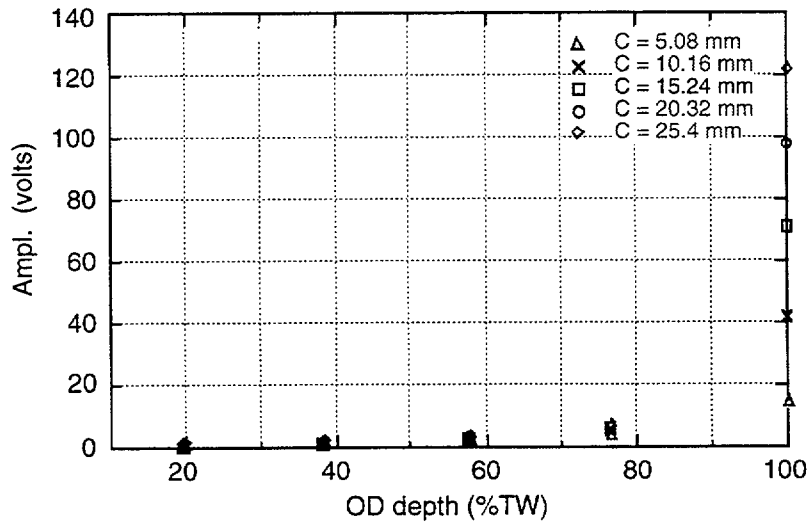
(a)
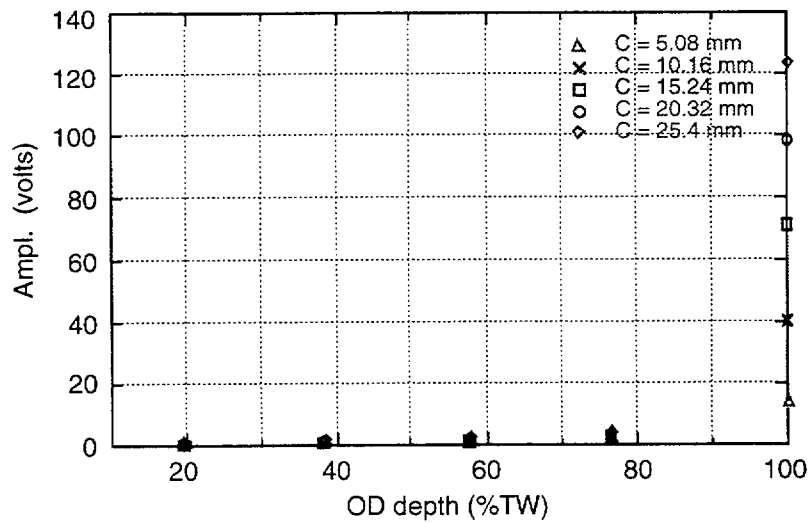
(b)

Fig. 3.9.   *Measured absolute peak signal amplitude (in volts) as a function of depth by 18.3-mm (0.72-in.)-diameter magnetically biased bobbin coil on 25-notch EDM standard at (a) f = 100 kHz, and (b) f = 400 kHz.*
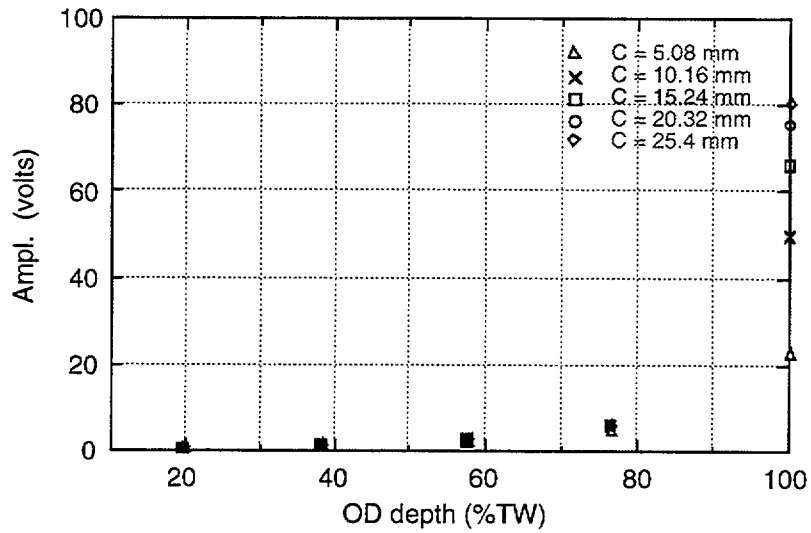
(a)
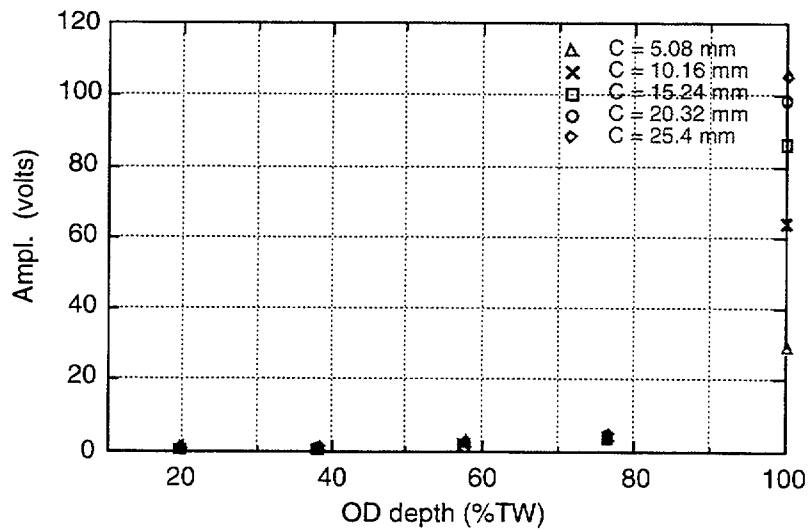
(b)

Fig. 3.10.   *Measured differential peak-to-peak signal amplitude (in volts) as a function of depth by 18.3-mm (0.72-in.)-diameter magnetically biased bobbin coil on 25-notch EDM standard at (a) f = 100 kHz, and (b) f = 400 kHz.*
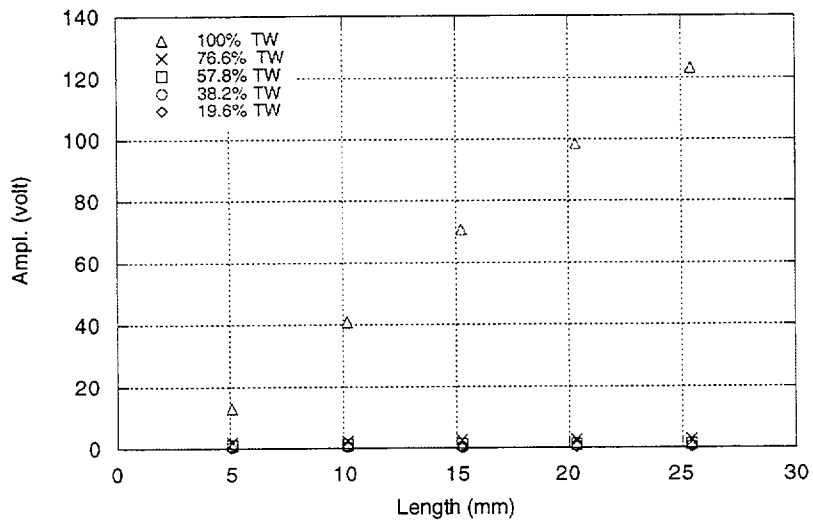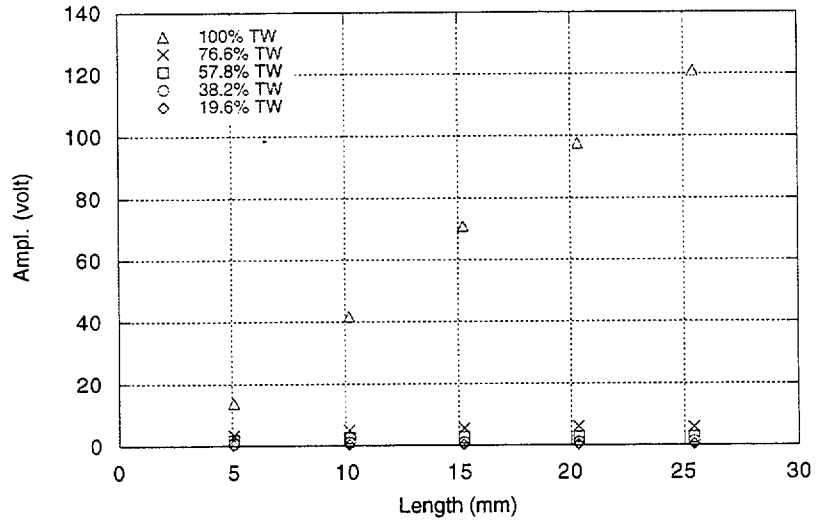
Fig. 3.11. *Measured absolute peak signal amplitude (in volts) as a function of length by 18.3-mm (0.72-in.)-diameter magnetically biased bobbin coil on 25-notch EDM standard at (a) f = 100 kHz, and (b) f = 400 kHz.*
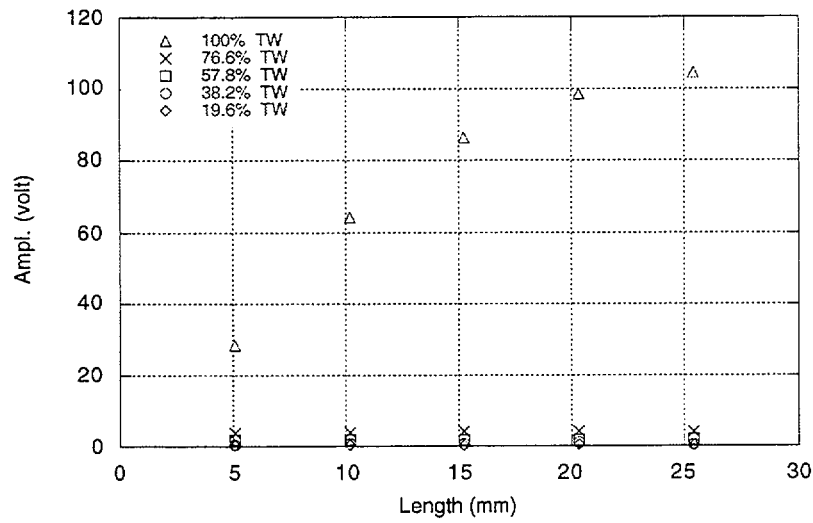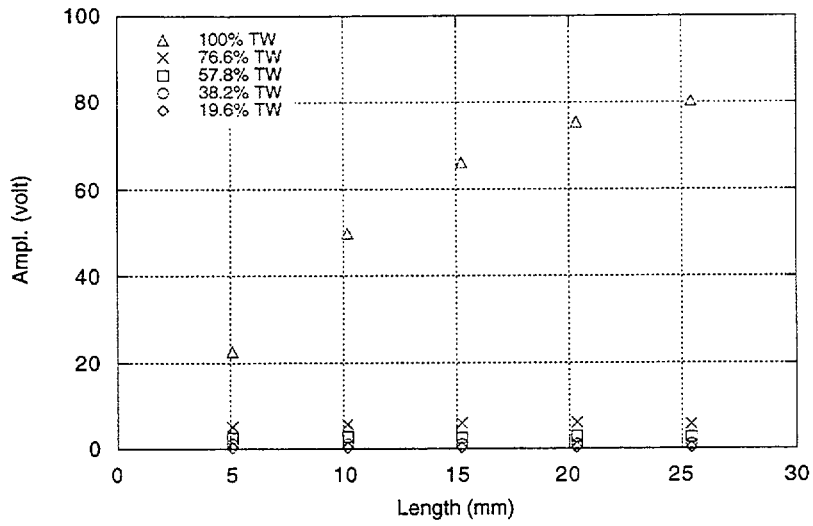
Fig. 3.12. Measured differential peak-to-peak signal amplitude (in volts) as a function of length by 18.3-mm (0.72-in.)-diameter magnetically biased bobbin coil on 25-notch EDM standard at (a) f = 100 kHz, and (b) f = 400 kHz.

It is important to note that the calibration of BC amplitude based on 20% TW drilled holes on an ASME standard tube does not imply detection of short axial cracks of comparable depth. Based on the simulated results presented here for a 6.35-mm (0.25-in.)-long axial notch, the BC probe amplitude begins to approach that of four 20% TW drilled holes for notch depths approaching 80% TW. Therefore, under realistic ISI conditions (i.e., in the presence of noise), short, shallow OD cracks (e.g., <40% TW) could go undetected during BC examinations because of their lower voltage response. It could be argued that for nonvolumetric degradations, even the 40% TW OD depth may not be a conservative estimate for BC examinations, because field induced cracks are often much tighter than machined flaws that could further degrade the signal-to-noise (S/N) ratio and, in turn, detection capability. Large differences in signal amplitude between holes and notches can be attributed to both defect geometry and probe design. In comparison to a single axial notch, the large volume of the four 20% TW OD holes in an ASME calibration-standard tube results in a much greater perturbation of the probe's impedance as a result of significant change in the volume conduction loss. The effect of the volume of a discontinuity is especially significant for BC probes for which the coil output at each axial position along the tube represents an integrated reading around the circumference.

Some general remarks should be made on comparing numerical results from this study with experimental data collected with conventional EC data acquisition instruments used for ISI of SG tubing. Although it is expected that the calculated voltage amplitudes in most cases will be in close agreement with the experimental results, various test parameters exist that cannot be accurately taken into account for simulation purposes. Typical examples include nonlinear frequency response of the probe, cable resistance and capacitance, inner winding capacitance, exact coil geometry and fill-factor, and instrument nonlinearity. These parameters, which are primarily associated with the probe and test equipment, can be accounted for with reasonable accuracy only through calibrated measurements that use laboratory instrumentation. These factors are particularly important when normalization of data is carried out in a linear fashion across different frequency channels.

3.2 Data Analysis

An objective of the SG tube integrity program at ANL is assessment of the existing models that correlate NDE results to parameters associated with tube integrity, and further exploration alternative models for improved correlations. As part of the work to study potential relationships between EC NDE parameters and SG tubing failure pressure, inspection results from the alternate repair criteria (ARC) data base on pulled and model boiler tube specimens are currently being analyzed. The degradation mechanism in this data base is limited to ODSCC at TSP intersections. Initial results of the analysis using a multivariate regression model were presented in a previous report.[2] As a continuation of this work, follow-up studies employed a standard multiple linear regression (MLR) and a neural network (NN) structure to further examine the previously established models. Because this unknown dependence is expected to be nonlinear, nonlinear models such as neural networks could serve as viable tools to explore implied relationships. Multivariate linear regression models are also employed to describe nonlinear systems.

Preliminary results are presented next on the further evaluation of two separate multivariate analysis techniques implemented to study potential relationships between BC

probe signals for ODSCC degradation at the TSP region and tube failure pressures. Representative results from test case studies that are presented here pertain to selected indications from the ARC data base that contain both model boiler and pulled tube specimens. Alternative correlation models that utilize more inclusive NDE parameters could help reduce reliance on analyst interpretation of defect signals in the presence of artifacts and background fluctuations, thus rendering more repeatable results. It should be noted that the robustness of any correlations developed here may be limited by the range of degradation morphologies and inspection artifacts included in this data base. The validity of any correlation model established here will ultimately be substantiated through laboratory testing of SG tubing specimens, including both laboratory-grown and service-induced degradations.

3.2.1 Multiparameter Correlation of Failure Pressure with Bobbin Coil Indications

Initial evaluations of correlation models that could potentially describe implicit relationships between BC readings and tube failure pressure consisted of independent analyses of pulled and model boiler tube test sets. The results of these investigations utilizing factor-based multivariate linear regression analysis were published in previous reports[1,2] and indicated that reasonable correlations could be independently developed for each category of pulled and model boiler tubes. Different signal components such as maximum, mean, and integrated signal amplitudes served as the model parameters. The signal features ultimately selected for the analyses consisted of integrated EC readings at multiple original and mix frequencies. Preliminary results of this study on pulled-tube data sets suggested that an optimal subset (i.e., minimum number of indications for an acceptable correlation) of calibration/training data should include representative indications that best describe the entire range of parameter variations for all data included for analysis. As expected, prediction confidence intervals were narrower for the model boiler test set. Subsequent attempts to develop correlation models with a combined set of pulled and model boiler specimens using similar EC test parameters and features failed to produce acceptable prediction confidence intervals. Eventually, an independent normalization procedure was devised for this analysis. An evaluation of the results based on hypothetical test case calibration and prediction scenarios utilizing a partial least-squares (PLS) algorithm was presented in a previous report.[2] Subsequently, analyses of the same data set were carried out using a standard multiple linear regression technique and an NN structure. Representative results from comparative studies to determine the prediction accuracy of each modeling approach are presented here.

3.2.1.1   Description of Data

A total of 41 TSP indications from the ARC data base were included for analysis. They consisted of 22 indications from the model boiler and 19 indications from pulled-tube specimens. All inspection results pertain to 22.2-mm (0.875-in.)-diameter tubes with a 1.27 mm (0.05 in.) nominal wall thickness. The pulled-tube indications utilized here for analysis were collected from the first three support plates on the hot-leg side of all SG units. Selected pulled-tube specimens from the same data base were incorporated from three separate plants with four SG units. Table 3.1 lists the number of specimens from each SG unit that was incorporated for analysis. Table 3.2 lists all indications that were incorporated for analysis from ARC model boiler tube data base. The decision to incorporate a tube for analysis was based on several pieces of information, with the most critical ones being the availability of

(a)   ASME calibration standard data file,

(b)   measured failure pressure, and

(c)   consistent EC inspection test frequencies.

Although transformation of EC readings among different test frequencies for similar type probes has been proposed in the past, this procedure was avoided to reduce potential uncertainties for this preliminary analysis. Figure 3.13 shows a histogram representation of the measured failure pressure distribution for both categories of indications. These plots show the difference in distribution of the available ARC tube specimens used for analysis. The pulled and model boiler tube populations better represent high and low failure pressure values, respectively. Standard normalization of multifrequency BC probe raw data that were retrieved from the ARC database was described in previous reports. All manipulations of NDE data, such as searching each file for proper channel configuration, selection of data segments that contain indications at the TSP region, normalization, resampling, and construction of mix frequency channels, were implemented off-line by a series of computer codes implemented at ANL. The normalization procedure consisted of automatic phase-angle adjustment for each channel and amplitude scaling in reference to four 20% TW flat-bottom holes on an ASME calibration standard tube. Selected data files contained inspection results at four frequencies of 400, 200, 100, and 10 kHz for both absolute and differential channels. These data were subsequently used to construct mix channel outputs. A linear two-frequency LS mix was used to reduce/suppress the TSP signal. This was carried out for 400|100, 400|200, and 200|100 mixes in which the upper frequency was taken as the primary channel. Alternatively, a three-frequency 400|200|100 mix was also implemented and provided a small improvement over the 400|100 mix for regression analysis, based on the integrated signal. The mixing algorithm was carried out for all data files whether or not the file contained a TSP indication. The number of resampled data points for all indications was chosen to cover the entire TSP region.

Selection of Normalized Features. When a parametric model is established between features derived from NDE results and those associated with the tube integrity, consistency of the selected parameters to describe viable trends in the data is of primary importance. For example, when a linear or nonlinear model based on a set of selected NDE features is trained to reach a specified error rate for predicting a subset of data, the trained model should not yield an unacceptably high prediction error when the validation data (i.e., indications not incorporated in the training set) are analyzed. To establish a unified model to map features to failure pressures for both model boiler and pulled tubes, the correlations between independent and dependent variables should be reasonably consistent for both types of tubes. Consistency refers to the same sign and similar values of the correlations.

The integrated area under each TSP indication was originally calculated according to

$$S_f^{A,D} = \sum_{n=-N/2}^{N/2} \left(\left| H_n + i * V_n \right| \right), \tag{3.2}$$

where S represents the integrated signal magnitude at frequency f for each absolute A and differential D channel. H and V are the horizontal and vertical components at each frequency. The integrated region was bounded by $N/2$ points on either side of the TSP center ($n = 0$), with the sampling rate of each data segment adjusted in accordance with the simulated TSP ring from the corresponding ASME tube standard.

Table 3.1. Composition of pulled-tube specimens from ARC data base incorporated for failure pressure analysis.

Plant	SG Unit	Indication no.
A	1	1 - 4
A	2	5 - 8
B	1	9 - 11
C	1	12 - 19

Table 3.2. Destructive examination and failure pressure measurements for 22.2-mm (0.875-in.)-diameter tubes from ARC model boiler data base containing ODSCC degradation at TSP intersections. All NDE and destructive examination (DE) measurements were carried out by Westinghouse Electric Corporation.

Specimen No.	Destructive Examination			Adjusted Pressure	
	Max. Depth (% TW)	Length[a] (mm)	Length[a] (in.)	(MPa)	(psi)
528-2	100	17.0 (12.7)	0.67 (0.5)	32.2	4,668
532-1	100	17.8 (13.2)	0.7 (0.52)	27.6	4,010
532-2	100	19.1 (14.7)	0.75 (0.58)	28.2	4,087
535-1	100	7.1 (2.8)	0.28 (0.11)	57.0	8,265
555-3	100	19.1 (10.7)	0.75 (0.42)	29.0	4,209
533-4	100	8.6 (3.6)	0.34 (0.14)	48.0	6,964
536-1	90	10.2	0.4	54.9	7,959
542-4	N/A	N/A	N/A	>33.6	>4,867
543-1	N/A	N/A	N/A	>18.2	>2,633
543-2	N/A	N/A	N/A	>21.7	>3,153
543-4	98	13.2	0.52	37.6	5,459
547-1	N/A	N/A	N/A	38.3	5,561
576-2	100	7.6 5.6	0.3 (0.22)	45.7	6,628
576-4	100	15.2 (10.9)	0.6 (0.43)	38.6	5,602
557-1	90	4.6	0.18	>51.7	>7500
557-2	100	13.2 (11.1)	0.52 (0.44)	>34.3	>4,974
557-4	N/A	N/A	N/A	80.2	11,633
558-1	100	10.2 (8.1)	0.4 (0.32)	41.2	5,969
568-1	100	8.4 (6.4)	0.33 (0.25)	44.1	6390
568-2	N/A	N/A	N/A	>32.0	>4,635
571-1	100	11.1 (8.9)	0.44 (0.35)	>34.1	>4,950
574-4	100	9.9 (8.4)	0.39 (0.33)	38.0	5,506

[a] Total crack network length with TW degradation length given in parentheses. N/A = Data not available.
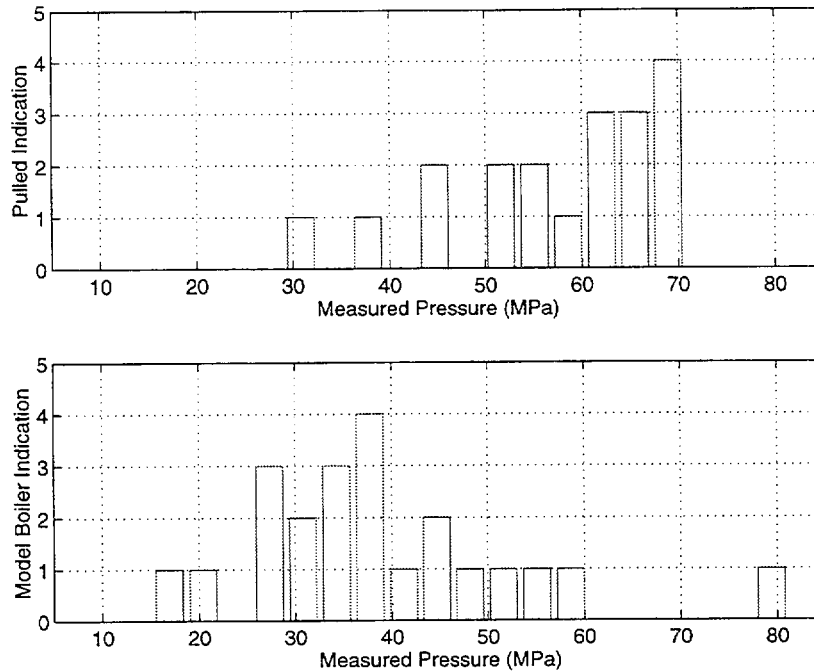
Fig. 3.13. *Distribution of pulled tube (top) and model boiler (bottom) indications as a function of failure pressure used for multivariate analysis.*

As stated in earlier studies, the features initially used for construction of correlation models for each tube category resulted in rather weak correlations for the combined data set with pulled and model boiler indications. The inconsistency between the two models could be associated with potential differences between laboratory and field specimens and NDE inspection procedures. In particular, BC probe signal amplitudes for laboratory specimens (model boiler) were generally higher than similar degradations (based on destructive results) from the pulled-tube data set. Furthermore, factors influencing the NDE measurements, such as variations among calibration standards, probe wear, dissimilarity of tube/artifact geometry (i.e., NDE carried out with or without TSP in place), and differences in defect morphologies, can further contribute to variation of the integrated BC signal along each TSP. These observations suggested that more robust features must be sought to allow for the construction of a single model that would encompass both categories of tubes. To reduce the influence of such elements on NDE data, independent normalization procedures based on the signal energy were evaluated.

Examination of the mean-centered signal traces suggested that two factors may contribute to the failure pressure variations: maximum extent and complexity of the Lissajous patterns. Consequently, an independent normalization procedure was implemented on the model parameters to reduce the effect of factors that could cause discrepancies between the selected features for the two data sets. The normalization consisted of mean-centering and energy-scaling each data segment independently. Mean-centering is done to reduce the effect of signal offset, and energy-scaling is used to render equal weight for each data segment. With reference to Eq. 3.2, the transformed variables were calculated according to

$$\hat{S}_f^{A,D} = \sum_{n=-N/2}^{N/2} \left(\left| \hat{H}_n + i * \hat{V}_n \right| \right),$$ (3.3)

with the new transformed $\hat{H}$ and $\hat{V}$ components defined as

$$\hat{X}_n = \left(X_n - \mu^X \right) \big/ \sigma^X,$$ (3.4)

or

$$\hat{X}_n = \left(X_n - \mu^X \right) \big/ \xi^X,$$ (3.5)

where μ and ξ^x represent the sequence mean and the square root of the signal energy, respectively. For equal-length mean-centered signal components, ξ is proportional to the standard deviation σ^X of each trace. It should be noted that transformation in accordance with Eq. 3.5 will retain the original impedance plane signal shape (i.e., Lissajous trace). Alternatively, the trace mean instead of the integrated value may be used in the calculation of the parameters described by Eq. 3.3. This was found to be particularly advantageous when slight variations exist between the lengths of data segments. For the available data set, the analysis results showed negligible differences in the predicted results using either Eq. 3.4 or 3.5.

Subsequently, linear and nonlinear predictors based on the above features were examined in an attempt to exploit any correlations between the new features derived from the eddy current measurements and the failure pressure values. These features served as the input parameters for the two separate correlation models described next. The correlation between the measured failure pressures, P_{meas}, and the predicted failure pressure, P_{pred}, was taken as a measure of the effectiveness of the predictors. The correlation is generally defined as:

$$C = E\left\{ \frac{(P_{meas} - \overline{P}_{meas})(P_{pred} - \overline{P}_{pred})}{\sigma_{meas} \, \sigma_{pred}} \right\},$$ (3.6)

where E denotes the expected value and the bar refers to the mean value. The correlation coefficient can take values between -1 and 1. A value of $C = 1$ indicates that the predicted failure pressures correspond exactly to the actual failure pressures. A value of $C = 0$ suggests that the predicted failure pressures have no relationship to the actual failure pressures. A negative value of C indicates that correspondence between the actual and predicted failure pressures is inverted.

Three separate training and prediction schemes were subsequently employed to evaluate the ability of each correlation model in capturing all the useful trends in the data. These are abbreviated as

All: Information from all (both model boiler and pulled tubes) indications are used to establish the predictor.

LOOT: Leave-one-out technique (LOOT), i.e., a sampling-with-replacement, where the information from all but one tube is used to establish the predictor. The predictor is then used to predict the failure pressure of the one sample not used for training. The procedure is repeated until a prediction result is obtained for all indications available in the data base.

Mixed: Information from half of randomly selected samples is used to establish the predictor, which is then used to estimate the failure pressures of the remaining half.

3.2.1.2   Analysis of Results

Initially, all available original and mix channel signals (a total of 14 components) were incorporated for multivariate analysis to determine the best fit to the data, as well as to identify the minimum number of independent variables that best describe all variations in the data. Based on examination of the correlation coefficients, eight components were eventually chosen for parametric studies. They consisted of differential and absolute channels at 400 and 200 kHz, as well as 400|200|100 and 400|200 mixes. Test cases were then carried out to examine the stability of each correlation model.

Figures 3.14(a) and (b) display the multivariate regression and the neural network (NN) fits, respectively, when all samples were incorporated for the model building stage. Also shown are the upper and lower bounds of the 95% confidence intervals calculated through a first-order LS fit to the measured vs. predicted pressures. As expected, the NN has better capability in capturing all of the variations in the data. However, it should be noted that this test case is not representative of the predictive capability of the model, but rather of the ability of the model to construct a fit to the entire data. Figure 3.15 displays the prediction results of the two models when ≈50% of the indications from each tube category were included in the training stage. For this test case, comparable confidence intervals are achieved by both methods. Finally, Fig. 3.16 displays the prediction results of the two models based on the LOOT training and prediction scheme. Once more, the confidence intervals for both methods of fitting indicate comparable prediction accuracy.

The following general observations can be made regarding the results of this study. Based on the sufficiently high values of correlation coefficients for the case when all samples are used for training, the structure of both linear predictors and NNs are capable of capturing any implicit trends that may be present in the data. The LOOT training scheme possibly provides the most conservative estimate of the accuracy of the predictors. The results suggest that normalized features provide more consistent inputs to the predictors. Another aspect, not shown here, is that in comparison with normalized features, training of the NN using the original NDE parameters requires much longer training times for the same prescribed convergence criteria; this is a further indication of the lack of trends in the original data when both categories of specimens were analyzed. Once again, the results here suggest that with normalized features, the best prediction results are obtained when the training set is composed of both pulled and model boiler specimens that represent the entire range of variation in the data set. For failure pressure prediction accuracy, the linear prediction method performs nearly as well as the NN, which suggests that the input-output relationships between selected features and tube failure pressure are primarily linear. Statistical analyses

of the prediction error also confirmed that performances of the multiple linear regression and NN are generally comparable for the specific data set used in this study.

A major objective of the multivariate regression analysis technique currently under study at ANL has been to reduce the influence of NDE-related factors discussed above. More inclusive NDE parameters (i.e., signal features) such as the integrated BC probe signal over the entire degraded region can presumably reduce the effect of operator variability. Furthermore, the renormalized integrated signal, in theory, should better reflect variations of cracking morphology along the entire tube-to-TSP intersection as all potential indications are incorporated. Consequently, it is expected that the signal features considered in this study should better account for the outlier samples. An outlier is defined here as a specimen with a low voltage indication and a low failure pressure or a high voltage indication and a high failure pressure. Further studies on the application of multivariate regression models and NN structures for both direct and indirect correlation of NDE results with tube structural integrity are currently being pursued. The results of these efforts will be presented in future reports.
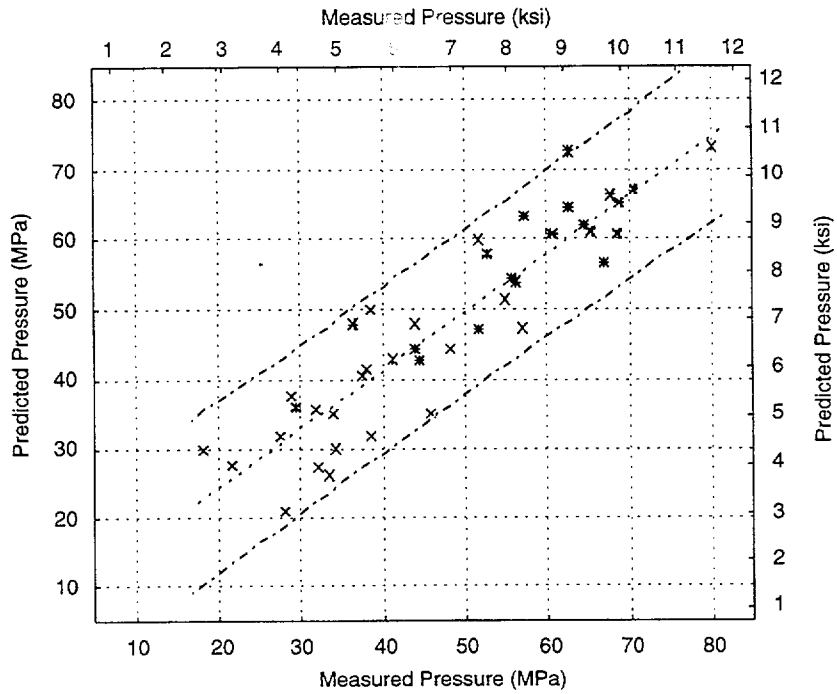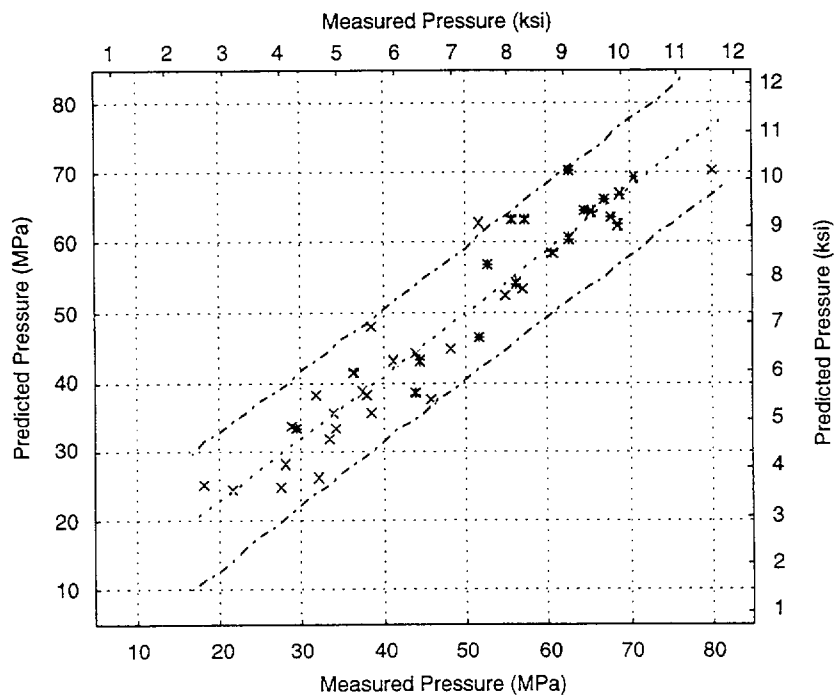
Fig. 3.14. *Distribution of pulled tube (a) and model boiler (b) indications as a function of failure pressure used for multivariate analysis. Also shown are upper and lower bounds of 95% confidence interval based on linear LS fit to data.*
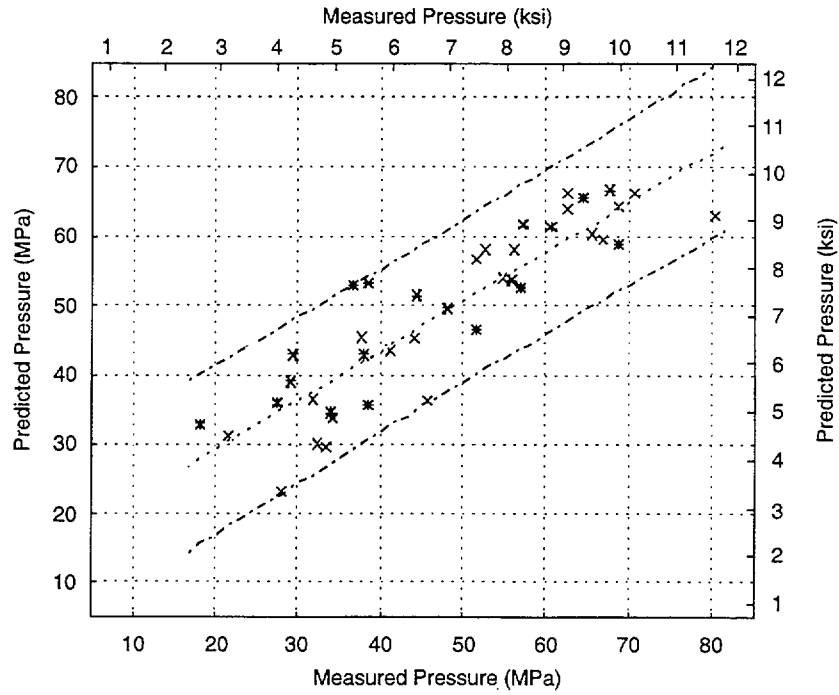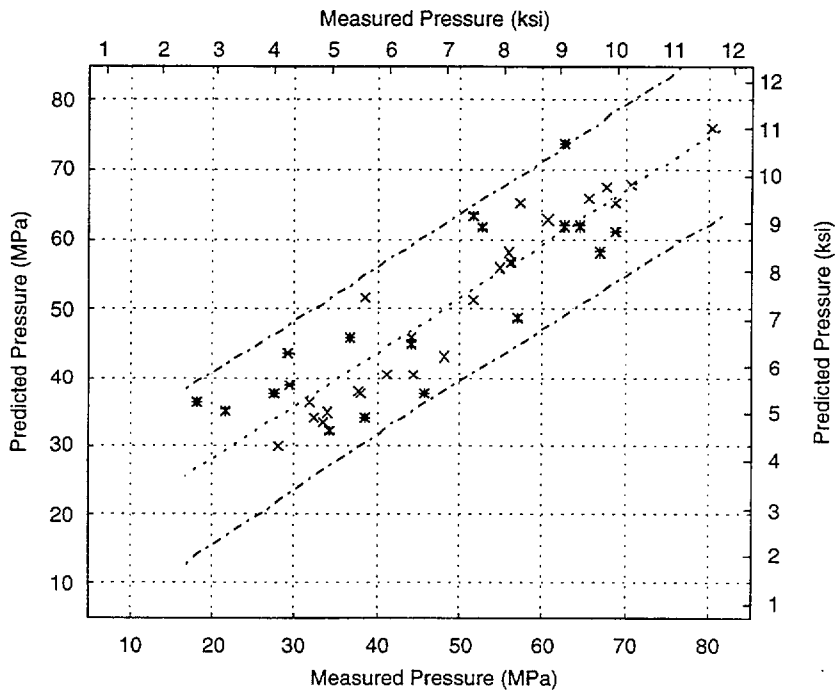
Fig. 3.15. (a) Regression- and (b) neural network-predicted versus measured failure pressure when 50% of model boiler (x) and pulled-tube (*) indications were randomly selected for training. Also shown are upper and lower bounds of 95% confidence interval based on linear LS fit to data.
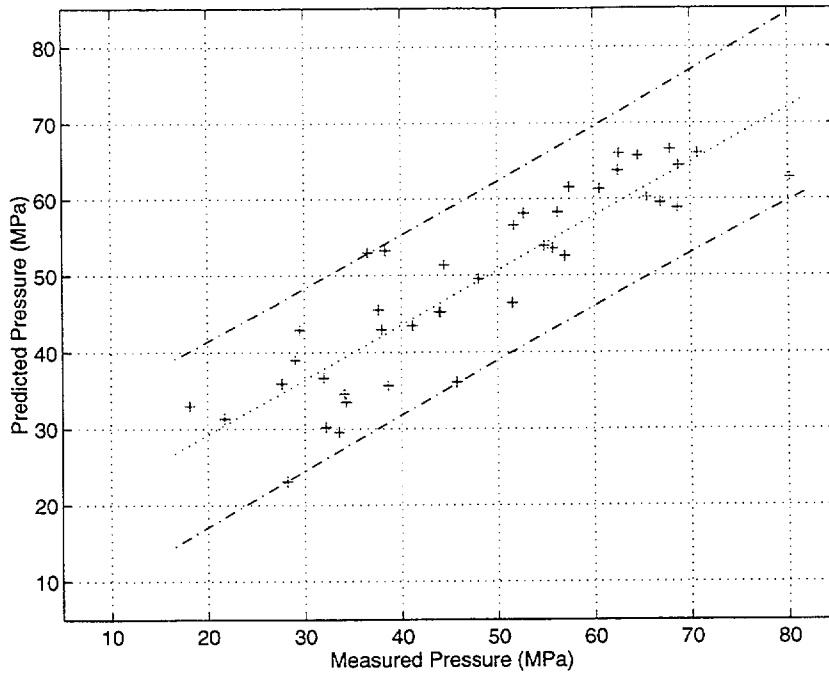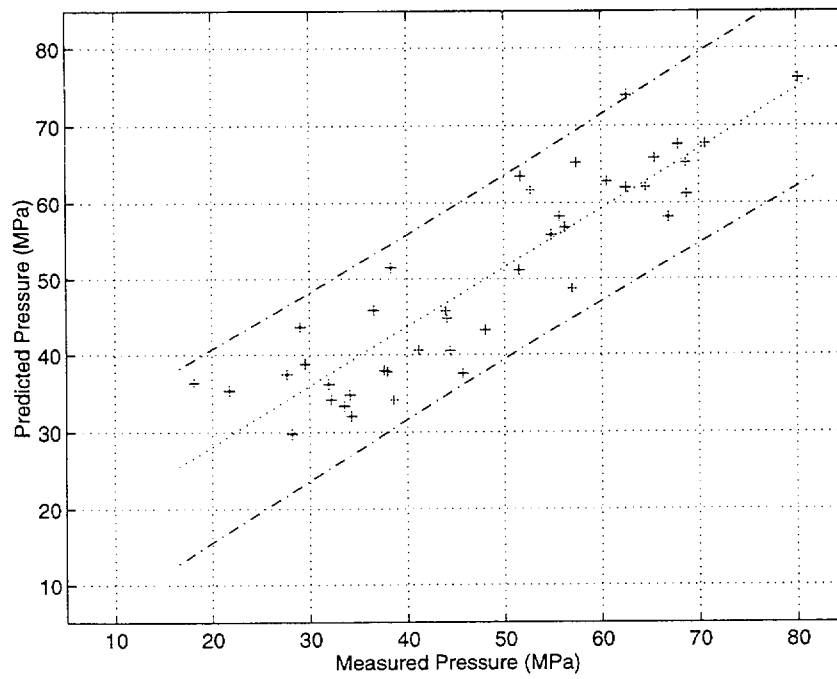
Fig. 3.16. (a) Regression- and (b) neural network-predicted versus measured failure pressure for model boiler (x) and pulled-tube (*) indications using a LOOT training and prediction method. Also shown are upper and lower bounds of 95% confidence interval based on linear LS fit to data.

4 Research on Degradation Modes and Integrity (K. E. Kasza, S. Majumdar, J. Y. Park, W. J. Shack, and D. R. Diercks)

4.1 Production of Laboratory Degraded Tubes

Because degraded tubing from operating or retired SGs is difficult and expensive to obtain and the availability of such tubing is limited, it is necessary to produce prototypical degradation in tubes as part of this program. These cracked tubes will be used to evaluate of NDE equipment and techniques in the SG tube mock-up and for pressure and leak-rate testing. Two techniques have been developed for the production of laboratory-degraded tubes under accelerated conditions, namely (a) exposure to highly caustic solutions in a high-temperature pressurized autoclave system[3] and (b) exposure to sodium tetrathionate at room temperature and atmospheric pressure. Although the autoclave technique has been used with some success in the earlier stages of the program, cracking in sodium tetrathionate at room temperature has proven to be much simpler and faster, and all of the specimens described here were produced by this technique.

4.1.1 Production of Cracked Tubes

The production of laboratory-degraded tube specimens continued throughout the reporting period, and a substantial number of 22.2-mm (7/8-in.)-diameter Alloy 600 tubes (Heat no. NX8527) have been subjected to the cracking treatment to date. These tubes were cracked by exposing them to a 1M sodium tetrathionate solution ($Na_2O_6S_4 \cdot 2H_2O$) at room temperature and atmospheric pressure. A small amount of boric acid (1.69 g H_3BO_3 in 100 ml H_2O) was added to the solution for some of the early exposures (specimens SGL-0001 through SGL-0012) but produced no discernible beneficial effect and its use has been discontinued.[2] Prior to exposure to the tetrathionate solution, the specimens are solution-heat-treated at 970-1130°C for 5-15 min and aged at 600-750°C for 5-48 h to produce a microstructure that is susceptible to cracking.[2] This heat treatment results in grain boundary precipitation and a reduction in the hardness and flow stress of the material. A correction for this effect on mechanical properties will be required when these tubes are used for subsequent pressure and leak-rate testing. This heat treatment can also influence the EC NDE response of the tubes to some extent. During the reporting period, the tube cracking facilities were modified to produce 304.8-mm (12-in.)-long tubes rather than the 285.8-mm. (11.25-in)-long tubes produced previously, and additional rigs were constructed for production of skewed OD, axial OD, and axial ID SCC.

The cracks are detected by visual inspection and confirmed by nondestructive EC tests. Figures 4.1 and 4.2 show a macroscopic view of throughwall circumferential ODSCC in Specimen SGL-033 and the EC test results of the tube. Variations in penetration depth or multiple cracking are indicated in the figures. Degradation with multiple throughwall circumferential ODSCC in Specimen SGL-040 is shown in Fig. 4.3. Two nearly parallel circumferential ODSCC cracks are separated by about 5 mm. Figure 4.4 is an EC NDE result of nonthroughwall circumferential ODSCC in specimen SGL-063, showing secondary multiple cracks. Figure 4.5 shows the EC test results for a throughwall axial ODSCC in specimen SGL-065. Figure 4.6 shows the eddy current NDE result for a axial OD crack in specimen SGL-273 that may have a ligament between two short throughwall segments. Figure 4.7 is an

eddy current NDE result for a more complex geometry of cracks introduced into specimen SGL-289. Multiple axial OD cracks and some circumferential components of the cracks are shown. The cracks penetrate throughwall, and the length of individual cracks is <7 mm (0.3 in.) on the OD surface. Ten tubes (tube nos. SGL-130-132 and 277-282) contain a laboratory simulation of the roll-transition. Figure 4-8 is an EC NDE result for degraded tubes (SGL-282) with the roll transition simulation. Indications of 360° circumferential ODSCC and an artifact from a steel collar tool are shown in the figure. Some of the degraded tubes were sectioned through the SCC for metallographic examination. Figures 4.9 and 4.10 are optical photomicrographs of unetched cross sections of the cracks in specimens SGL-115 and SGL-116. Tight intergranular SCC penetrated 4.3 mm (34% TW) in specimen SGL-115 and 2.8 mm (22% TW) in specimen SGL-116, respectively.

To examine the influence of oxide film on EC response, five cracked tubes (SGL-127, 149, 169, 189, and 197) were immersed in deionized high-purity water with 3 ppm dissolved oxygen at 290°C for 120 hours and in a simulated primary water environment (1200 ppm B and 2 ppm Li) at 320°C and 12.4 MPa (1800 psi) for 1400 h. The tubes were examined with eddy current NDE before and after the treatments. Results are given in Section 2.1.2. Oxidation treatments on five additional cracked tubes (SGL-114, 159, 170, 182, and 187) are being performed in deionized high-purity water with 8 ppm dissolved oxygen at 290°C and 1280 psi.

A technique to deposit Cu onto laboratory-degraded Alloy 600 tubes has been developed. Copper was galavanically deposited on tube surfaces in an aqueous solution of 10% $CuSO_4$-10% H_2SO_4. The anode material was Fe. Four degraded specimens were treated: SGL-057 and SGL-058 with circumferential ODSCC and SGL-089 and SGL-090 with axial ODSCC. Eddy current NDE will be performed before and after the Cu deposition to examine its effects.

4.2 Model Boiler Tube Cracking Facility

Secondary-side SG tube SCC is a major degradation mechanism in nuclear power plant SGs. A model boiler multitube corrosion cracking facility designed to closely simulate SG thermal-hydraulic and chemistry conditions for the tube/crevice geometry has been partialy assembled. In particular, heat transfer conditions across the tube wall in this facility will be maintained to produce chemical concentration of impurity species in secondary side crevices and thereby promote SCC at the tube OD. This facility will thus permit the production of cracked tubes under nearly prototypical conditions. These cracked tubes will be used in pressure and leak-rate tests and for NDE characterization at ANL. The facility can also be used to study SCC at a more mechanistic level.

The design features of the facility were described in detail in the previous annual progress report.[2] As stated in that report, detailed hardware specifications have been completed for all facility components, and requests for component fabrication bids were issued. The fabricator delivered the boiler to ANL in March 1997, but further assembly was delayed so that programmatic resources could be concentrated on other activities in the program.
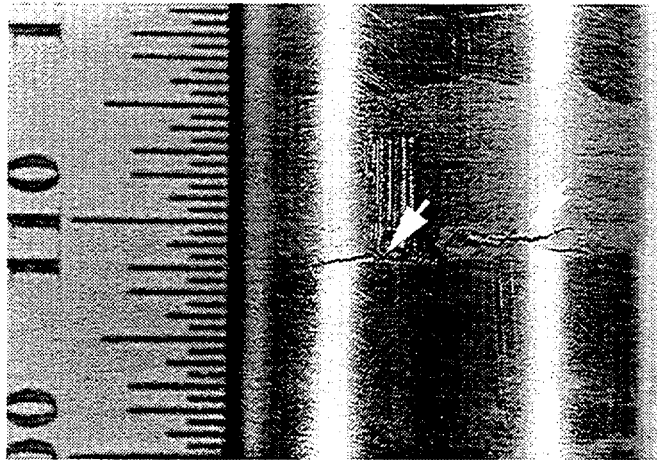
Fig. 4.1. *Laboratory-degraded throughwall circumferential ODSCC in 22.2-mm (7/8-in.)-diameter Alloy 600 (heat no. NX8527) tube specimen SGL-033.*
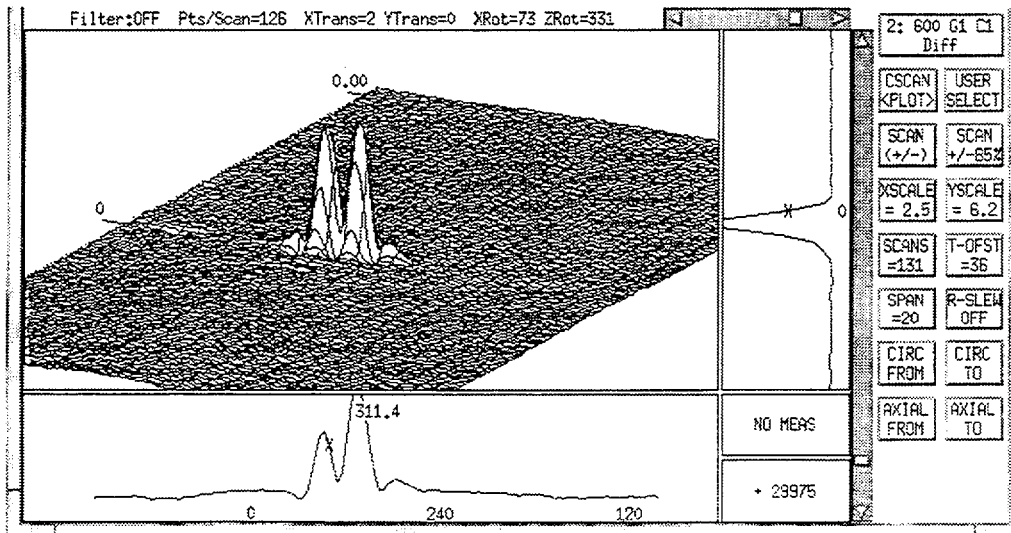
Fig. 4.2. *Eddy current test of degraded throughwall circumferential ODSCC in 22.2-mm (7/8-in.)-diameter Alloy 600 (heat no. NX8527) tube specimen SGL-033.*
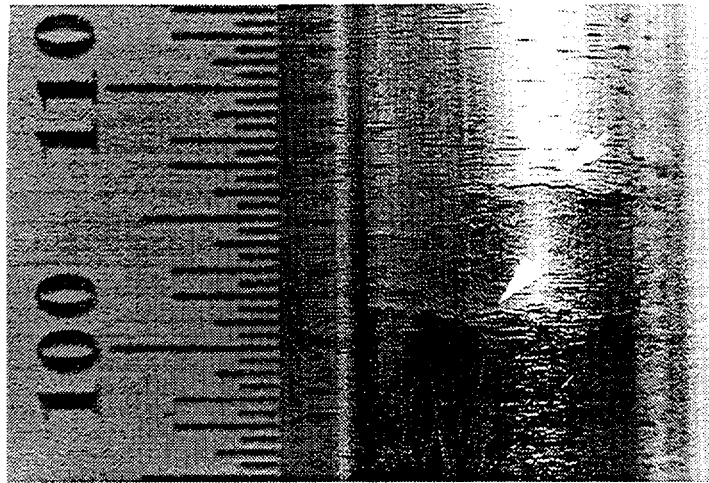
Fig. 4.3. *Laboratory-degraded multiple circumferential ODSCC in 22.2-mm (7/8-in.)-diameter Alloy 600 (heat no. NX8527) tube specimen SGL-040.*
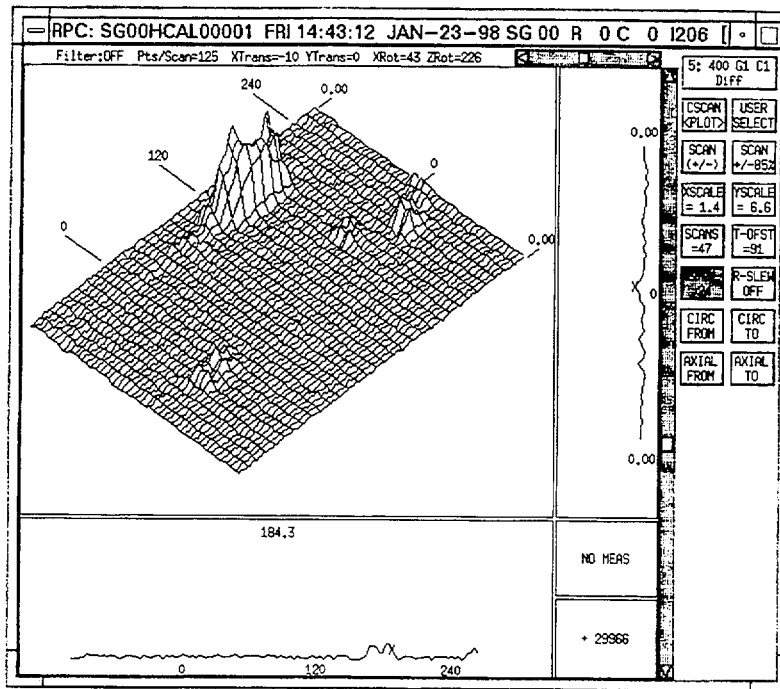
Fig. 4.4. *Eddy current test of laboratory-degraded circumferential ODSCC in 22.2-mm (7/8-in.)-diameter Alloy 600 (heat no. NX8527) tube specimen SGL-063.*

Filter:OFF Pts/Scan=124 XTrans=-2 YTrans=0 XRot=43 ZRot=222

9: 300 G1 C1
Diff

CSCAN <PLOT>   USER SELECT

SCAN (+/-)   SCAN +/-95%

XSCALE = 1.4   YSCALE = 6.6

SCANS =47   T-OFST =91

SPAN =44   R-SLEW OFF

CIRC FROM   CIRC TO

AXIAL FROM   AXIAL TO

119.0

NO MEAS

+ 29335
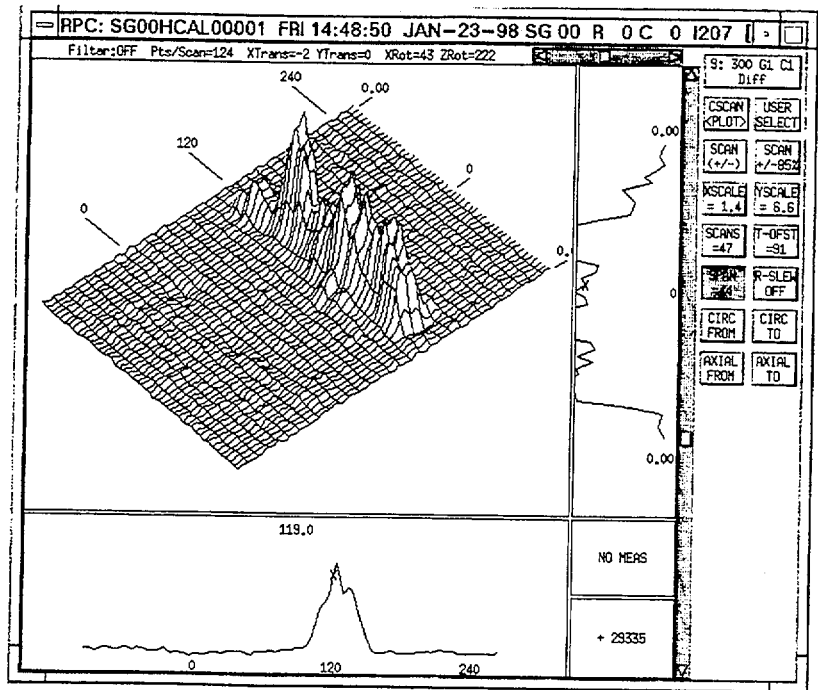
Fig. 4.5.   *Eddy current test of laboratory-degraded throughwall axial ODSCC in 22.2-mm (7/8-in.)-diameter Alloy 600 (heat no. NX8527) tube specimen SGL-065.*

RPC: SG00HCAL00001 THU 14:11:37 JUL—16—98 SG 00 R 0 C 0 I127 [MB]

Filter:OFF Pts/Scan=124 XTrans=2 YTrans=0 XRot=60 ZRot=332

9: 300 G1 C1
Diff

CSCAN <PLOT>   USER SELECT

SCAN (+/-)   SCAN +/-95%

XSCALE = 1.5   YSCALE =6.7

SCANS =31   T-OFST =0

SPAN =32   R-SLEW OFF

CIRC FROM   CIRC TO

AXIAL FROM   AXIAL TO

180.0

NO MEAS

+ 25164
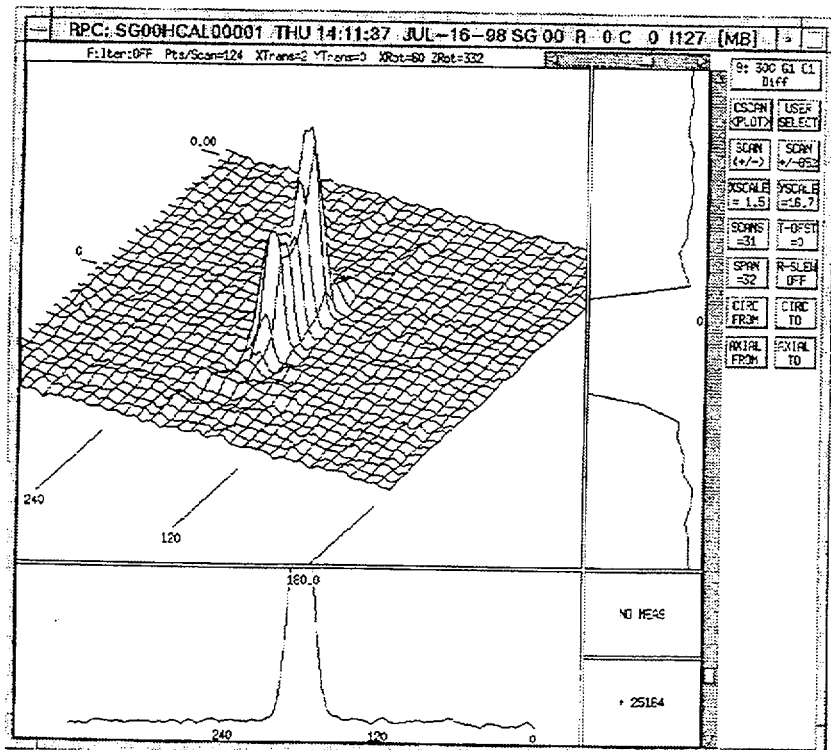
Fig. 4.6.   *Eddy current NDE of axial ODSCC in Alloy 600 (heat no. NX8527) tube specimen SGL-273. Two short throughwall cracks may be connected by a ligament.*
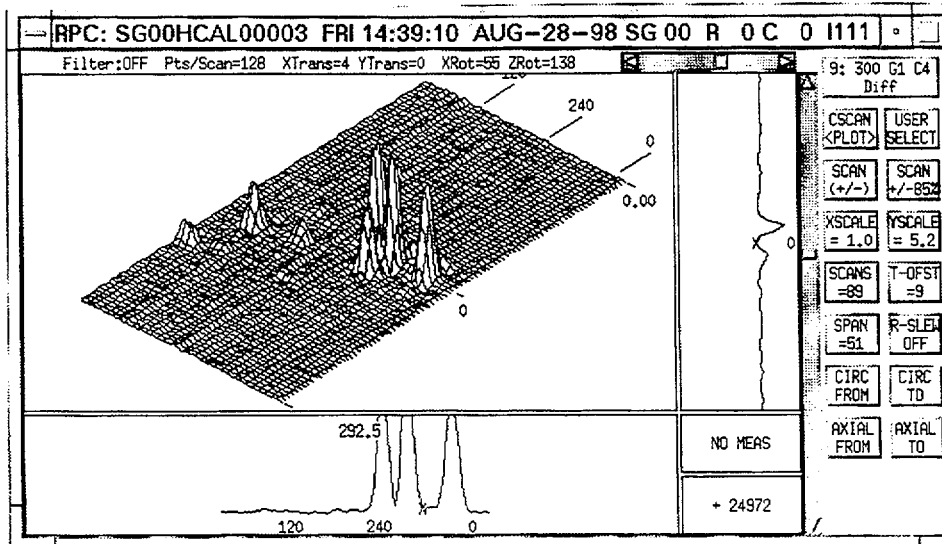
Fig. 4.7.   Eddy current NDE of multiple axial ODSCC in Alloy 600 (heat no. NX8527) tube specimen SGL-289.   Circumferential components of SCCs are also seen around tube.
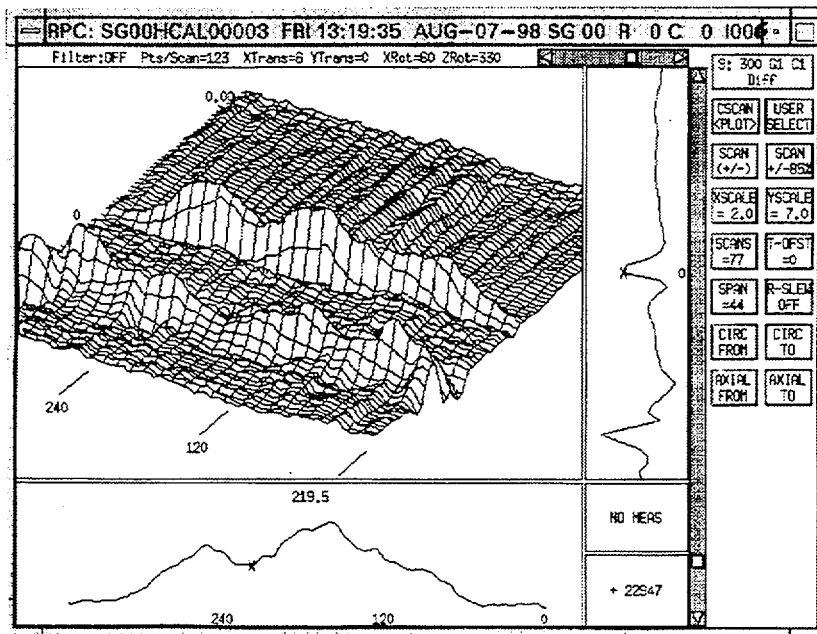
Fig. 4.8.   Eddy current NDE of circumferential ODSCC in Alloy 600 (heat no. NX8527) tube specimen SGL-282, simulating a roll-transition crack. Indications of circumferential ODSCC (top) and an artifact from a steel collar (bottom) are also shown.
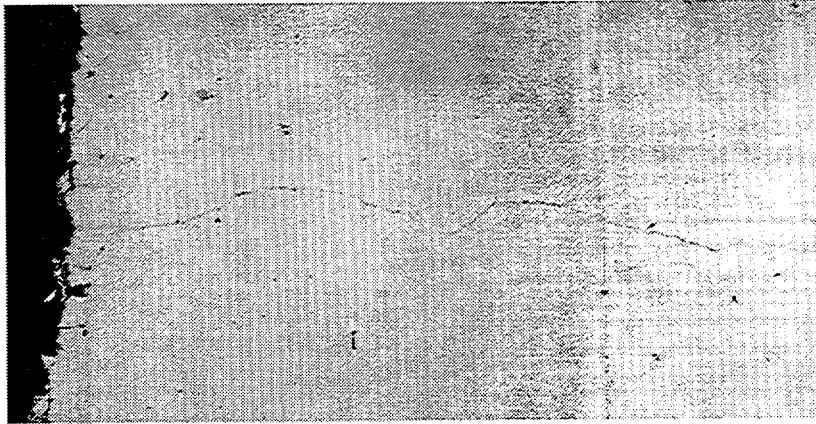
Fig. 4.9.   Cross section of laboratory-degraded 22.2-mm (7/8-in.)-diameter Alloy 600 (heat no. NX8527) tube specimen SGL-115 with axial IDSCC. 433 X.
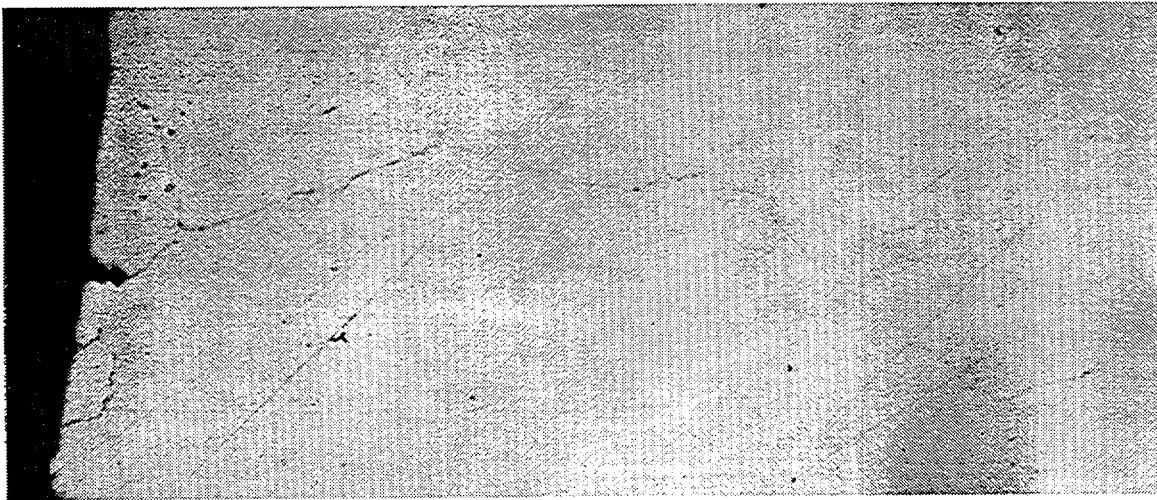
Fig. 4.10.   Cross section of laboratory-degraded 22.2-mm (7/8-in.)-diameter Alloy 600 (heat no. NX8527) tube specimen SGL-116 with axial IDSCC. 433 X.

4.3 Pressure and Leak-Rate Test Facility

The Pressure and Leak-Rate Test Facility, a unique facility for evaluating the leakage and structural integrity of flawed SG tubes, has been completed during this reporting period. The facility is designed to operate under prototypical PWR conditions. The facility underwent checkout, shakedown, and performance qualification from October 1997 through April 1998, and testing of various types of flawed tubes was initiated in May 1998. These activities are described below.

4.3.1 Facility Description

The Pressure and Leak-Rate Test Facility is being used to obtain data on failure pressures, failure modes, and leak rates of flawed tubing at temperatures up to 343°C (650°F), pressures up to 21 MPa (3000 psi), and pressurized-water flow rates up to 1520 L/min (400 gal/min). Available information on the design and performance of previous facilities was reviewed in the design of this facility, and it incorporates several features that are necessary to obtain prototypical data under stable, controlled conditions. A photo of the facility, which was described in detail in the previous annual report[2] is shown in Fig. 4.11, and a schematic diagram is provided in Fig. 4.12.

Briefly, the important features of the facility are (a) a large heated blowdown vessel water inventory of ≈760 L (200 gal) to ensure a high and stable flow rate capability and to permit full-range testing of initially stable leaking cracks to instability; (b) piping and valves of a size sufficient to minimize pressure drop in the supply line to the flawed tube and thereby permit high flow rates; (c) the use of nitrogen cover gas pressurization in the blowdown vessel and a downstream back-pressure regulator valve to control tube pressure differential, thereby minimizing nonprototypical two-phase flow from entering the tube; (d) computer feedback valve control to allow rapid pressure control; and (e) a tube test module containment vessel shown in Fig. 4.13 that can hold tubes of ≈0.15-1.0 m (6-40 in.) in length. The test module can also be fitted with support stings to simulate support plate constraints on flawed tubes or enable tests to explore the impact of a flaw jet on an adjacent tube.

The tube pressure differential is ramped up in a series of plateau increases by the back-pressure regulator valve located downstream from the test module containment vessel or by increasing the nitrogen cover gas pressure in the blowdown vessel. Both modes of operation can be carried out under manual or computer control. In the computer-controlled mode, the pressure can be programmed to simulate a prototypical transient pressure history. Blowdown vessel pressurization is achieved by the use of regulated feedback nitrogen cover gas pressurization from a 30 MPa (4400 psi) outdoor tank system of 0.9659 ML (34,110 standard ft³) capacity. Flaw leakage exiting the test module is routed outdoors through a large pipe to minimize back pressure and is discharged into a large muffler for noise suppression. During the ramp-up of pressure, information on tube flaw flow rate, pressure differential, and temperature are recorded as a function of time.

Ramp-up of the tube differential pressure is terminated when the tube flaw becomes unstable (i.e., the tube ruptures, causing a dramatic increase in Q) or when the water level in the blowdown vessel becomes too low. For large flaws, the rupture pressure will be considerably less than 21 MPa (3000 psi), and high flow rates are achieved. Under these conditions, short-duration tube pressure plateaus of only a few seconds are used, and crack flow rates of ≈400 gal/min have been achieved and measured. For short, tight flaws with
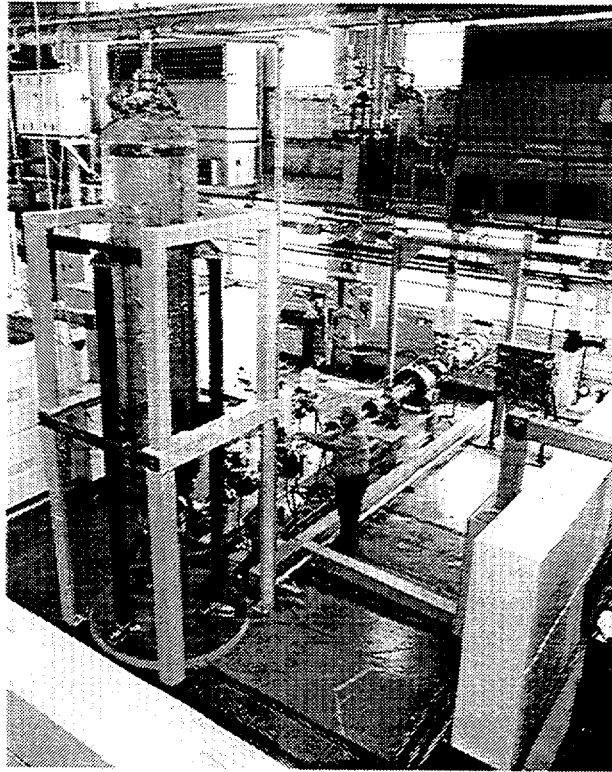
Fig. 4.11 Pressure and Leak-Rate Test Facility

considerably lower flow rates, the time available for testing can extend to more than a day. A turbine flowmeter is located immediately upstream of the test module to monitor the leak rate. Load cells in the support legs of the blowdown vessel are used to monitor the mass of the water in the blowdown vessel as a function of time, thereby providing a backup to and cross check of the flowmeter.

4.3.2 Facility Checkout, Shakedown, and Performance Qualification

During the first half of this reporting period, facility checkout, shakedown, and performance qualification testing were performed at room and elevated temperature over the full range of operation pressure. The most significant of these activities are summarized here.

Performance of the ASME-Code-required overpressurization relief valve protection for the entire system was verified. This checkout was performed under a worst case scenario, namely with the outdoors gas system pressurized to 30 MPa (4400 psi), the blowdown vessel filled with 760 L (200 gal) of water and pressurized to 21 MPa (3000 psi), the maximum allowable working pressure (MAWP) for the blowdown vessel, and no water flow out of the vessel. For this relief valve test, all control valves on the gas supply system were held wide open except for a 50-mm (2-in.) solenoid rapid opening full port ball valve, which was initially closed and then opened, allowing the full 30 MPa (4400 psi) gas storage system flow to begin moving through the supply line and past the relief valve into the blowdown vessel. The pressure in the blowdown vessel cover gas head space was monitored, and the test verified that the blowdown vessel pressure rise above the maximum allowable working pressure (MAWP) was limited by the
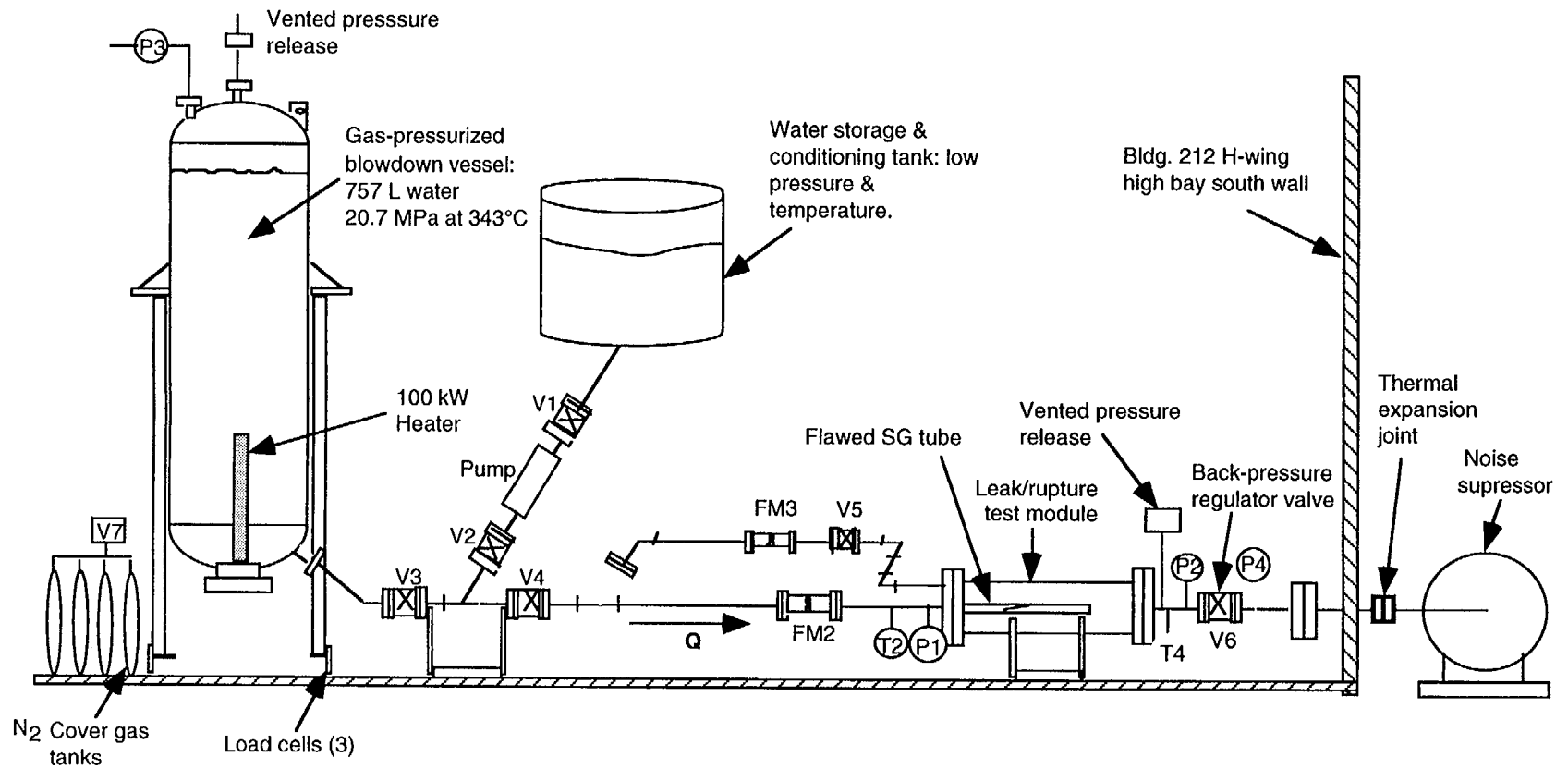
Fig. 4.12. Schematic diagram of Pressure and Leak-Rate Test Facility.
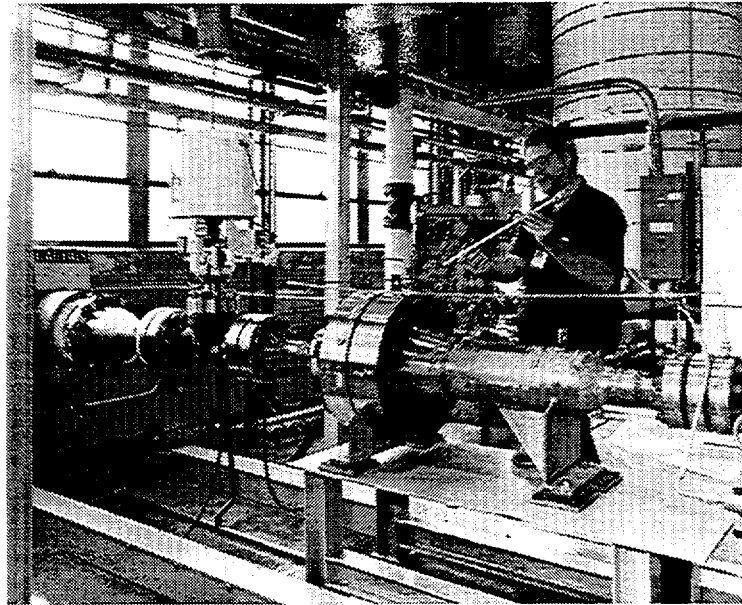
Fig. 4.13. Test module and typical tube specimen

opening of the relief valve to only ≈2% of the vessel MAWP, which is considerably less than 10% rise permitted by ASME Code.

Tests were also conducted to verify the ability of the blowdown vessel gas pressurization system controls to maintain a constant cover gas pressure at 0-21 MPa (0-3000 psi) and water flow rates out of the blowdown vessel of 0.04 to >760 L/min (0.01 to >200 gpm) into the test module that houses the test specimen. These tests were conducted with room-temperature and 282°C (540°F) water. During these performance tests, valves V3 and V4 on the 50-mm (2-in.) flow pipe connecting the blowdown vessel to the test module, and back-pressure control valve V6 downstream of the test module were used to regulate the flow out of the blowdown vessel (see Fig. 4.12). No flawed SG tube was installed in the test module. These tests showed that under some conditions of rapid change in water flow rate, the computerized controlled gas pressurization supply valve had a tendency to overrespond and then return to the desired cover gas pressure. Because even brief overpressurizations beyond the set point can induce irreversible structural changes in a flawed tube, such excursions are unacceptable. The gas control valve tuning parameters and facility operation procedures underwent several modifications to successfully eliminate this behavior. The cover gas pressure variation from the desired set point was finally reduced to less than the 1% maximum variation set forth in the design specifications for the facility.

The performance of the two methods for measuring tube leak flow rate, i.e., the turbine flowmeter in the water flow line upstream of the test module and the blowdown vessel load cells, was also verified. Good agreement between the two flow rate readings was obtained. The turbine flowmeter low end reading was determined to be ≈11 L/min (3 gpm) before the turbine stopped turning. The load-cell tank weighing method was found to be sensitive to water inventory changes of 1 kg (0.5 lb), thus providing water flow rate readings down to tenths of a liter per minute.

The pressure vessels and piping were thermally cycled several times between room temperature and 282°C (540°F) and pressurized up to 19 MPa (2800 psi) as a check on the

high-pressure leak tightness of the thick-wall components (the blowdown vessel walls are 64 mm [2.5 in.] thick). This thermal cycling also verified system design features that were incorporated to accommodate the structural thermal expansions arising from heatup. No leaks were created by the thermal cycling, and the thermal expansion joint located outside the facility wall, immediately upstream of the large exhaust muffler, accommodated the ≈25 mm of thermal elongation in the main pipe flow line at the highest temperature. These thermal cycling tests were conducted with the facility completely insulated and all electrical trace heating operating.

The high-pressure and high-temperature hardware of the facility is designed to operate under repeated cycling between ambient conditions and prototypical steam generator operating conditions. However, the thick walls of the facility components and piping require electrical trace heating to limit the temperature difference across the pressure boundaries and thereby maintain vessel stresses at acceptable limits. The trace heating on the piping connecting the blowdown vessel to the test module (where the flawed tube undergoing test is located) is also used to keep the piping at the same temperature as the water during testing. Without the trace heating, the superheated water from the blowdown vessel would be cooled considerably as it flows through the massive cooler connecting piping, particularly for low flow rates at the beginning of a test. This would result in variable water leak temperatures during the test. The proper functioning of the controllers and the ability to maintain the piping and water temperatures within specified limits at elevated temperature have been verified. The electrical 100-kW flanged heater mounted in the bottom of the blowdown vessel performed very well at all temperature levels, and all control features, including the over-temperature protection features of the heater and the facility electrical power emergency shutoff, performed to specifications.

The facility computer data acquisition system (DAS) used to record the tube test data has been configured and checked out. This system consists of a Power Macintosh 8500 computer with National Instruments hardware. The DAS has various computer monitor data display windows for monitoring facility operation, such as facility heatup and approach to test readiness, as well as actual flawed tube leak rate and pressure data.

In order to see long-term facility trends in approaching the desired test conditions during heatup and pressurization, a window displays graphical plots of various temperatures and pressures over the period of several hours required to achieve elevated test temperatures. Data recorded during a test is displayed graphically and is then transported by floppy disk to a second facility computer for analysis.

Facility control procedures were also developed and streamlined in order to maximize the number of tube pressure plateaus that can be tested for the available water inventory in the blowdown vessel. Depending upon the pressure level, leak flow rate, and whether the flaw is part or throughwall at the beginning of the test, sufficient time is available to achieve stable pressure and flow response for as few as 2 or as many as 20-30 plateaus over the course of a test. The time required to prepare the facility for testing and the recycle time between tests depend strongly on whether testing is conducted at room temperature or elevated temperature. As expected, test frequency is much higher for room-temperature testing.

The following summarizes some of the considerations that influence facility test recycle time and the number of tests that can be conducted per week.

Elevated-temperature tests (two tests per week)

- Massive thick-wall components require 5-6 hr heatup to achieve 282°C (540°F).

- Overnight cooldown is required before removing the specimen from the test module.

- Specimen change requires 4 h for opening and reclosing the high-pressure bolted crushable metal gasketed flanges on the heavy piping upstream of test module and reinstallation of the insulation and instrumentation.

- Nitrogen storage tanks require overnight pressurization to achieve 30 MPa (4400 psi).

- Refill of the blowdown vessel with 760 L (200 gal) of deionized water requires 2.5 hours.

Room-temperature tests (five tests per week)

- No time required for heatup or cooldown.

- About three hours is required to open and close the high-pressure flanges on the test module.

In summary, safe facility pressure and temperature control was verified under conditions of both a step change and a gradual change in leak flow rate over the range 0-760 L/min (0-200 gpm) with at most a <1% rise above the desired set point at pressure set point levels ranging from 0 to 19 MPa (0 to 2800 psi) for room- and elevated-temperature operation.

4.3.3 Initial Tube Leak and Rupture Testing

In the second half of this reporting period, the facility conducted an initial series of tests on flawed tubes. All tested tubes were fabricated from 22.2-mm (7/8-in.)-diameter Alloy 600 SG tubing (Valinco heat NX8524). Tests have been conducted on tubes with axial OD EDM notches of several lengths and depths. Tests have also been conducted on tubes with circular orifice EDM holes of various diameters to study the influence of flaw area and shape on leak modeling. The results of these tests were also used to evaluate the range of validity of a sharp-edged orifice flow model for predicting flow from circular and highly noncircular flaws (e.g., highly open and tight flaws), as well as to check other leak models currently in use. The EDM flawed tubes were all 0.56-m (22-in.) long with the flaw centered at 0.15 m (6 in.) from the end of the tube fitted with a welded plug. The unplugged end of the tube was held in place in the test module vessel by a Swagelok fitting mounted on a blind flange with a hole that permits flow from the blowdown vessel to enter the flawed tube. Finally, experiments were also performed on several laboratory-degraded tubes containing axial ODSCC. These tests addressed questions concerning flaw leak stability under constant temperature and pressure associated with normal and main steam line break operating conditions. The various flaw types were tested at both room and elevated temperature to assess flaw behavior dependence on temperature. In early EDM flaw testing, two identical specimens of each flaw type were tested to verify reproducibility of specimens and leak rate/pressure data and to evaluate the influence of test temperature on the leak rate of identical flaws. Plans are also in place to test EDM and laser-cut axial and circumferential flaws with multiple interacting notches separated by ligaments of various lengths.

All flaws tested in the facility were characterized with respect to flaw dimensions before and after testing. In general, the EDM flaws tested (comprising circular orifices and EDM notches) are relatively easy to characterize, but the characterization of the SCC flaws is much more difficult. Because of the need to evaluate leak rate and flaw opening pressure prediction capabilities and improve the models if needed, accurate knowledge of pre- and posttest flaw dimensions and leak area is essential. Procedures have been developed and implemented to obtain these data.

Each tube specimen is given an engraved alphanumeric identifier that enables it to be tracked through all phases of fabrication and testing. A detailed tube specimen facility testing table has been developed for keeping track of the tube type, material type, source, pretest flaw characterization work, test conditions, facility mode of operation, computer data records, posttest tube characterization, leak/rupture data analysis results, and any comments on testing pertinent to interpretation of data. Over the next two years, as many as 150-200 tubes will undergo testing.

The following pretest flaw characterization steps are used:

1. Eddy current NDE, yielding crack depth profiles and voltage and other information.

2. Utilization of finite element code structural calculations to estimate crack opening pressures from NDE crack depth profiles.

3. Dye penetrant techniques and digital photography with computerized image analysis to characterize the flaw region

4. Low-pressure (0.28 MPa or 40 psi) air-bubble tests in a water bath to identify regions of throughwall penetration

5. In some cases, destructive examination of part-throughwall flaws after testing to validate NDE depth measurements and to assess tube structural wall tear characteristics.

For SCC flaws, the use of dye penetrant for crack accentuation and digital photography is an essential part of the pre- and posttest flaw characterization process to permit flaw characteristics to be related to leak behavior. After the flaw has been accentuated through the use of dye penetrant, digital photography and image processing techniques are used to obtain flaw information such as crack area, total length, and location and number of branch points. The use of computerized digital image analysis of flaw images provides a more systematic and less subjective means of characterizing flaw features than using an optical microscope or measuring manually from photographs.

An additional procedure has been developed for characterizing the surface crack pattern for throughwall flaws. With the dye penetrant still in the crack, the capped tube is connected to a low-pressure (0.28 MPa or 40 psi) air pressurization apparatus and submerged in a water bath. The flaw region is observed with a low-magnification optical microscope for gas bubble leaks along the crack, and the leakage regions are recorded. All of the above procedures for crack and leak characterization are performed before and after testing to obtain information on changes in crack morphology resulting from the test.

The tests conducted to date have provided information on facility operation and performance; the influence of crack geometry, temperature, and pressure on flaw behavior; and the effectiveness of pre- and posttest flaw characterization procedures. Detailed results from these tests are summarized in the following three sections.

4.3.3.1   Initial Circular Hole Flaw Testing

An initial series of tests was conducted on tubes with sharp-edged circular orifice throughwall holes using room- and high-temperature water. These tubes had hole diameters of 6.35 mm (1/4 in.) (specimen T5EOTWX.250D), 3.175-mm (1/8 in.) (specimen T4EOTWX.125D), and 0.794 mm (1/32 in.) (specimen T6EOTWX.031D).

Each hole diameter was carefully measured and checked for circularity and sharpness of the entrance and exit edges. Depending on the entrance contours and the importance of roughness, the orifice coefficient can range from near unity to as low as 0.5. Photographs of the EDM holes show quite sharp hole edges, indicating a coefficient in the lower end of this range. The EDM process was also found to leave a pebbly, rough pattern on the hole walls, and the walls have been optically photographed to record this roughness. Following testing, the specimens were checked for evidence of flow erosion on the hole walls by comparing their appearances with those in the pretest photographs. Such erosion can increase the flow area beyond that produced by corrosion alone. This comparison was done for both room- and elevated-temperature tests, and no erosion was detected in these short-duration tests. The tests at different temperatures also permit an evaluation of leak correlations as a function of temperature and different multiphase flow conditions for this simple hole geometry. For very small circular holes, it is possible that the wall roughness will be significant compared to the hole diameter and will affect flow behavior, thereby influencing the orifice leak correlation. This situation may be analogous to what happens in a real throughwall SCC flaw that is tight enough so that the crack wall roughness is significant relative to the crack width.

During the tests, the pressure gradient across the tube wall was varied from 0 to 19 MPa (0 to 2800 psi) in several plateau steps for a 760 L (200 gal) water charge of the blowdown vessel. All data were recorded on the facility DAS. Sufficient time was available at each plateau to permit the pressure and flow rate to stabilize before increasing the pressure to the next level. No hole structural distortion or erosion was detected under these conditions in posttest examination, and test control and data reproducibility were good.

Figures 4.14 and 4.15 show typical computer-DAS-recorded tube-pressure differential and blowdown vessel weight, respectively, as a function of time for the 0.794-mm (1/32-in.)-diameter hole size test. As shown in Fig. 4.14, the tube was subjected to seven increasing pressure plateaus ranging from 0.69-19.5 MPa (100-2825 psi). The pressure is quite constant at each plateau. At the low flows associated with this test (<4 L/min [1 gpm] at the highest pressure), leak flow rate was determined solely by the measured change in blowdown vessel weight. Figure 4.15 shows a plot of vessel weight vs. time. For each pressure plateau of Fig. 4.14, the weight curve exhibits a straight-line segment. The slope of this segment, after applying a correction for increasing weight of the cover gas in the tank, is the water leak rate in kg/s.

The leak rates for the 0.794-, 3.175-, and 6.35-mm (1/32-, 1/8- and 1/4-in.)-diameter holes for room temperature water at the nominal differential pressure of 17.2 MPa (2500 psi) were 2.76, 56.0, and 216 L/min (0.73, 14.8, and 57.0 gpm), respectively. The 3.175-mm
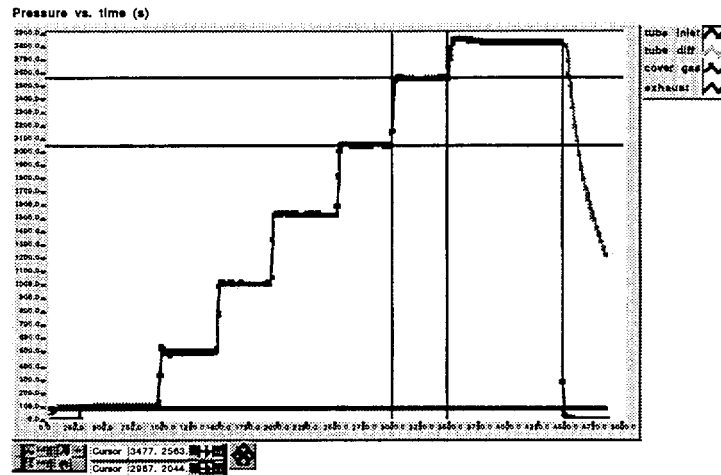
Fig. 4.14. Tube pressure difference vs. time for test of tube with 0.794-mm (1/32-in.)-diameter hole (T6EOTWX.031D).
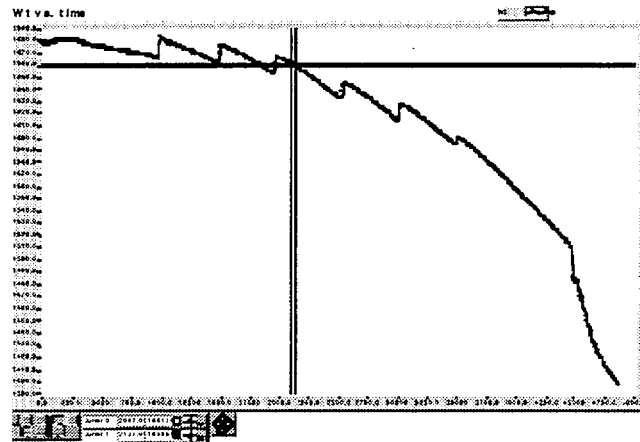
Fig. 4.15. Blowdown vessel weight vs. time during test of tube with 0.794-mm (1/32-in.)-diameter hole (T6EOTWX.031D).

(1/8-in.)-diameter hole at 17.2 MPa (2500 psi) exhibited an average jet velocity of 112 m/s (366 ft/s). These high jet velocities can produce significant lateral thrust, and the 6.35-mm (1/4-in.)-diameter hole specimen was bent ≈10° from its axis as a result of this thrust (Fig. 4.16). The two other specimens with smaller diameter holes leaked at lower flow rates at this same pressure and hence were subjected to lower jet thrust, resulting in no observable bending.

The flow rate through the 3.175-mm (1/8-in.)-diameter hole in a test using 282°C (540°F) water was compared with that observed at room temperature. A standard correlation for a sharp-edged circular orifice,

$$Q = C \cdot A \cdot \left(\frac{\Delta p}{\rho}\right)^{1/2}, \qquad (4.1)$$
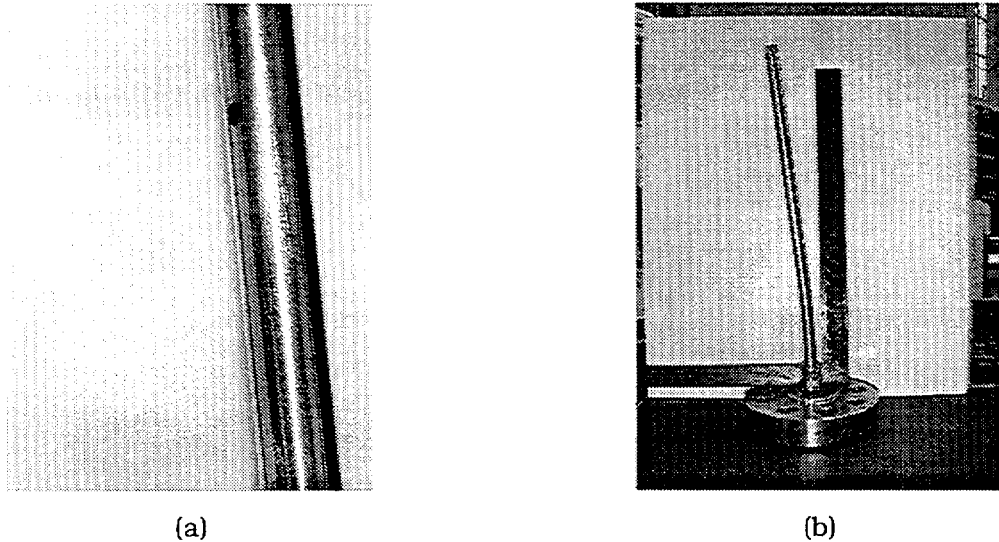
Fig. 4.16.   Two views of tube T5EOTWX.250D containing 6.35-mm (1/4-in.)-diameter
circular hole after testing, showing bending produced by thrust from water jet.

was used, where Q is the flow rate, C is the orifice discharge coefficient, A is the cross-sectional area, Δp is the pressure gradient across the orifice, and ρ is the density of the fluid. For C = 0.6, this correlation was found to predict the room-temperature flow rate quite well. When applied to the elevated-temperature data, this relatively simple model also appeared to correctly describe the fluid temperature effect on flow rate through the dependence of fluid density on temperature.   The density of water at 21 and 282°C (70 and 540°F) is 1.00 and 0.745 g/cm^3 (62.3 and 46.51 lb./ft^3), respectively. In two separate tests, the same tube tested at a pressure differential of 8.72 MPa (1265 psi) and a temperature of 282°C (540°F), exhibited a flow rate of 3.03 L/min. (11.45 gpm). For C = 0.6, Eq. 4.1 predicts a flow rate of 3.04 L/min. (11.51 gpm), in very good agreement with the experimental value.   The orifice correlation predicts a flow rate of 2.63 L/min. (9.95 gpm) for this same 3.175-mm (1/8-in.)-diameter hole under the same pressure differential for room-temperature water.   Thus, for the limited conditions explored, elevating the water temperature for the same orifice pressure differential increases the volumetric leak flow rate.   Additional elevated-temperature data are being generated for EDM holes, and the validity of Eq. 4.1 will be explored over a wider range of conditions.   In particular, the possibility that the effect of hole roughness on leak rate may become significant for very small circular holes will be examined.   Other predictive leak rate codes such as SQUIRT will also be evaluated.

4.3.3.2   Initial Rectangular Notch Flaw Testing

Rectangular notches with high aspect ratios (flaw length/width), which more closely approximate service- or laboratory-induced SCC, have not been studied nearly as thoroughly as circular orifices. Furthermore, a very-high-aspect-ratio notch having the same flow area as a circular hole may exhibit a significantly different flow rate if the notch width is about the same as the material grain size. This difference is caused by the dramatically different flow behavior in the narrow flow passage resulting from surface roughness and tortuosity effects. The criteria for defining when a flaw is tight are not well understood or demonstrated because of lack of an adequate data base.   Furthermore, the hole leak rate can be significantly impacted by whether the flaws are sharp-edged (i.e., the flow turns abruptly at a 90° angle to

enter the flaw) or the inlet edge of the flaw is more smoothly contoured. For example, a sharp-inlet-edge circular orifice can be represented by a discharge coefficient of value 0.6, whereas an orifice of the same flow area but having a smooth inlet can have a coefficient approaching unity. Hence, a simple measurement of flow area can be grossly inadequate. These issues are being addressed in this program.

A series of tests on tubes with 38.1- and 12.7-mm (1.5- and 0.5-in.)-long axial EDM notches has also been performed. These flaws are simplified representations of SCC flaws and thus permit a systematic parametric study of the influence of flaw size, shape, placement, multiple flaw interactions, and tube properties on leak rate and flaw opening tendencies. Three tubes (T3EA80X1.5, T4EA80X1.5, and T7EA80X1.5) with geometrically identical axial OD 38.1-mm (1.5 in.)-long, 0.20-mm (0.0075-in.)-wide 80% TW EDM flaws were tested at room temperature. Two of these tubes had the same as-received heat treatment and provided a check on data reproducibility, and the remaining tube was sensitized (solution heat treated at 1100°C for 10 min and aged at 600°C for 48 h) before testing to evaluate the influence of this heat treatment on flaw failure behavior. A tube containing a throughwall axial EDM notch 12.7-mm (1/2-in.) long and 0.20-mm (0.0075-in.) wide was also tested at room temperature.

All three tubes opened dramatically upon failure and had high volumetric flow rates. The behavior of the three tubes was quite similar, and test details are therefore presented only for tube T4EA80X1.5. For this tube, the pressure gradient across the tube wall was increased in a series of pressure steps starting at 0.69 MPa (100 psi) in increments of 1.38 MPa (200 psi) up to 10.3 MPa (1500 psi), then in increments of 0.69 MPa (100 psi) up to 13.8 MPa (2000 psi), and finally in increments of 0.34 MPa (50 psi) until tube failure. The tube failed at ≈17.22 MPa (2497 psi), and the flow through the flaw abruptly increased from 0 to a sustained leak rate of ≈1470 L/min (388 gpm) in less than 1 s. This leak rate was successfully measured before the facility automatically shut down because of low water inventory in the blowdown vessel. The leak event lasted a total of about 28 s. The facility was originally designed to sustain a leak rate of at least 760 L/min (200 gpm), and this target was exceeded in this test. Finite-element code calculations predicted a failure pressure of 17.24 MPa (2500 psi) for this flaw. Upon removal from the test module, the tube was found to have been bent by the jet thrust, and the crack had opened up to a large hole. Figure 4.17 shows a photograph of the flaw opening after testing, and Figure 4.18 shows a side view of the flaw.

Table 4.1 summarizes the failure pressure data and flow rates for tests T3EA80X1.5, T4EA80X1.5, and T7EA80X1.5 and reports results on posttest rupture hole area obtained by computer analysis of digital images of the flaws. The reported hole areas are the values obtained by projecting the puckered three-dimensional hole area onto the mean plane of the failure location. The maximum width of the hole is taken at the widest part of the puckered hole opening. The failure-pressure and leak-rate data for the two tubes with the same heat treatment (T4EA80X1.5 and T7EA80X1.5) are in close agreement. Tube T4EA80X1.5 failed at 17.2 MPa (2497 psi) with a sustained leak rate of ≈1469 L/min (388 gpm), and tube T7EA80X1.5 failed at a pressure of 16.5 MPa (2398 psi) with a leak rate of ≈1453 L/min (384 gpm). These tubes also exhibited very similar failure opening areas and overall lengths and maximum widths. The sensitized tube (T3EA80X1.5) exhibited a reduced failure pressure, an increased flow area, and a larger hole width. It failed at 13.8 MPa (2000 psi) and exhibited a leak rate of 1605 L/min (424 gpm). The hole size for this tube after failure was larger than those for the two unsensitized tubes. The heat treatment used to promote SCC clearly
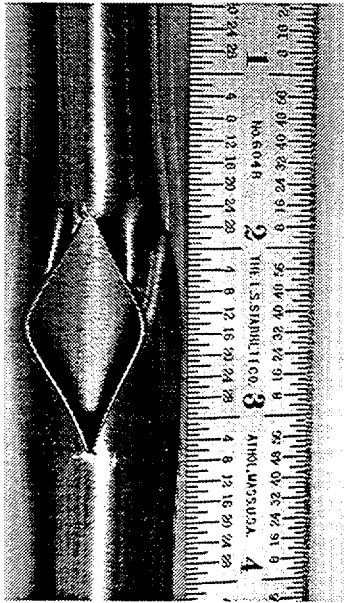
Fig. 4.17. Photograph of specimen containing 38.1-mm (1.5-in.)-long 80% TW axial EDM notch after failure (test T4EA80X1.5).
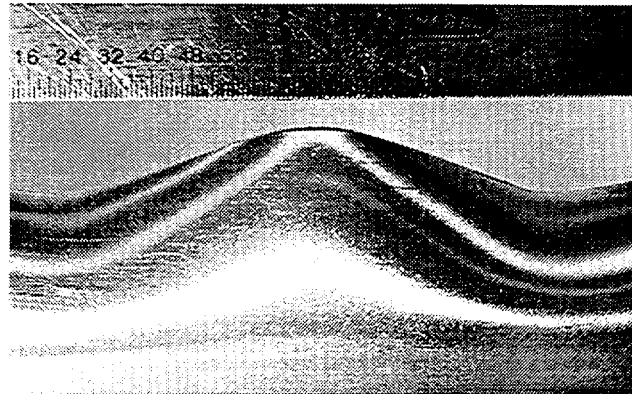
Fig. 4.18. Side view of tube shown in Fig. 4.17.

Table 4.1. Results from pressure and leak-rate tests on tubes with 38.1-mm (1.5-in.)-long 80% TW axial EDM flaws. Tube T3EA80X1.5 was subjected to a sensitization heat treatment before testing, and the remaining two tubes were tested in as-received mill-annealed condition.

Tube ID	Failure Pressure (MPa [psi])	Flow Rate (L/min [gpm])	Hole Area (cm^2 [in.^{2}])	Hole Overall Length (cm/ [in.])	Hole Maximum Width (cm/ [in.])
T3EA80X1.5	13.8 (2000)	1605 (424)	8.31 (0.507)	3.30 (1.30)	1.83 (0.72)
T4EA80X1.5	17.2 (2497)	1469 (388)	7.41 (0.452)	3.35 (1.32)	1.60 (0.63)
T7EA80X1.5	16.5 (2398)	1453 (384)	7.24 (0.442)	3.38 (1.33)	1.57 (0.62)

weakens tubes and changes the leak and rupture characteristics somewhat. For very tight SCC cracks, the leak rate and fundamental leak regimes may be influenced by the increased grain size associated with the heat treatment. This behavior is being evaluated further.

All three tubes exhibit the same approximate overall hole length of ≈33.5 mm (1.32 in.). It should be noted that all three tubes underwent significant lateral bending as a result of jet thrust, similar to that reported for the 6.35-mm (1/4-in.)-diameter circular hole tube, and this bending probably influenced the flow area somewhat. Work is currently underway to see how well these leak rates, rupture pressures, and hole areas can be predicted from structural analysis codes and from various flow models and codes such as SQUIRT. There are some early indications that the simple orifice leak model discussed above can be used to predict the flow rates at failure reasonably well.

The room-temperature test of tube T2EATWX.5 containing a 12.7-mm (0.5-in.)-long throughwall flaw is described next. The pressure gradient across the tube wall was increased in a series of steps consisting of seven pressure plateaus. The tube leaked water at all pressures. The highest pressure achieved was 19.28 MPa (2796 psi), at which point a steady-state leak rate of 29.1 L/min (7.7 gpm) was observed. Figure 4.19 is a photograph of the flaw opening after testing. The width of the flaw has increased substantially from the initial uniform 0.19 mm (0.0075 in.) width formed by EDM, and there is a slight amount of metal tearing (not visible at this magnification) at both ends of the notch. The flow rate predicted for this notch at the highest pressure, based on the posttest measured area and Eq. 4.1 with C = 0.6. was in good agreement with the experimental value.

Additional single axial notches of length 25.4, 12.7, and 8.9 mm (1.0, 0.5, and 0.35 in.) and various depths will also be tested at room and elevated temperatures. Testing of tubes with circumferential and various patterns of multiple interacting flaws are also planned. Tubes with field- and laboratory-induced SCC cracks frequently exhibit these complex flaw patterns, and EDM and laser-cut notches will be tested to explore leak and failure behaviors. The influence of the sensitization heat treatment on tube material properties and flaw behavior is also being studied further. The use of the circular orifice flow correlation may overpredict the flow rate when the flaws are tight, and this effect will be explored to determine the threshold below which the correlation fails.

4.3.3.3 Initial SCC Flaw Testing

Test results from four Alloy 600 tubes with laboratory-produced axial ODSCC of nominal length 12.7 mm (0.5-in.) are described here. The tubes, SGL-177, SGL-195, SGL-104, and SGL-219, were cracked at ANL in an aqueous solution of sodium tetrathionate, as described in Section 4.3.1. The tests were designed to gain information on flaw stability under constant temperature and pressure conditions associated with normal SG operation and main steam line break, i.e., T = 282°C (540°F) and p = 8.3 and 17.2 MPa (1200 and 2500 psi), respectively. These pressure plateaus were held for at least 2 h (depending on leak rate and amount of water in the blowdown vessel), with extended duration holds at intermediate pressures if flaw flaw tearing, as indicated by a sudden increase in flow, was observed. Tubes SGL-177 and SGL-195 were tested at room temperature and tubes SGL-104 and SGL-219 were tested at 282°C.

As described earlier, three techniques were used to characterize the SCC flaws prior to testing: (a) dye penetrant crack accentuation and digital photography with computerized image
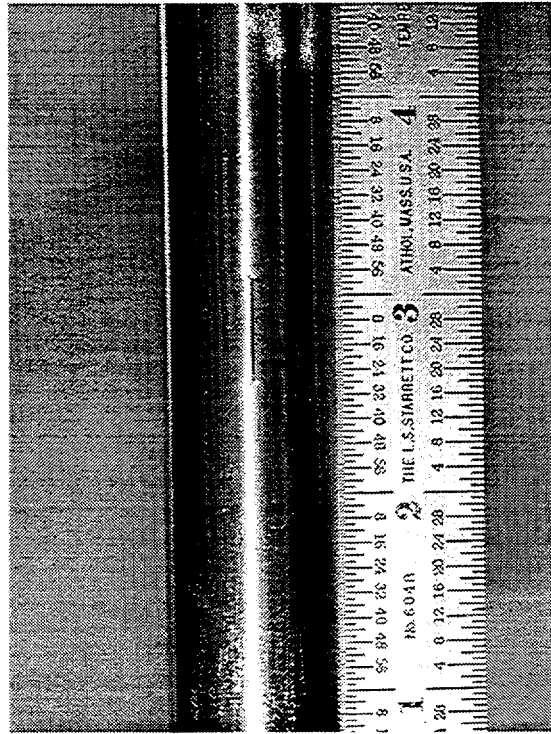
Fig. 4.19. *Posttest photograph of slightly opened 12.7-mm (0.5-in.)-long TW EDM notch (tube T2EATWX.5).*

analysis, (b) bubble testing with low-pressure (0.28 MPa [40 psi]) air in a water bath to identify regions of throughwall penetration, and (c) EC NDE. Finite-element code structural calculations were used to estimate crack opening pressures from the NDE crack depth profiles.

Based on the EC results, all four flaws had variable crack depths along their main flaw zones, with maximum depths of 75-95%. Leaking throughwall cracks not seen by EC NDE were identified in all four specimens by the pretest bubble examination, and the dye penetrant inspection revealed flaw branching. The EC BC voltages indicated that the four flaws fell into two categories. Tube SGL-177 had a voltage of 4.0 V, and the other three tubes had highr levels of 6-10 V. The crack depth profiles for the four tubes were used not only to prescreen the flaws for similarity but also to calculate the pressure at which the flaws would start to open. The tests are described below.

Room-Temperature Tests

Results are presented first for tubes SGL-177 and SGL-195, which were tested at room temperature. The two flaws are quite similar in their overall characteristics. The flaw in sample SGL-177 (test T501ACTW177-B), shown in Fig. 4.20, is nominally 12.2-mm (0.48-in.) long and exhibits "Y" branching at both ends. Similarly, the flaw in sample SGL-195 (test T500ACTW195-B), shown in Fig. 4.21, is nominally 13.7-mm (0.54-in.) long and also exhibits "Y" branching at both ends. Both cracks thus have similar overall lengths and end-branching patterns. The bubble leak test results also revealed similar leakage locations for both flaws; a main leak region located near the center of each crack pattern and a secondary leak region located at a "Y" branch point. It thus appears that both cracks have a nonthroughwall ligament between the two regions of throughwall penetration. Time–dependent failure of this

ligament (or a portion thereof) could produce changes in leak rate under conditions of constant temperature and pressure .

Tube SGL-195. This tube was tested by gradually increasing the internal pressure in ≈2.1-MPa (300-psi) increments. Each pressure plateau was held for about 15-30 min except for that at 8.27 MPa (1200 psi) (nominally, normal plant operating conditions), which was held for 2 h. Even though the crack showed definite gas leakage at two locations during the pretest gas bubble check (indicating localized throughwall penetration) no leakage was detected in water testing during the 2-h hold at 8.27 MPa (1200 psi). As stated previously, the facility can detect leak rates of several hundredths of a L/min. With increasing pressure beyond 8.27 MPa (1200 psi) the tube continued to show no detectable leakage until the pressure reached the ≈14.7 MPa (2129 psi) pressure plateau, where very slight leakage was observed. As the pressure was increased toward the final target plateau of 17.2 MPa (2500 psi), the tube abruptly started leaking at 29.9 L/min (7.9 gpm) when the pressure reached ≈15.1 MPa (2188 psi). When the pressure stabilized at 15.5 MPa (2250 psi), the leak rate had increased to 32.6 L/min (8.6 gpm) and remained at that level for another 15 min. The test was terminated at this point because of low blowdown vessel water inventory.

The tube was removed from the test module and digitally photographed (see Fig. 4.22) for image analysis. The tube also underwent posttest EC examination and will eventually be examined destructively. A visual comparison of the posttest photograph (Fig. 4.22) with the pretest photograph of the dye penetrant crack image (Fig. 4.21) shows that the flaw had opened up significantly in width along its entire length, even into the extremities of the Y branches at each end of the main flaw. Additional zones of what appeared to be faint dye streaks in Fig. 4.21 are seen in Fig. 4.22 to correspond to several posttest cracks emanating from the main crack pattern. The region around the flaw is raised noticeably, i.e., puckered.

Tube SGL-177. This tube was tested using the same general procedure as for tube SGL-195, except that the pressure plateaus associated with normal operating and main steam line break (MSLB) conditions were both held for >15 h by running the test facility at fixed pressure overnight under automatic control. As for tube SGL-195, no leak was detected on the approach to normal operating tube pressure differential or during the >15 h overnight hold at normal operating pressure (8.27 MPa or 1200 psi). Thus, both SCC flawed tubes, even though exhibiting throughwall localized penetration in the low-pressure gas bubble test at locations marked in Figs. 4.20 and 4.21, did not leak under normal operating pressure in subsequent water tests.

Following the overnight hold at 8.27 MPa (1200 psi), tube pressure was increased in 1.38-MPa (200-psi) increments toward MSLB conditions. No leakage was detected until the pressure reached 16.9 MPa (2450 psi). For the first 100 min at this pressure, no leak was detected. However, a very small leak of less than several hundredths of a L/min then abruptly appeared at this same pressure. Leak initiation was verified by an ultrasonic leak detector that sensed the water jet noise when held on the walls of the test module. After ≈1 h of steady leak rate under constant pressure, the rate abruptly increased further to ≈0.26 L/min (0.07 gpm). This increase was accompanied by a stronger signal output from the ultrasonic leak detector. The crack was allowed to leak at this fixed pressure level overnight, but no additional increase in flow rate was observed.

After replenishing the blowdown vessel water inventory and recharging the nitrogen cover gas pressurization system, the pressure on the tube was increased to higher levels to see if the
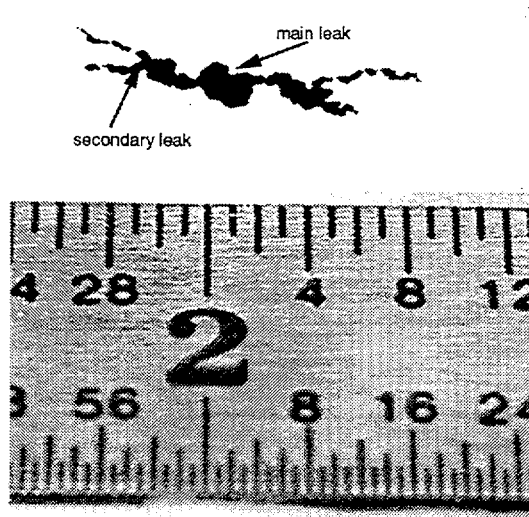
Fig. 4.20. *Pretest image of tube SGL-177 with flaw highlighted by dye penetrant and digital image processing; two regions of throughwall penetration are indicated by bubble testing.*
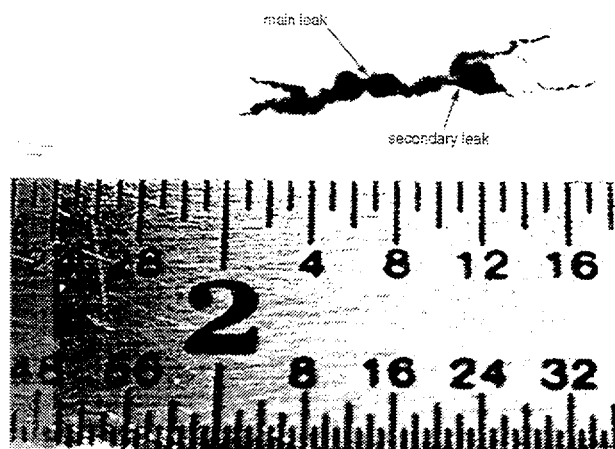
Fig. 4.21. *Pretest image of tube SGL-195 with flaw highlighted by dye penetrant and digital image processing; two regions of throughwall penetration are indicated by bubble testing.*
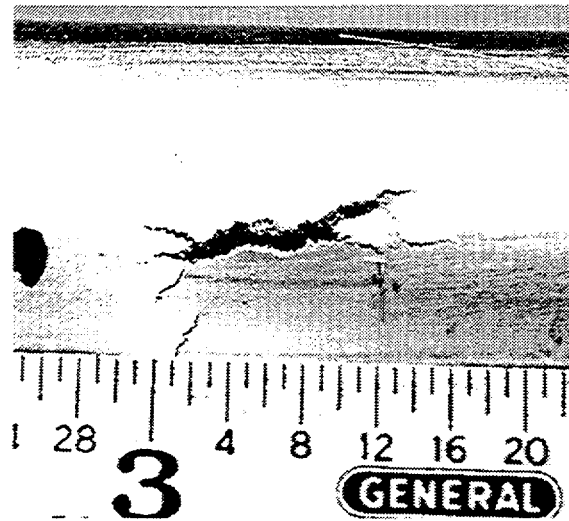
Fig. 4.22. Digital photograph of failed region of tube SGL-195 after testing.

tube would open further. The pressure was increased to a maximum of 19.3 MPa (2800 psi) in a series of plateaus held for 30 min or less, and the leak rate continuously increased with increasing pressure. At each increased leak level, increasing leak noise was also measured, though the audible noise would occasionally change frequency and fluctuate randomly. At 19.3 MPa (2800 psi), the leak rate was 1.67 L/min (0.44 gpm). This was considerably less than the 32.6 L/min (8.6 gpm) leak at 15.5 MPa (2250 psi) that abruptly occurred for tube SGL-195 under similar conditions. The crack depth profile determined by pretest EC inspection for tube SGL-177 was not as uniformly deep over its length as the profile for tube SGL-195. Similarly, the posttest digital image of the opened flaw in tube SGL-177 shown in Fig. 4.23 shows less opening than that for tube SGL-195 (Fig. 4.22).

Elevated-Temperature Tests

Tubes SGL-104 and SGL-219 were tested at 282°C (540°F) using procedures similar to those for the room-temperature tests. The flaws in these tubes have overall axial extents of 10.4 and 14.0 mm (0.41 and 0.55-in.), respectively, as determined by dye-penetrant examinations. These flaws are thus nominally the same size as the flaws present in tubes SGL-177 and SGL-195 tested at room temperature. Like tubes SGL-177 and SGL-195, the flaws in tubes SGL-104 and SGL-219 exhibited Y-branch cracking at both ends of a central axial crack zone (Figs. 4.24 and 4.25). These flaws also had a central region of throughwall penetration as determined by pretest bubble testing. Unlike tubes SGL-177 and SGL-195, however, tubes SGL-104 and SGL-219 did not have a second smaller leak zone at a branch point. Based on EC examination results, the flaws in all four tubes had variable crack depths along their main flaw zones, with maximum depths of 75-95%. The pretest leak zones were not detected by EC because of their very small axial extent and tightness. The EC crack depth profiles were used not only to prescreen the flaws for similarity but also in finite-element calculations to estimate the failure pressures of the flaws. In most cases, these predictions, based on the thinnest crack zone, were found to be in good agreement with the observed failure pressures.
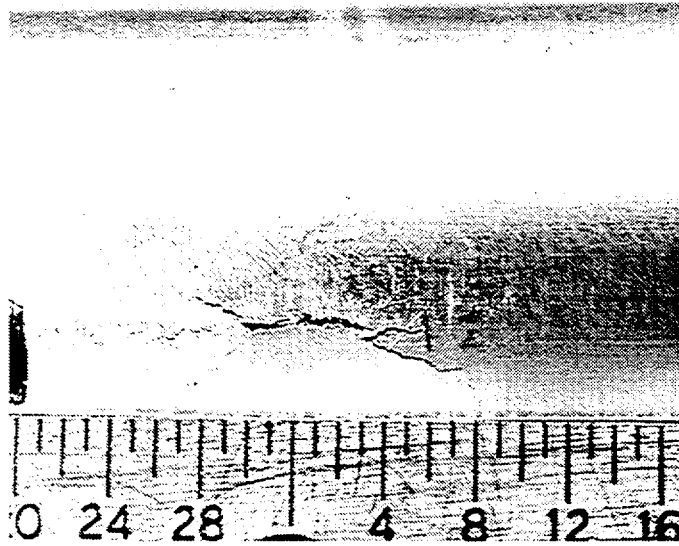
Fig. 4.23.   Digital photograph of failed region of tube SGL-177 after testing.
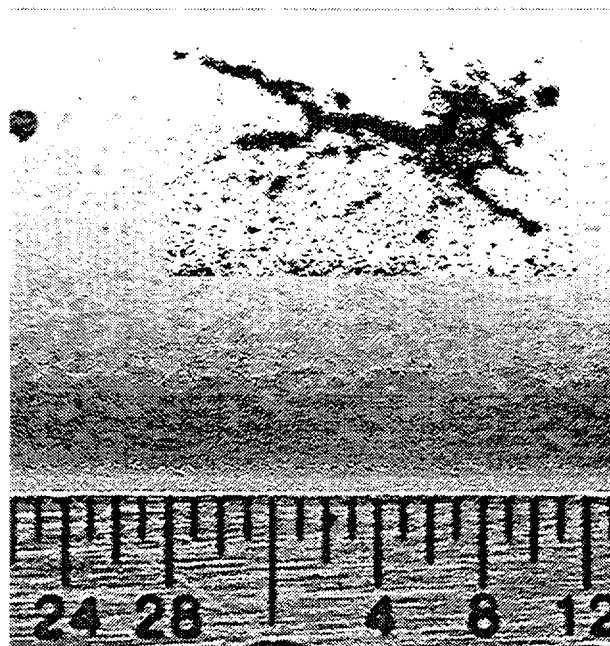
Fig. 4.24.   Pretest image of tube SGL-104 with flaw highlighted by dye penetrant and digital image processing; a single region of throughwall penetration was indicated by bubble testing.
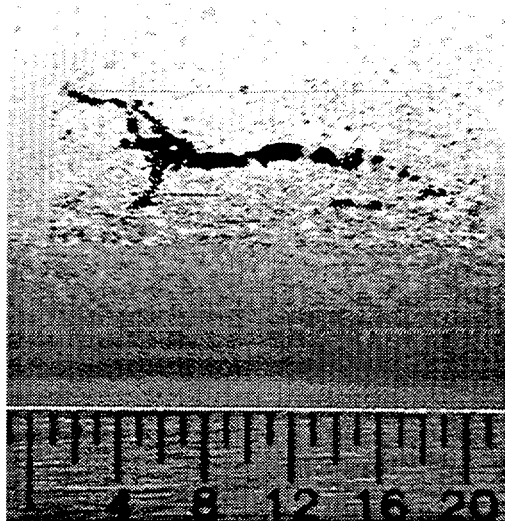
Fig. 4.25. *Pretest image of tube SGL-219 with flaw highlighted by dye penetrant and digital image processing; a single region of throughwall penetration was indicated by bubble testing.*

Tube SGL-104. This tube again exhibited no detectable leakage at pressures below 8.27 MPa (1200 psi) or during the 2-h hold at that pressure, despite the throughwall penetration indicated by the bubble test. In fact, no detectable leakage occurred until the pressure exceeded 15.9 MPa (2300 psi). During the subsequent pressure ramp to 17.2 MPa (2500 psi), the flaw abruptly opened at 16.2 MPa (2352 psi) and yielded a flow of 21.2 L/min (5.6 gpm). When the pressure stabilized at the final 17.2 MPa (2500 psi) hold plateau, the flow rate held steady at 23.5 L/min (6.2 gpm). The increases in flow rate were all associated with increases in internal pressure for this tube, and no flaw tearing under constant conditions was indicated. The test was terminated after an additional 15 min because of low blowdown vessel water inventory.

A comparison of posttest (Fig. 4.26) and pretest (Fig. 4.24) photographs of the flawed region of tube SGL-104 shows that the flaw opened significantly in width in all regions highlighted by the pretest dye-penetrant examination, similar to that of tube SGL-195. Like tube SGL-195, several posttest secondary cracks also emanate from the main crack pattern in tube SGL-104 after testing, again corresponding to faint pretest dye-penetrant images. The region around the flaw is again raised noticeably, or puckered, as seen in the side view of Fig. 4.27. This suggests that the corrosion may have produced a weak region, with the small secondary cracks probably contributing to the overall weakness.

Tube SGL-219. As for the other SCC flaws tested, this tube exhibited no detectable leakage at pressures below 8.3 MPa (1200 psi) or during a 2-h hold at 8.3 MPa (1200 psi), although it had leaked air in the pretest bubble test. In fact, no leakage was detected until the pressure reached 13.3 MPa (1930 psi), when the flaw abruptly opened and leaked at 3.7 L/min. (0.97 gpm). This pressure was held for 90 min, during which time no change in flow rate was observed. The test was stopped because of low water inventory and was restarted after refilling and reheating the system. The test was resumed at 13.3 MPa (1930 psi), which resulted in the same leak rate as before, and pressure ramping continued. After 10 min at 16.2 MPa (2346 psi), the leak rate increased abruptly to 14.0 L/min. (3.7 gpm), indicating

ligament tearing. During the subsequent 11 min at this pressure, the leak rate gradually increased to 39.0 L/min (10.3 gpm), suggesting additional ligament tearing under constant conditions. For the next 9 min, the flow remained stable at 39.0 L/min. The test was then terminated because of low water inventory.

Posttest digital photography inspection of the tube SGL-219 (Figs. 4.28 and 4.29) and comparison with the pretest digital photograph of the flaw (Fig. 4.25) shows that the flaw opened significantly in width along its entire length, even into the extremities of the Y branches on the ends of the main flaw. Again, several posttest secondary cracks emanate from the main crack; these cracks are marginally observable in the pretest flaw image. The region around the flaw is raised noticeably, or puckered.

Observations from all four SCC tests are presented in Table 4.2 and can be summarized as follows:

1. All four SCC flaws were axial, very tight, nominally 13-mm (0.5 in.)-long, and had one or two subregions of pretest throughwall penetration (pinholes) as determined by bubble testing. However, none of the flaws exhibited detectable water leakage at pressures below 8.3 MPa or during the 2-h (or greater) hold times at 8.3 MPa (1200 psi). In fact, no detectable leakage occurred until substantially higher pressures were reached.

2. Flaws in three of the four tubes (SGL-195, SGL-177, and SGL-219) exhibited crack ligament tearing under constant temperature and pressure conditions, resulting in increasing leak rates under constant pressure.

3. Posttest inspection revealed that flaws in three of the four tubes (SGL-195, SGL-104, and SGL-219) opened significantly in width along their entire length, even into the extremities of the Y branches at each end of the main flaw. The other tube (SGL-177), for which the
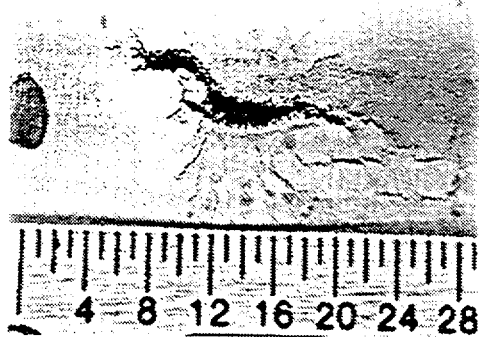
Fig. 4.28. Photograph of failed region of tube SGL-219 after testing.
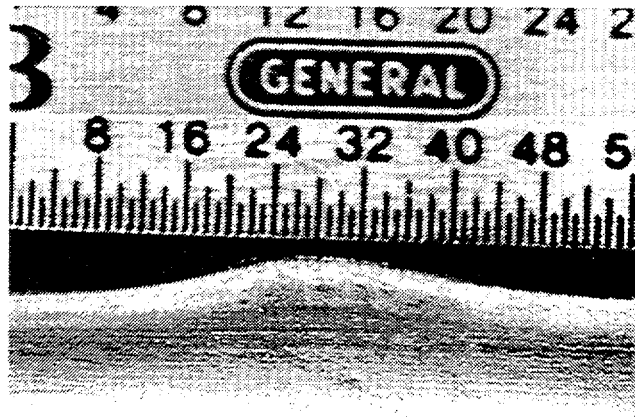
Fig. 4.29. Side view of tube shown in Fig. 4.28.

Table 4.2. Summary of results from four tests on tubes with axial ODSCC cracks.

Test Number	Overall flaw length (mm)	Test Temp (°C)	Pretest air leak at 0.28 MPa	Flaw opening pressure initial/final (MPa)	Tearing pressure, constant conditions (MPa)	Flow rate at initial/final opening pressure (L/min)
SGL-177	12.2	R.T.	yes	16.9/19.3	16.9	0.04-0.26/ 1.67
SGL-195	13.7	R.T.	yes	14.7/15.5	14.7	<0.04/32.6
SGL-104	10.4	282	yes	16.2/17.2	no tearing	21.2/23.5
SGL-219	14.0	282	yes	13.3/16.2	16.2	3.7/ 14.0-39.0

EC amplitude of ≈4 V was considerably lower, opened only slightly. Additionally, tubes SGL-195, SGL-104, and SGL-219 had several posttest secondary cracks emanating from the main crack pattern, and the region around the flaws was raised noticeably (puckered). The flaw with the lower EC voltage did not exhibit this behavior.

4. Three of the four tubes, SGL-195, SGL-104, and SGL-219, which opened along their entire pretest flaw extent, did so at pressures of <17.2 MPa (2500 psi), resulting in flow rates of 23-38 L/min (6.0-10.0 gpm) or more. These three tubes had the highest EC voltages. Tube SGL-177, which had the lowest EC voltage, exhibited a leak rate of 1.66 L/min (0.44 gpm).

The results described here suggest that ligament failure in an SCC flaw may occur progressively (sometimes with delays under constant loading conditions) until the crack is completely open over its full extent. In flawed specimens with highly varying ligament thicknesses, initial leakage occurred abruptly at a pressure significantly lower than that predicted by the equivalent rectangular crack approach. The experimental evidence of time-dependent increase of leak rate possibly due to progressive ligament rupture at 282°C (550°F), as well as at room temperature, highlights the lack of a criterion for predicting time-dependent ligament rupture. Many more SCC flaws will be tested, and eventually field-induced SCC flaws will be tested as the ultimate check on our understanding of tube flaw behavior.

4.4   Pretest Analysis of Crack Behavior

4.4.1   Analysis of Two Collinear Axial Cracks with a Ligament

To help design tests for the leak rate test facility, a series of finite-element analyses were conducted on a 22.2-mm (0.875-in.)-diameter Alloy 600 tube with a single throughwall axial crack or two collinear throughwall axial cracks with a ligament between (Fig. 4.30a). The analysis was done for a sharp crack, ignoring the initial flaw width. The total crack opening area was determined by adding the initial flaw area to the computed crack opening area. The stress strain curve assumed for analysis is shown in Fig. 4.30b.

4.4.1.1   Single Crack Results

The variations of total crack opening displacement over the crack surface for single throughwall cracks of length 12.7 mm (0.5 in.) and 25.4 mm (1.0 in.) are shown in Figs. 4.31 a-b, respectively. Estimated failure pressures for these two cracks are 16.5 and 29.0 MPa (2.4 and 4.2 ksi), respectively. It is proposed that a test using a specimen with a 25.4-mm (1-in.)-long TW flaw be pressurized and periodically unloaded to measure the flaw opening as a function of pressure to validate these calculations.

4.4.1.2   Multiple Crack Results

The variations of effective stresses at the ID and OD surfaces of the ligament for two collinear throughwall cracks of length 12.7 mm (0.5 in.) separated by ligaments of width 1.27, 2.54, and 6.35 mm (0.05 in., 0.10 in., and 0.25 in.) are shown in Figs. 4.32 a-c, respectively. The ligament is loaded both by membrane and bending stresses, but the bending component increases with increasing ligament size. A 1.27-mm (0.05-in.)-wide ligament is loaded primarily by membrane stress. If we arbitrarily define the ligament as failing when its volume-averaged plastic strain reaches 100%, the ligament failure pressures are 15.5, 19.0, and 29.0 MPa (2.25 ksi, 2.75 ksi, and 4.2 ksi) for ligament widths of 1.27, 2.54, and 6.35 mm (0.05 in., 0.1 in. and 0.25 in.), respectively. Thus, for ligament widths ≥6.35 mm (≥0.25 in.), each of the two 12.7-mm (0.5-in.)-long cracks fail unstably at 29.0 MPa (4.2 ksi), i.e., the two cracks do not interact. For ligament widths <6.35 mm (<0.25 in.), the two cracks do interact, and the failure pressure of the ligament is reduced progressively with decreasing ligament width. For ligament widths ≥2.54 mm (≥0.1 in.), the cracks fail unstably upon ligament rupture. However, for a ligament width of 1.27 mm (0.05 in.), the cracks remain barely stable after ligament rupture, because the unstable failure pressure for a single 25.4-mm (1-in.)-long TW crack is 16.5 MPa (2.4 ksi).

(a) Crack geometry

(b) Stress-strain curve
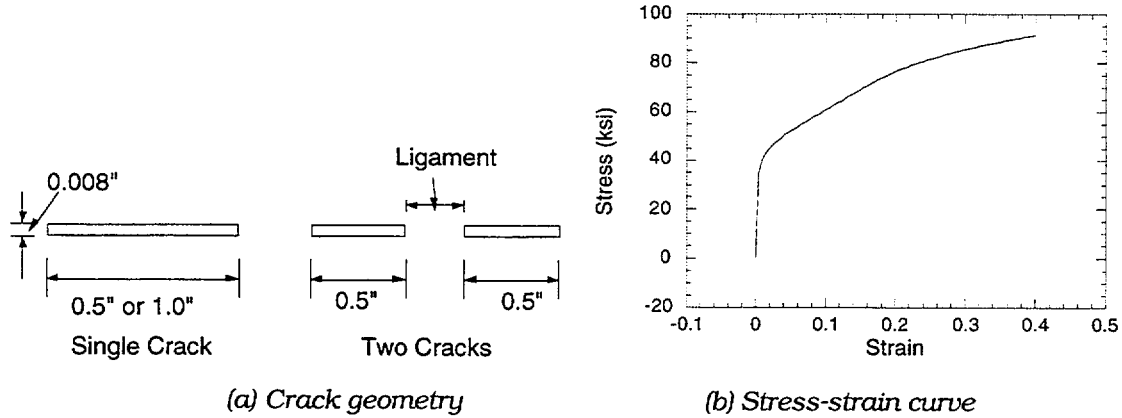
Fig. 4.30.   (a) Crack geometry and (b) stress-strain curve assumed for analysis.

(a)

(b)
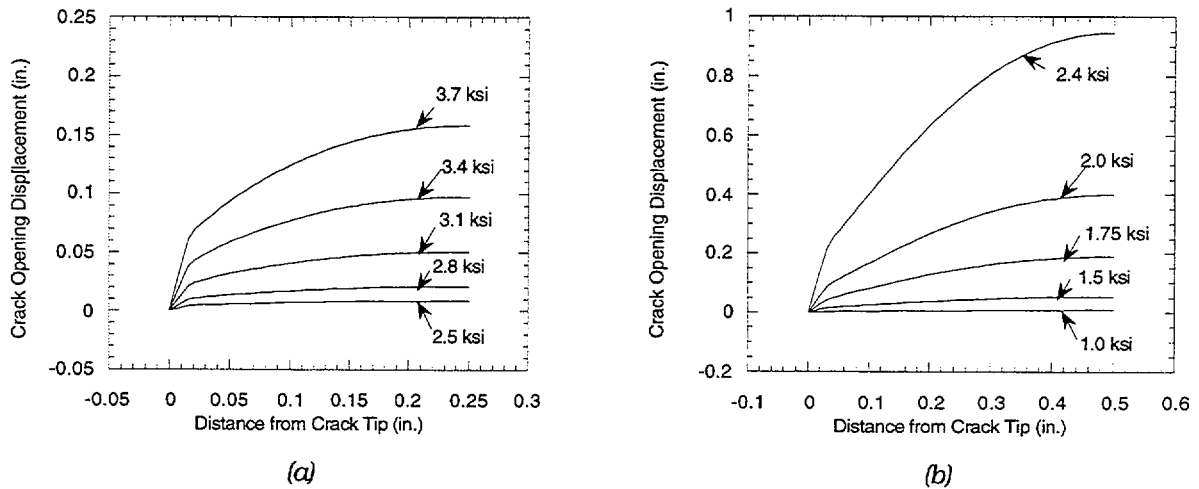
Fig. 4.31.   Calculated total crack opening displacement as a function of internal pressure for single (a) 12.7-mm (0.5-in.)-long and (b) 25.4-mm (1.0-in.)-long TW cracks.

The variations of total crack opening displacement over the crack surface for two collinear TW cracks of length 12.7 mm (0.5 in.) separated by ligaments of width 1.27, 2.54, and 6.35 mm (0.05 in., 0.10 in., and 0.25 in.) are shown in Figs. 4.33 a-c, respectively. Note that the asymmetry in the COD is reduced with increasing ligament size so that for ligament sizes of ≥6.35 mm (≥0.25 in.), the COD is almost as symmetrical as it is for two cracks separated by an infinite ligament width, again confirming that the two cracks do not interact when ligament widths are ≤6.35 mm (≥0.25 in.).
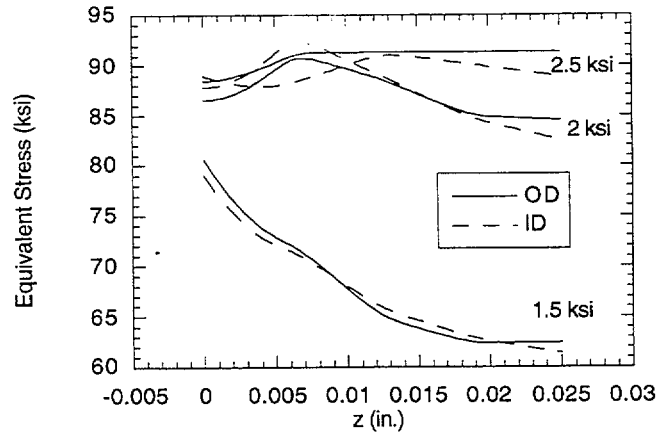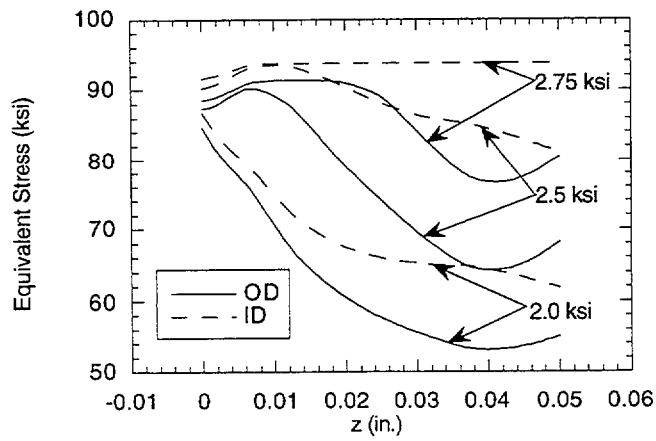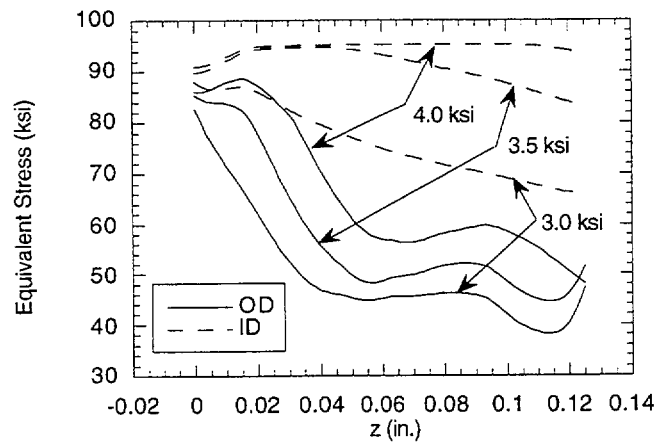
Fig. 4.32. *Variations of calculated equivalent stresses at ID and OD surfaces of ligament with pressure for two 12.7-mm (0.5-in.)-long TW cracks separated by ligaments of width (a) 1.27 mm (0.05 in.), (b) 2.54 mm (0.1 in.), and (c) 6.35 mm (0.25 in.).*

The variation of total crack opening area (COA) with pressure for two throughwall 12.7 mm (0.5 in.) collinear cracks with 1.27, 2.54, and 6.35 mm (0.05 in., 0.1 in. and 0.25 in.) ligament widths are shown in Fig. 4.34. The flaws are assumed to be 0.20 mm (0.008 in.) wide initially. Figure 4.34 also includes the COAs for a single 25.4-mm (1-in.) and 12.7-mm (0.5-in)-long TW cracks. Note that a single ligament of width 1.27 mm (0.05 in.) reduces the COA of a 25.4-mm (1-in.)-long crack significantly. For ligament widths ≥6.35 mm (≥0.25 in.), the total COA is the same as that of two isolated 12.7-mm (0.5-in.)-long flaws.

4.5 Test Matrix for Pressure and Leak-Rate Facility

Described below is a series of tests with EDM notches planned for the next 6 months. Axially flawed (EDM) specimens of 22.2-mm (0.875-in.)-diameter Valinco Alloy 600 steam generator tubes will be fabricated in duplicate. All specimens will be examined by the NDE group for EC characterization prior to testing.

4.5.1 Single Axial Flaw (13 tests)

The purpose of these tests (Table 4.3) is to fill the void in the existing data base for short and deep axial flaws and also to develop correlations between failure pressure and leak rate at room temperature with those at high temperature. Some of these specimens have been heat treated using the same procedure that is currently being used before stress corrosion cracking in the laboratory and then reexamined by the NDE group to check for any change in the EC signal prior to pressure and leak rate testing. A number of tests have been completed to date as indicated in Table 4.3.

4.5.2 Single Part-Throughwall Axial Flaw with Nonuniform Ligament (3 tests)

The purpose of these tests is to provide well-characterized analogs for laboratory-grown SCC cracks that have been observed to have approximately similar geometry as indicated by the EC +Point technique. These tests will help develop criteria for initial ligament failure and full ligament failure with pressure. The three planned tests are shown in Table 4.4. The third test in this series is nominally the same as the first except that it has a drilled throughwall segment at the center simulating throughwall segments often observed in SCC cracks. The hypothesis is that for ductile materials like Alloy 600, the failure behavior of flaws with localized throughwall segments is approximately the same as those without such throughwall segments.

4.5.3 Multiple Axial Flaws with Ligaments (6 tests)

The purpose of these tests is to develop failure pressure and leak rate correlations for multiple-axial (collinear) flaws separated by various ligament widths and thicknesses. In the tests (Table 4.5), the total length (L) and depth of the flaw will be held constant. The ligament width will be varied while the total ligament cross-sectional area is held constant. This will require reducing the ligament thickness in some tests from 100% of wall thickness by removing material from the OD. The hypothesis is that for a given number of ligaments, the total ligament cross-sectional area, rather than the ligament width or the location of the ligament within the wall thickness (i.e., whether at ID or OD or in between), determines the failure pressure and leak rate. It is expected that for thin-walled SG tubing, the location of the ligament within the wall thickness should be less important than the number and total cross-sectional area of the ligament.
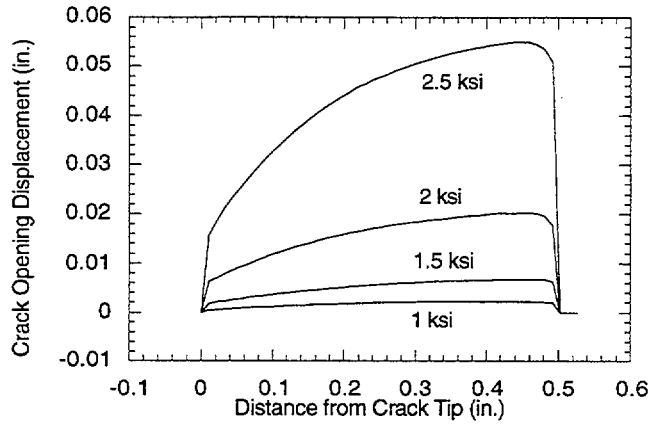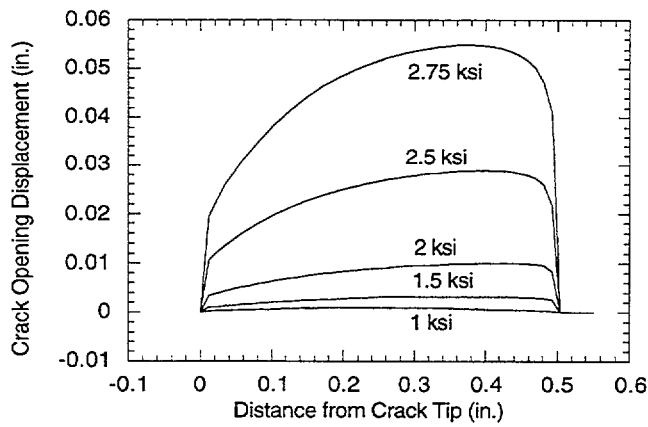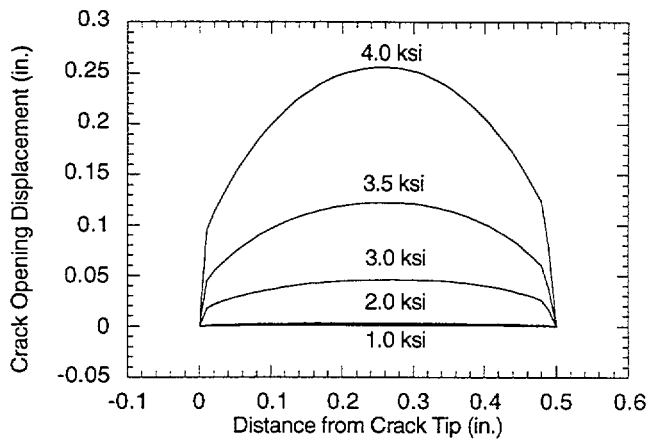
Fig. 4.33. *Variations of calculated crack opening displacements with pressure for two 12.7-mm (0.5-in.)-long TW cracks separated by ligaments of width (a) 1.27 mm (0.05 in.), (b) 2.54 mm (0.1 in.), and (c) 6.35 mm (0.25 in.).*
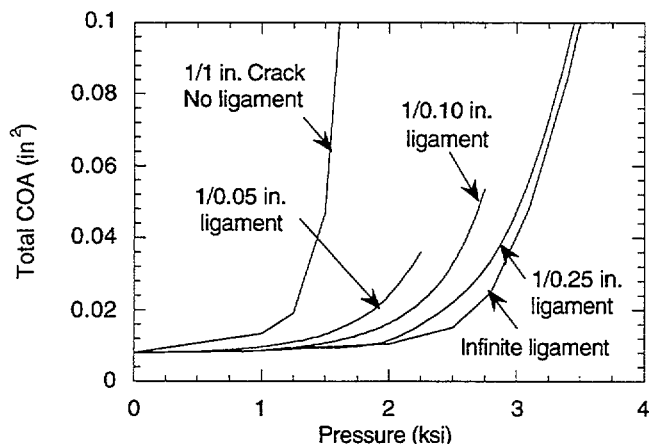
Fig. 4.34.   *Calculated variation of flaw opening area with pressure for single flaw 25.4-mm (1-in.) long and two flaws each 12.7-mm (0.5-in.) long separated by ligaments of various widths. Each flaw had an initial width of 0.20 mm (0.008 in.).*

4.6 Posttest Analysis of Tests

Three available correlations for predicting ligament failure of part-throughwall axial cracks were used for posttest analysis of the tests. A detailed discussion on these correlations is given in Ref. 1. The earliest correlation for calculating the pressure required to fail the remaining ligament (referred to as the Battelle Columbus Laboratories [BCL] correlation) is as follows:

$$p_{sc} = \frac{\overline{\sigma} h}{m_p R_m} = \frac{p_b}{m_p}, \tag{4.2a}$$

where p_b is the burst pressure of an unflawed tube, $\overline{\sigma}$ is the flow stress and

$$m_p = \frac{1 - \dfrac{a}{mh}}{1 - \dfrac{a}{h}}, \tag{4.2b}$$

$$m = 0.614 + 0.481\lambda + 0.386\exp(-1.25\lambda), \tag{4.2c}$$

$$\lambda = \left[12(1 - v^2)\right]^{\frac{1}{4}} \frac{c}{\sqrt{R_m h}} = \frac{1.82\,c}{\sqrt{R_m h}}, \tag{4.2d}$$

where h is the wall thickness, R_m is the mean tube radius, a is the crack depth, and $2c$ is the crack length. We emphasize that Eq. 4.2a gives only the pressure required to fail the remaining ligament.

Table 4.3. Estimated failure pressures for proposed tests on specimens with single axial flaw. Each test will be conducted in Argonne's Pressure and Leak-Rate Test Facility.
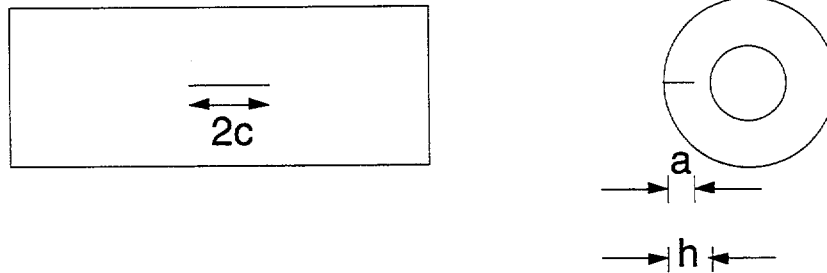
Flaw length 2c (mm [in.])		Flaw depth (a/h)	Test Temp. (°C)	Est. ligament rupture press. (MPa [ksi])		Est. unstable failure press. (MPa [ksi])		Status
6.35	(0.25)	90%	300	16.5	(2.4)	44.1	(6.4)	
8.89	(0.35)	90%	20/300	18.6	(2.7)	35.9	(5.2)	completed[a]
				16.5	(2.4)			
12.7	(0.5)	100%	20/300	-		29.0	(4.2)	completed[b]
12.7	(0.5)	80%	20/300	20.1^2	$(2.92)^b$	29.0	(4.2)	
21.6	(0.85)	80%	20/300	16.5	(2.4)	19.3	(2.8)	
25.4	(1.0)	100%	20	-		17.2^3	$(2.5)^c$	
38.1	(1.5)	80%	20	14.5^2	$(2.1)^b$	12.4	(1.8)	completed[d]

[a] This specimen was first tested at RT and then at 300°C without ligament rupture.

[b] This specimen was tested at RT.

[c] This test will be periodically unloaded for crack opening area measurement.

[d] Duplicate tests on as-received tubes as well as a single test on heat-treated tube.

Based on tests conducted on SG tubes at PNNL, an empirical equation referred to as the INEEL/PNNL correlation was proposed and can be expressed as Eq. 4.2a with m_p given by the following:

$$m_p = \left[1 - \frac{a}{h} + \frac{a}{h}\exp(-0.51\lambda)\right]^{-1}. \tag{4.3}$$

The PNNL tube test data were reanalyzed (including remeasurement of the flaws by posttest fractography) by ANL and it was proposed that Eq. 4.2b be modified as follows (referred to as the ANL equation):

Table 4.4. Matrix of tests to establish correlations for ligament failure pressure, leak rate, and unstable burst pressure on specimens with axial flaws with nonuniform ligament thickness.
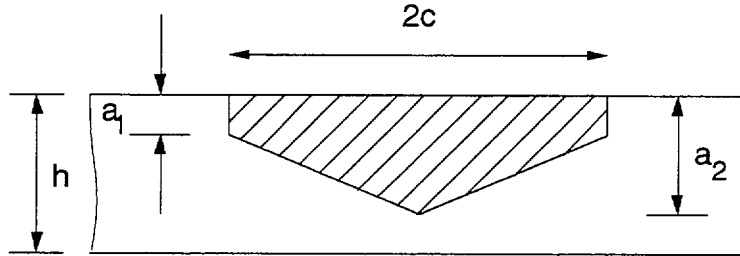
Flaw Length 2c (mm [in.])		a_1/h (%)	a_2/h (%)	Test Temp. (°C)	Ligament rupture pressure (MPa [ksi])	Unstable burst pressure (MPa [ksi])
25.4	(1.0)	50	90	300	-	-
25.4	(1.0)	80	90	300	-	-
25.4	(1.0)	50	90[a]	300	-	-

[a] This specimen will have a drilled hole at the deepest point of the crack to breach the ligament locally.

$$m_p = \frac{1 - \alpha \dfrac{a}{mh}}{1 - \dfrac{a}{h}},$$

(4.4a)

where

$$\alpha = 1 + 0.9\left(\frac{a}{h}\right)^2\left(1 - \frac{1}{m}\right).$$

(4.4b)

Except for short and deep cracks, Eq. 4.4a predicts ligament failure pressures similar to those predicted by Eq. 4.2a.

Based on limited tensile and burst test data, the flow stresses of the as-received and sensitized tubes at room temperature were taken as 538 and 434 MPa (78 and 63 ksi), respectively. The flow stress at 300°C was assumed to be 90% of the room-temperature value.

Table 4.5. *Matrix of tests to establish correlations for failure pressure and leak rate on specimens with coplanar axial flaws with ligaments.*
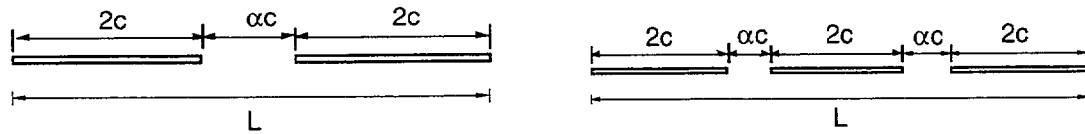
No. of flaws	L (mm [in.])		a/h (%)	Ligament width αc (mm [in.])		Ligament thickness (%)	Test Temp. (°C)
2	12.7	(0.5)	100	0.25	(0.01)	100	300
2	25.4	(1.0)	100	1.27	(0.05)	100	300
2	25.4	(1.0)	100	0.64	(0.025)	100	300
5	25.4	(1.0)	100	0.25	(0.01)	100	300
5	25.4	(1.0)	100	0.64	(0.025)	50	300
5	25.4	(1.0)	100	1.27	(0.05)	25	300

4.6.1 Notched Specimen Tests

A comparison of the observed failure pressures for duplicate tests at room temperature on as-received tubes with an 80% deep, 38.1-mm (1.5-in.)-long axial flaw with predicted failure pressures by the three available correlations (BCL, INEL/PNNL and ANL correlations) are given in Fig. 4.35a. A similar comparison for a sensitized tube is given in Fig. 4.35b. All three correlations give reasonable predictions for ligament failure pressure with the ANL correlation giving the closest prediction. An as-received tube containing a 80% deep 38.1-mm (1.5-in.)-long axial crack was analyzed by finite element analysis (FEA). The computed results plotted in Figs. 4.36a-b confirm that the failure of the ligament occurs soon after the entire ligament at the throughwall crack tip deforms plastically. It should be noted that because the unstable failure pressure of a 38.1-mm (1.5-in.)-long TW axial crack is significantly lower than the ligament failure pressure, all three correlations predict that the resulting throughwall crack upon ligament failure should be unstable. Although none of the tubes failed by unstable bursting because of immediate depressurization of the system after ligament rupture, they all had large crack openings (fish-mouth) after the tests.

In contrast to the specimens with 38.1-mm (1.5-in.)-long crack, an as-received specimen with a nominally 8.9-mm (0.35-in)-long, 90% TW axial notch did not experience ligament failure at room temperature at the maximum system pressure. Later, the same specimen did not fail when subjected to maximum system pressure at 300°C. A plot of the predicted ligament failure pressures by the three correlations, shown in Figs 4.37a-b, confirm earlier

suspicion that the BCL correlation tends to overestimate the damaging effect of short deep cracks. It appears that the actual failure pressure may be even higher than that predicted by the ANL correlation. This test will be repeated at 300°C in the future.

4.6.2   Tests on Specimens with Laboratory-Grown SCC Cracks

In contrast to machined notches that have constant depth and are rectangular in shape, laboratory-grown SCC cracks are irregular in shape and have variable depths along their lengths.   Instead of being a single planar crack, they are composed of a family of crack segments in different planes. Local variations in crack depth and geometry are smoothed out in the EC measurements because the EC signals are necessarily averaged over a finite volume, and hence the EC data tend to show a relatively smooth variation of crack depth along the crack length. This is evidenced by the fact that although all four specimens tested to date have shown leakage under low gas pressure prior to testing, the EC +Point method has failed to detect or identify the locations of these throughwall segments.   However, no leakage of water was detected through these cracks until much higher pressures were applied.

Currently, no models are available for predicting the ligament failure pressure of cracks with such complex geometries. From a limit analysis viewpoint, it can be argued that the collapse behavior of a crack tip ligament with an irregular point-by-point variation of crack depth should be similar to a crack with a smoothed out "average" crack depth profile. For the present, we assume that the average profile measured by the EC +Point method is relevant for limit analysis. With this assumption, although the real crack may have short throughwall segments at a number of locations, from the viewpoint of plastic collapse of the ligament, the tube behaves as if it has a smoothly varying average ligament thickness (or crack depth) profile.

Figures 4.38a-b and 4.39a-b show EC +Point profiles for specimens tested at room temperature, and calculated ligament failure pressures by three available correlations for rectangular cracks with various crack depths. Crack lengths are determined from the EC profile after excluding the tails over which the signal drops off rapidly. Figures 4.40a-b and 4.41a-b show similar plots for tests conducted at 300°C.

Leakage in specimen SGL-177 started abruptly at 16.9 MPa (2450 psi) with an initial leakage rate of 0.04 L/min (0.01 gpm), but increased under constant-pressure hold to 0.26 L/min (0.07 gpm), indicating time-dependent progressive failure of the ligament at room temperature. Although the leakage rate increased to 1.7 L/min (0.44 gpm) when the pressure was increased to 19.3 MPa (2800 psi), the full ligament was almost certainly not ruptured because this leakage rate is very low compared to that from machined notches of comparable length. This specimen had a highly profiled crack depth (depth ranged from 50% to 90% TW) in which failure of the ligament appeared to occur progressively (but stably) with increasing pressure. Specimen SGL-195, which had a much more uniform crack depth than SGL-177, developed an initial leak (leak rate <0.04 L/min [<0.01 gpm]) at 14.7 MPa (2129 psi), which abruptly increased to 32 L/min (8.6 gpm) at 15.5 MPa (2250 psi), indicating a full ligament rupture, since this leak rate is comparable to that of a machined notch of similar length. Specimen SGL-104 (tested at 300°C), which also had a relatively uniform crack depth, experienced an abrupt increase in leakage rate from zero to 21 L/min (5.6 gpm) at 16.2 MPa (2352 psi), indicating a full ligament rupture.   Although its leakage rate increased with increased pressure, it did not increase under constant-pressure hold. Finally, specimen SGL-219 (tested at 300°C), which had a short crack segment with thick crack tip ligament
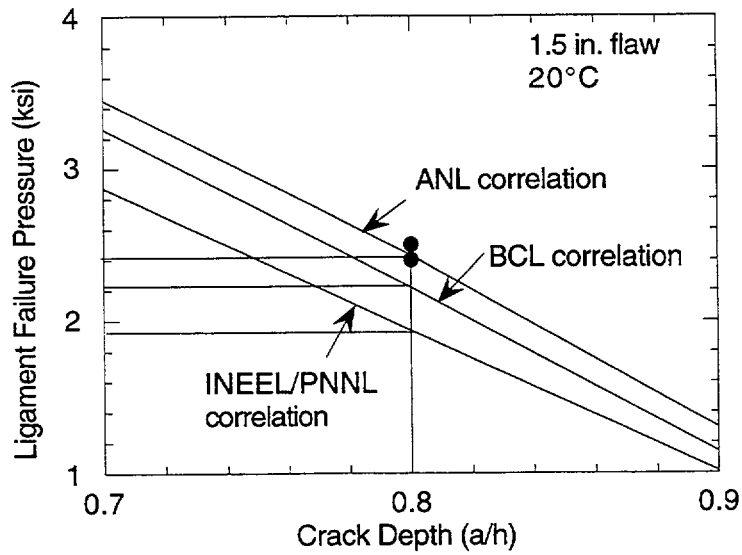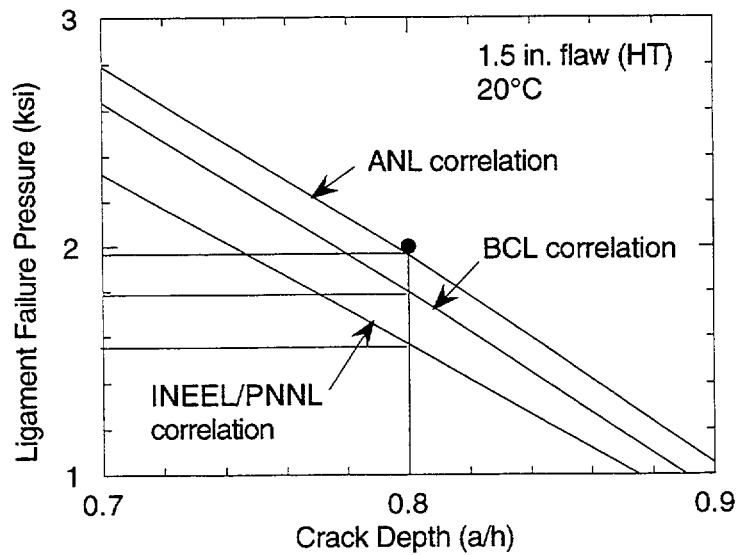
Fig. 4.35. Comparison of observed ligament failure pressure with those predicted by ANL correlation, BCL correlation, and INEEL/PNNL correlation for specimens with 38.1-mm (1.5-in.)-long, 80% TW axial flaw in (a) as-received tube and (b) heat-treated (sensitized) tube.
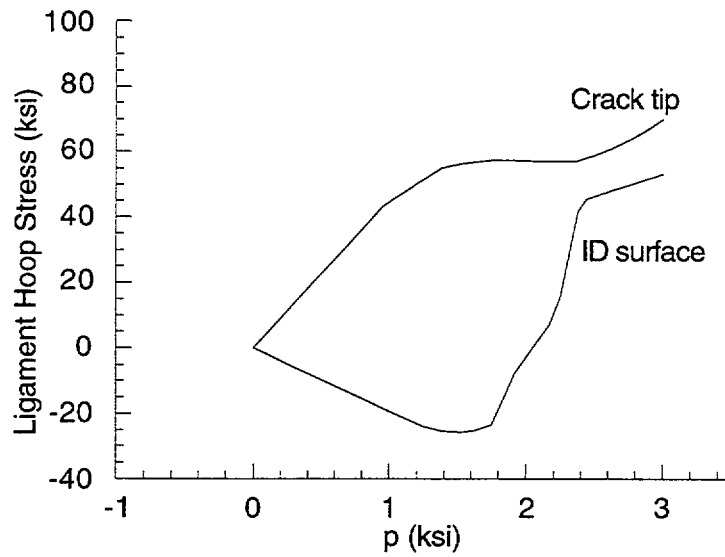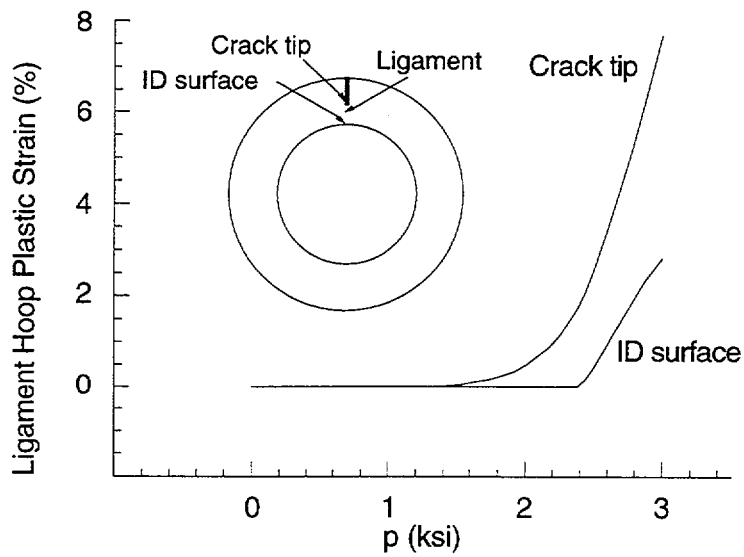
Fig. 4.36. Calculated (by FEA) variations of (a) ligament hoop stress and (b) ligament hoop plastic strain with pressure at crack tip and at ID surface of as-received tube with 38.1 mm (1.5-in.)-long, 80% TW OD surface flaw.
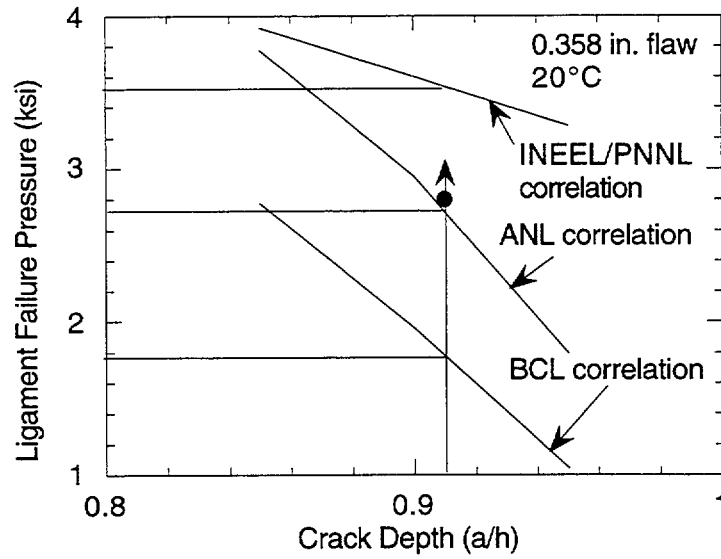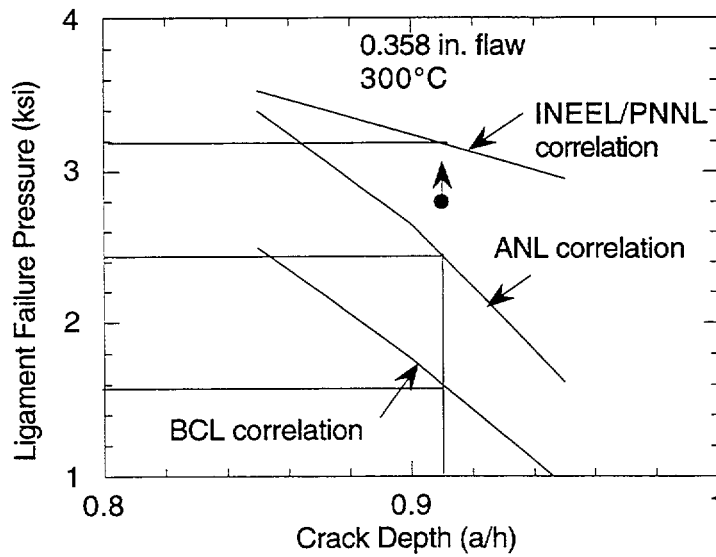
Fig. 4.37. Comparison of observed ligament failure pressure with those predicted by ANL correlation, BCL correlation, and INEEL/PNNL correlation for as-received tube with nominally 8.9-mm (0.35-in.)-long, 90% TW axial flaw at (a) room temperature and (b) 300°C. Test was first conducted at room temperature, and the same specimen was later tested at 300°C. Neither test resulted in ligament failure at highest system pressure.
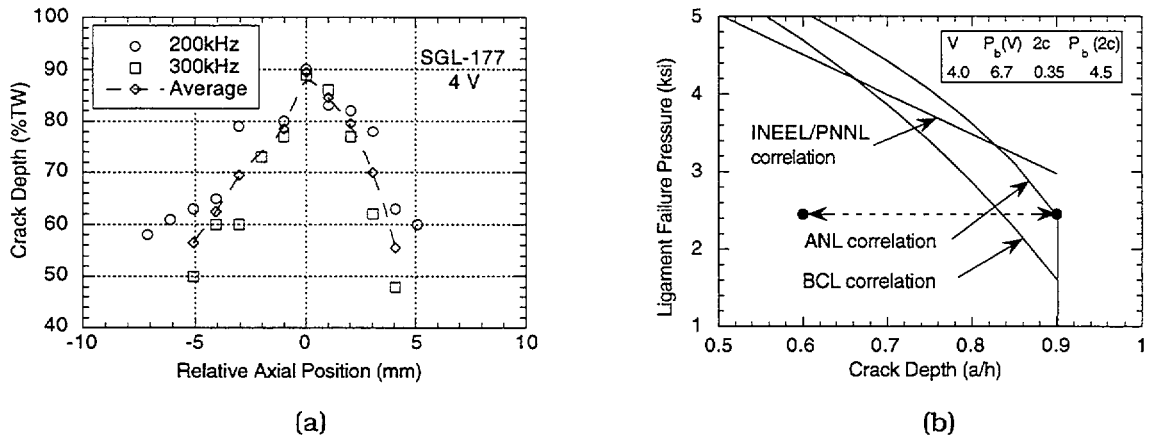
Fig. 4.38. (a) Measured crack depth profile in specimen SGL-177 by EC +Point and (b) predicted
ligament failure pressure at room temperature for 8.9-mm (0.35-in.)-long rectangular
crack as a function of crack depth. Circles represent range of crack depth measured
by EC +Point method at pressure corresponding to first measurable leakage rate.
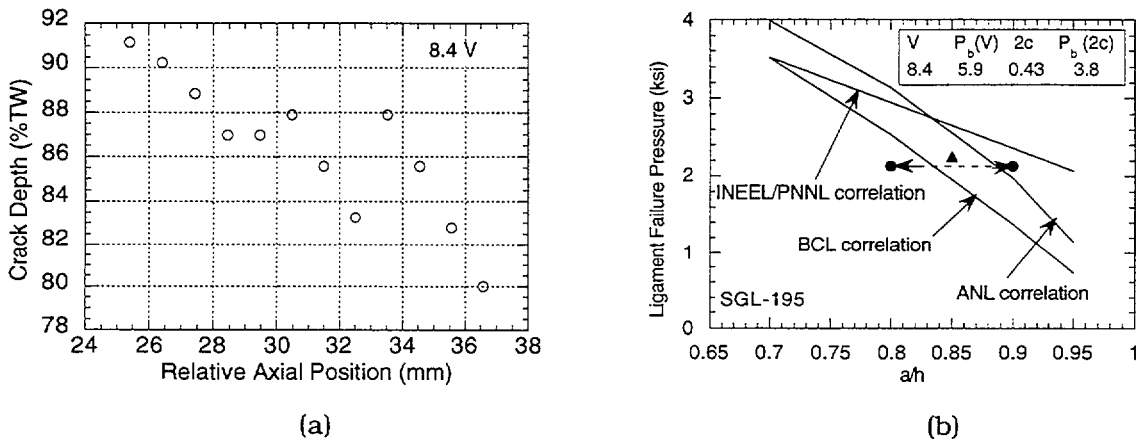
Fig. 4.39. (a) Measured crack depth profile in specimen SGL-195 by EC +Point and (b) predicted
ligament failure pressure at room temperature for 10.9-mm (0.43-in.)-long rectangular
crack as a function of crack depth. Circles represent range of crack depth measured
by EC +Point method at pressure corresponding to first measurable leakage rate, and
triangle represents average crack depth.
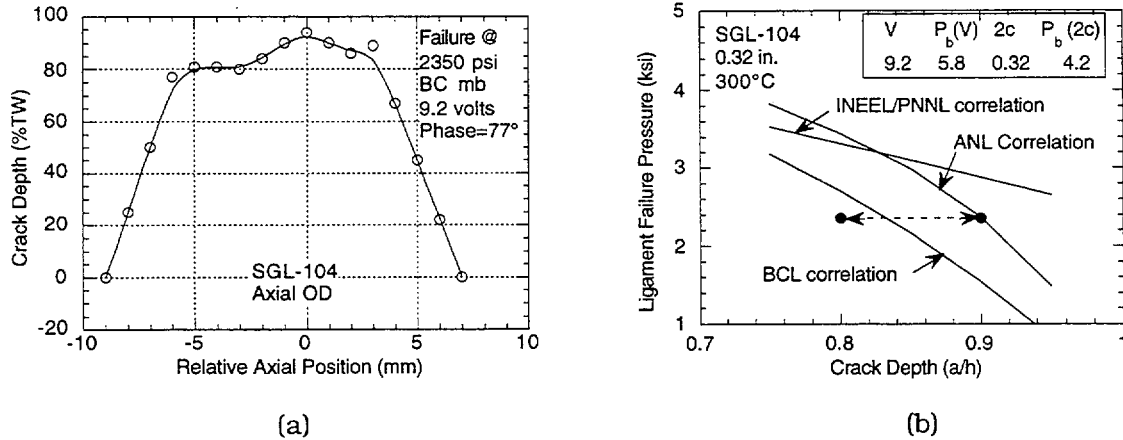
Fig. 4.40.   (a) Measured crack depth profile in specimen SGL-104 by EC +Point and (b) predicted ligament failure pressure at 300°C for 8.1-mm (0.32-in.)-long rectangular crack as a function of crack depth.   Circles represent range of crack depth measured by EC +Point method at pressure corresponding to first measurable leakage rate.
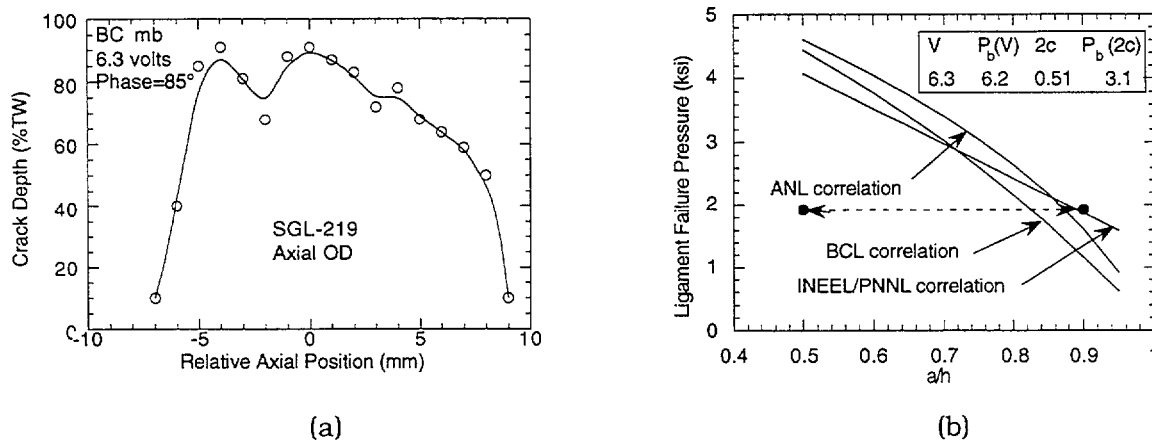
Fig. 4.41.   (a) Measured crack depth profile in specimen SGL-219 by EC +Point and (b) predicted ligament failure pressure at 300°C for 13.0-mm (0.51-in.)-long rectangular crack as a function of crack depth.   Circles represent range of crack depth measured by EC +Point method at pressure corresponding to first measurable leakage rate.

separating two crack segments with thin ligaments, developed a leak at 13.3 MPa (1925 psi) (leak rate = 3.7 L/min [0.97 gpm]).   Under a constant-pressure hold at 16.2 MPa (2346 psi), the leakage rate increased from 14 to 39 L/min (3.7 to 10.3 gpm), indicating time-dependent progressive rupture of a portion of the remaining ligament.   The final leakage rate is comparable to the leakage rates observed in tests with machined notches of comparable lengths.   In all cases, the pressure at first measurable leakage rate agrees very well with the failure pressure predicted by the ANL correlation for a rectangular crack with depth equal to the maximum depth of the crack as indicated by EC +Point measurement.   We expect that the

criterion for full ligament rupture can be related to the failure of a uniform ligament with a width equal to the average width of that of the actual crack. This will be confirmed after the tests are completed in a high-pressure test facility.

4.6.2.1   Conclusions

Although more tests are needed for confirmation, the results so far seem to suggest that part-throughwall axial cracks with highly profiled ligaments may experience some increase in leakage rate during constant-pressure holds at both room temperature and 300°C. The increasing leakage rate is very likely a consequence of progressive through-thickness crack tip ligament rupture. Finally, the pressure to cause the first measurable leakage rate appears to correspond to the predicted ligament failure pressure of a rectangular crack with length as measured by the EC +Point method (ignoring the tails where the signal drops off rapidly) and depth equal to the maximum depth as measured by the same method. This criterion appears valid even when the crack is known to have initial throughwall segments as evidenced by gas bubble leakage at 0.28 MPa (40 psi) pressure (but no detectable water leakage up to almost 13.8 MPa [2000 psi]).

4.7   Literature Survey on IGA/IGSCC initiation

We have prepared a draft of a literature review titled "Assessment of Current Understanding of Mechanisms of Initiation, Arrest, and Reinitiation of Stress Corrosion Cracks in PWR Steam Generator Tubing." The draft report was sent to Dr. A. P. L. Turner of Dominion Engineering, who has reviewed the report and sent us their comments and some minor criticisms. These will be taken into account in revising the report, and a final report will be issued by March 1999.

The literature on IGA/IGSCC of Alloy 600 in PWR water is vast, with contributions from every country that operates PWRs. The available literature is exclusively on crack initiation and growth. Literature on the phenomena of crack arrest and crack reinitiation in Alloy 600 in PWR water is not extensive. Despite extensive research extending over four decades, the definitive mechanisms responsible for PWSCC on the primary side and IGA/IGSCC on the secondary side remain elusive. However, a large body of experimental work has helped to establish a number of empirical facts and models for IGA/IGSCC of Alloy 600.

Although more than 200 publications were reviewed for this report, the search was not exhaustive. A historical study of the corrosion problems in PWR SG tubing shows that a succession of failure processes have afflicted the industry in the United States and around the world since the early 1960s. Current steam generators are faced with three main types of intergranular corrosion problems. The first is primary water stress corrosion cracking (PWSCC), typically found in regions of significant residual stress such as the roll transition zone where the tubes are expanded into the tube sheet and at the U-bends and tube dent locations. On the secondary side, intergranular attack (IGA) and outer-diameter stress corrosion cracking (ODSCC) typically occur at the tube support plate crevices and under sludge piles at the junctions of tubes with tube sheet and tube support plates. However, ODSCC in the tube free span is also occasionally observed.

A large experimental data base is available on stress corrosion crack initiation and propagation in Alloy 600 SG tubing. These data were primarily generated by using autoclave systems that simulate either the primary or secondary side chemical environment, although limited data from model boiler tests have also been reported. A complicating factor in

planning autoclave tests has been our incomplete knowledge of the chemical and electrochemical state within the crevices of operating steam generators. Despite a large body of empirical evidence linking various chemical, electro-chemical, metallurgical and environmental factors with PWSCC and IGA/ODSCC, the exact mechanisms responsible for these phenomena remain elusive.

Among the empirical facts that are common to both primary and secondary side SCC are:

- High-temperature mill-annealed or thermally treated Alloy 600 with continuous or semi-continuous grain boundary carbides is generally more resistant to IGA/IGSCC than low-temperature mill-annealed material.

- A key to understanding IGA/IGSCC mechanisms is the effect of the environment on the nature, properties, and stability of the surface oxide film.

- Increased temperature leads to shorter IGA/IGSCC life, both for crack initiation and crack propagation. The relatively high apparent activation energy of 30-40 kcal/mole for IGSCC with a large scatter band indicates that the rate-limiting step cannot be liquid diffusion.

- Resistance to IGSCC is highest at neutral pH and decreases with increasing or decreasing pH. The presence of lead is detrimental to TGSCC/IGSCC from acidic to caustic pH.

- The grain-boundary sliding rate (rather than total creep rate) appears to be important for IGSCC. Grain boundaries that are resistant to sliding are also resistant to IGSCC.

4.7.1 PWSCC

The threshold stress for PWSCC is relatively high for mill-annealed Alloy 600. A high stress near yield is necessary for PWSCC cracks to initiate, with the crack initiation time varying approximately inversely with the fourth power of stress. Cold work decreases life (factor of 3-4), and thermal treatment increases life (factor of 2-3). The smaller the grain size (or higher the yield stress), the more susceptible is Alloy 600 to PWSCC.

PWSCC life decreases with hydrogen partial pressure up to 0.05 MPa (7 psi), beyond which the effect saturates and life actually increases. Laboratory tests have shown that Alloy 600 cracks more readily in lithiated borated water than in pure water. Experimental data fail to show any consistent influence of trace impurities such as S, P and Si on PWSCC life.

The scatter in the crack growth rate data from various sources as a function of stress intensity factor is a factor of ≈ 100. The threshold stress intensity factor is ≈ 10 MPa$\sqrt{m}$.

PWSCC is observed over a limited range of potential centered on the Ni/NiO equilibrium in neutral to slightly alkaline solutions. The composition of the spinel oxide surface film changes rapidly within this region, and the film rupture/dissolution/repassivation mechanism suggests itself as a natural candidate. It has been suggested that ion transport in the oxide or oxygen transport into the metal may be the rate-controlling process, which would account for the high apparent activation energy. However, there is other experimental evidence that link hydrogen with PWSCC, although no quantitative model based on hydrogen-assisted cracking for predicting PWSCC life currently exists.

Although the mechanisms are uncertain, there is an extensive data base on crack initiation and crack propagation of Alloy 600 in hydrogenated deaerated water at high temperature. Future tests should be directed toward measuring crack growth rates of relatively short axial and circumferential cracks, using systems for monitoring crack lengths during the tests.

4.7.2 IGA/ODSCC

In contrast to the primary side, the chemical and electrochemical environment in the secondary side is vastly more complex because much of the secondary side cracking occurs in crevices and under sludge piles at the TTS and TSP junctions. The exact environment in these inaccessible regions is still largely unknown because direct measurements are virtually impossible. Data from model boilers may not be representative of plant conditions, because studies commonly use increased bulk water concentrations of impurities to accelerate the tests. It was traditionally held that local boiling and poor coolant circulation would tend to concentrate caustic impurities in superheated crevices and under sludge piles. This conclusion was supported by calculations that used codes such as MULTEQ with inputs from hideout return data. Therefore, a great deal of experimental data has been generated on the IGA/IGSCC behavior of Alloy 600 in highly caustic solutions, and a large data base and some mechanistic understanding on IGA/IGSCC of Alloy 600 in caustic solutions has been developed.

Several recent analyses of the deposits on pulled tubes suggest that the environment in the crevices is neither highly caustic nor highly acidic, but is near neutral to slightly alkaline. The presence of plugged crevices increases the potential for local dry-outs, and the crevice environment may approach that of laboratory tests with doped steam. Some of the secondary-side cracking observed in plants is difficult to explain as occurring in a liquid environment because not enough impurities enter the steam generators to fill the crevice volumes in which cracking occurs. A possible explanation for the cracking over full height of the crevice, despite the crevice not being filled by liquid, is that much of the cracking occurs in a contaminated steam environment.

It is clear that the greatest uncertainty in predicting IGA/IGSCC life of steam generator tubing is predicting the local environment within the crevice or under the sludge pile, where crack initiation occurs. Further, the crack initiation data generated in autoclave systems are not directly applicable to predicting the time to crack initiation in steam generator tube bundles, because the majority of the time required to nucleate cracks in a steam generator is consumed in developing the necessary local chemistry within the crevices. This process is, of course, dependent on the operational details of each steam generator. Nor are model boiler data very helpful for this purpose, because the concentration of bulk impurities is typically increased to accelerate the tests. One could argue from laboratory data on caustic or acidic stress corrosion cracking that once the appropriate chemistry is established within the crevices or under sludge piles, crack initiation should occur relatively quickly.

Because direct measurement of crevice chemistry in steam generators is extremely difficult, deposits from tube support plate and tube sheet crevices of retired steam generators should be chemically analyzed to elucidate the crevice chemistry. Model boiler testing, accelerated by chemical or thermal means, should be conducted in parallel to refine, improve, and validate models for predicting crevice chemistry. Future autoclave testing should be concentrated on generating crack initiation and crack propagation data in near-neutral high-temperature water and "doped" steam environments.

4.8 Examination of McGuire Steam Generator Tubes

The previous progress report provided a detailed description of the removal of tube and tube sections from the retired McGuire steam generators.[1] As stated in that report, portions of 11 individual tubes were pulled from steam generator D, as were two tube sheet samples containing 8 and 12 tubes, respectively. Two TSP sections containing ≈45 and ≈25 tube intersections, respectively, were also removed from the first TSP level of steam generator B.

In November 1997, the final cost for a fixed-price contract for the acquisition of the McGuire tubes was agreed to with Duke Engineering & Services (DES), and final payment was made. This cost included all of the Westinghouse and PCI subcontract work, as well as the costs for on-site support services provided by DES, including packaging and shipping the samples, and the remaining waste disposal. In addition, subcontracting costs were incurred with Golder Federal Services for the efforts of Dr. Robert Clark during the sampling operation.

The McGuire tube samples arrived at ANL on December 4, 1997, in four large wooden crates. The "hottest" of these crates had a reading of 650 mR/h at one surface, and the remaining crates had contact readings of 250 to 500 mR/h. These high radiation fields caused immediate storage problems, and ANL Health Physics personnel determined that the storage pit in the high-bay area of Building 212 where long-term storage was planned was not acceptable without modifications. In particular, it was necessary to build and install a secured door to prevent inadvertent access to the pit. Secondly, upgraded barriers were required at floor level above the pit to prevent personnel from inadvertently entering this region of above-normal radiation fields.

Modifications were also necessary in the glovebox where decontamination and sample handling were to be carried out. Specifically, the high radiation fields required that the floor of the glovebox be shielded and that leaded glass be installed around the glovebox perimeter to reduce the radiation exposure of the personnel working on the samples. In addition, upgrades to the glovebox ventilation system were required.

Decontamination of the McGuire tubes was then initiated. The tube selected for the initial trial was section 4 of tube R14 C55, one of the tubes pulled from steam generator D. This tube section was ≈1 m long and, as removed, had an overall activity level of ≈50 mR/h on contact. The initial loose (smearable) contamination level, as determined by wiping, was ≈5,000 disintegrations/min (dpm) β–γ on the outside surface. Initial smears of the inside surface were not taken.

Decontamination was first attempted by wiping the tube surfaces with liquid detergent and water. However, this process was found to increase rather than decrease the level of loose contamination, apparently because previously fixed surface contamination was being loosened. The loose contamination level after the first series of wipes was found to be ≈15,000 dpm at the outside surface and 4,500 dpm at the inside surface. Additional wiping with the same solution further increased the loose contamination levels to ≈25,000 dpm at the outside surface and ≈11,000 dpm at the inside surface.

At this point, a commercial decontamination solution sold under the product name "React" was employed. This solution is sprayed onto the tube surfaces (or, in the case of the tube ID, sprayed onto the wiping cloth) and then wiped off. After an extended treatment using this procedure, the level of contamination at the outside surface was reduced to ≈210 dpm. Decontamination of the tube ID continued, with the goal of reducing the levels of loose

contamination at both surfaces to <200. The overall level of fixed activity for this sample was reduced from 50 to 25 mR/h on contact.

Decontamination of sections 3 and 5 of tube R14 C55 was performed in a similar fashion. In both cases, successful decontamination required time-consuming repetitive applications of the decontamination solution and subsequent wiping of the ID and OD surfaces. Frequent cleaning of the glovebox gloves and interior surfaces was also necessary to prevent recontamination of the tube surfaces. Section 3 initially had a fixed contamination level of 30 mR/h at the OD surface and loose levels of 24,000 and 104,000 dpm at the OD and ID surfaces, respectively. After decontamination, the level of fixed contamination at the OD surface remained at 30 mR/h, but the levels of loose contamination were reduced to 180 dpm at both the ID and OD surfaces. Section 5 initially had levels of 41 mR/h fixed and 20,000 and 60,000 dpm loose at the OD and ID surfaces, respectively, and these were reduced to 37 mR/h fixed and 250 and 200 dpm loose at the OD and ID surfaces, respectively.

5 Integration of Results, Methodology, and Technical Assessments for Current and Emerging Regulatory Issues (D. S. Kupperman and D. R. Diercks)

5.1 NDE for Electrosleeved Tubes

Documents on the electrosleeving process for repairing tubes and qualification of ultrasonic NDE were reviewed. Eddy current examination of electrosleeved tubes with EDM notches has been carried out at ANL. In addition, ultrasonic probes for the evaluation of electrosleeved tubes have been assembled. These probes are being used to help assess the capability of ultrasonic techniques (UT) to detect and characterize defects in tubes repaired by the electrosleeving process.

5.1.1 Ultrasonic versus Eddy Current NDE

The ultrasonic probes used for detection of circumferential and axial cracks have been sized for the opening and curvature of a 22.2-mm (7/8-in.)-diameter electrosleeved tube. One circumferential probe operating at 5 MHz launches 45° shear waves in a pulse echo mode from the tube ID, with either water or glycerol used as a couplant. A second probe launches 70° shear waves. The echoes for both angles from a 13-mm (0.5-in.)-long, 0.5-mm (20-mil)-deep (40% TW) OD circumferential EDM notch in the parent tube of an electrosleeved tube are detectable. A third compound probe launches 45° and 70° waves traveling around the tube to detect axially oriented flaws. Echoes from a 0.5-mm (20-mil)-deep (40% TW) OD axial EDM notch in the parent tube are detectable.

The signals from the 45° beams are generally stronger than the 70° beam, as expected. However, the 70° beam may be more effective in detecting planar flaws that do not intersect either the ID or OD of the tube, thus eliminating the efficient corner-trap reflector. Detection of notches in these tubes is possible, despite the reduction in quality of the signal due to the rough surface of the electrosleeve. The use of 5 MHz rather than the higher frequencies helps minimize signal distortion due to surface roughness. However, echoes from SCC are expected to be considerably weaker than from notches because of the tightness of the cracks. The results of these and future efforts involving laboratory-cracked tubes will help assess the capability of UT to detect and characterize defects in tubes repaired by the electrosleeving process.

Ultrasonic echo patterns for tests carried out at ANL on electrosleeved tubes with OD EDM notches are presented in Figs. 5.1-5.4. For each ultrasonic echo pattern, there are corresponding EC traces obtained with a +Point™ probe at 100 and 300 kHz. It is somewhat surprising that EC signals from notches are present for the +Point at 300 kHz, but the conductivity of the electrosleeve material is likely to be significantly different from conventional nickel. A piece of copper (20 x 5 x 1 mm) placed on the outside of a flaw-free electrosleeved tube can be seen easily at 300 kHz. Figure 5.1 shows the results for a 1-mm (0.040-in.)-deep (80% TW) OD circumferential notch in the parent tube. Ultrasonic (70° shear) and EC flaw signals are both clear. Figure 5.2 shows the results for a 0.5-mm (0.020-in.)-deep (40% TW) OD circumferential notch in the parent tube. Ultrasonic (70° shear) and EC flaw signals are again both clear. Figure 5.3 shows the results for a 1-mm (0.040-in.)-deep (80% TW) OD axial notch in the parent tube. Ultrasonic (70° shear) and EC flaw signals are both clear, but the UT signal has a better S/N ratio. Figure 5.4 shows the
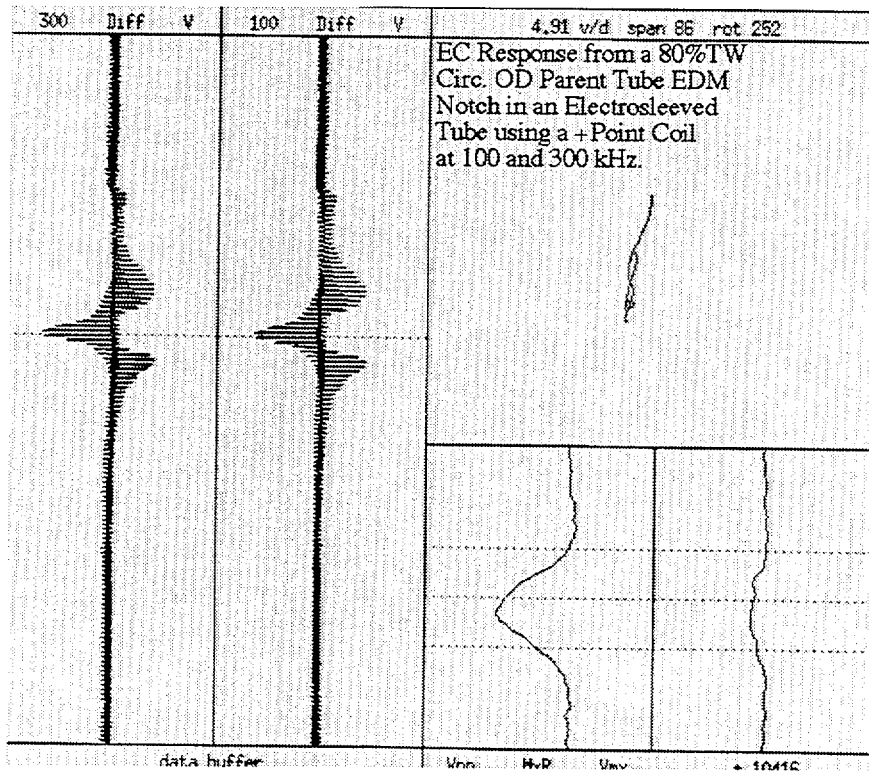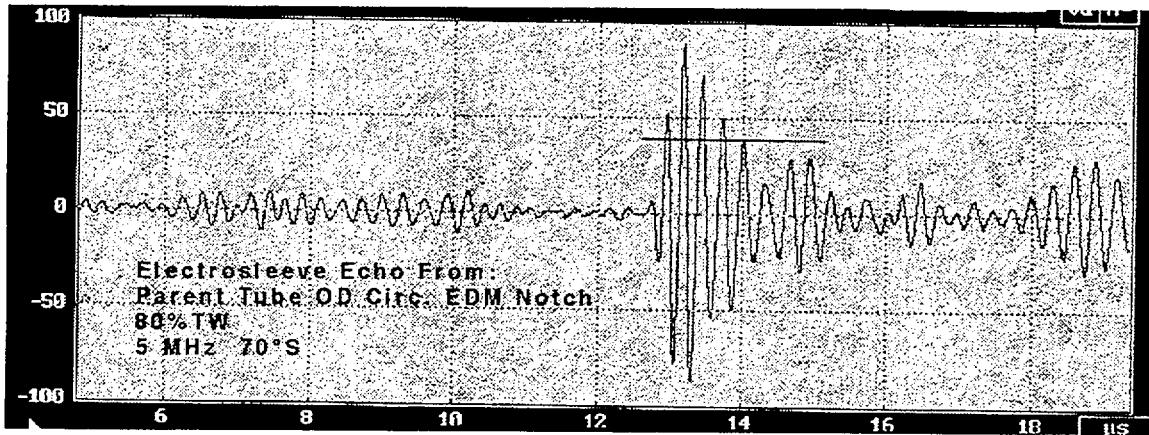
Fig. 5.1.   *Ultrasonic (top) and eddy current (bottom) signals from 1-mm (0.040-in.)-deep (80% TW) OD circumferential notch in parent metal of electrosleeved tube. Ultrasonic (70° shear) and EC flaw signals are both strong and clear.*
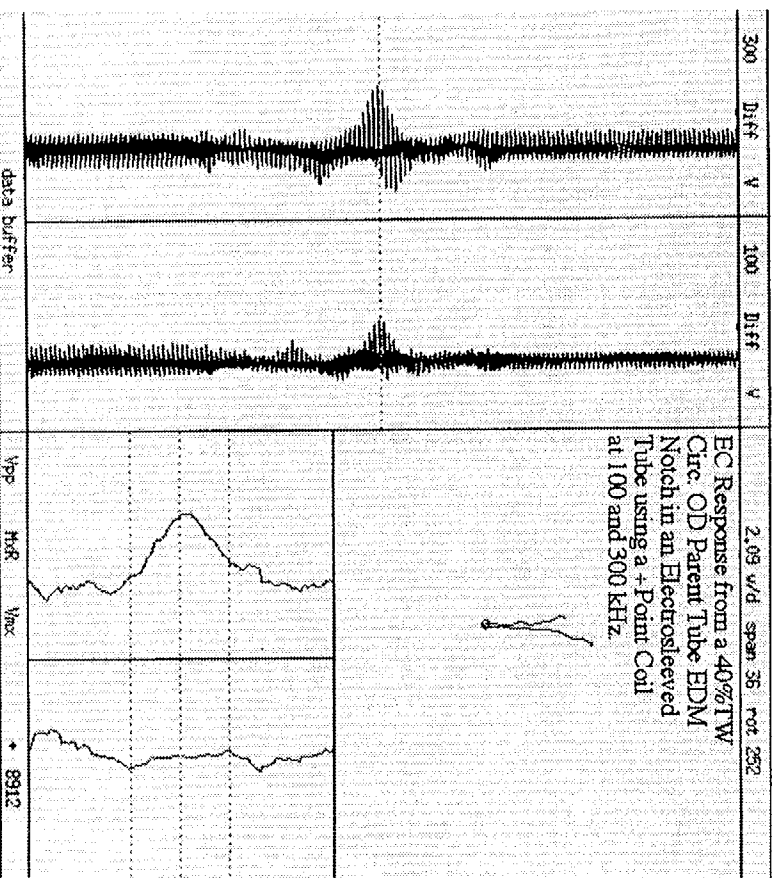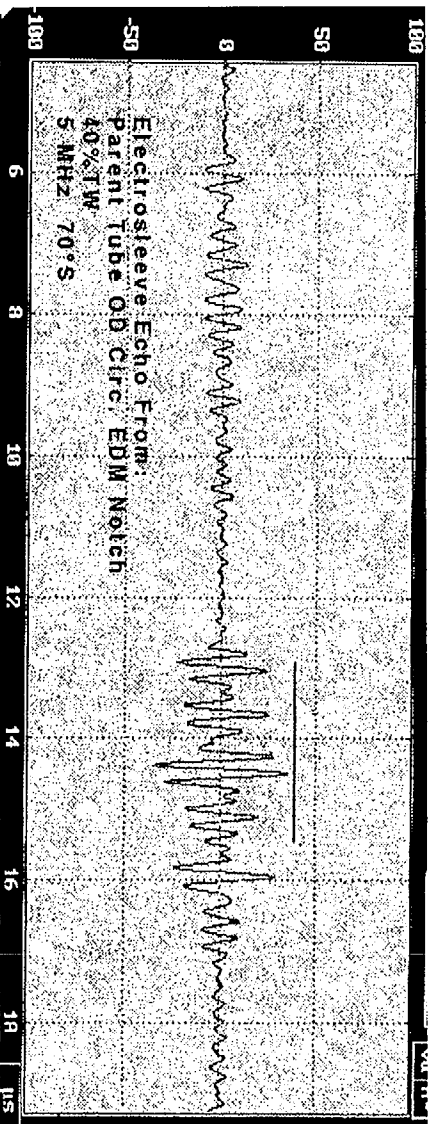
Fig. 5.2. Ultrasonic (top) and EC (bottom) signals from 0.5-mm (0.020-in.)-deep (40% TW) OD circumferential notch in parent metal of electrosleeved tube. Ultrasonic (70° shear) and EC flaw signals are both clear.
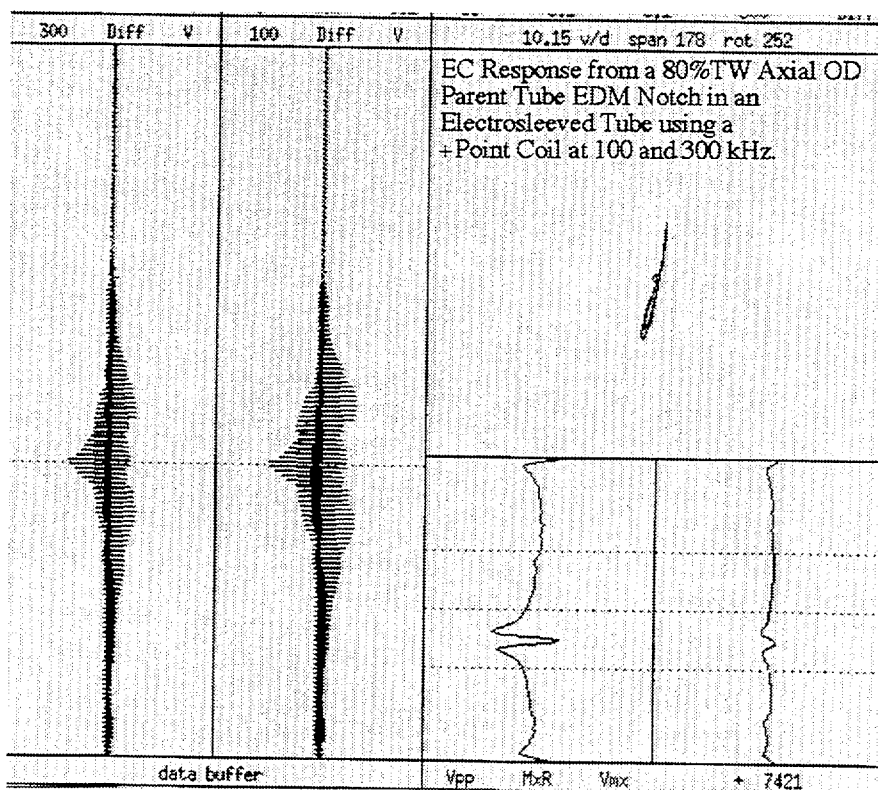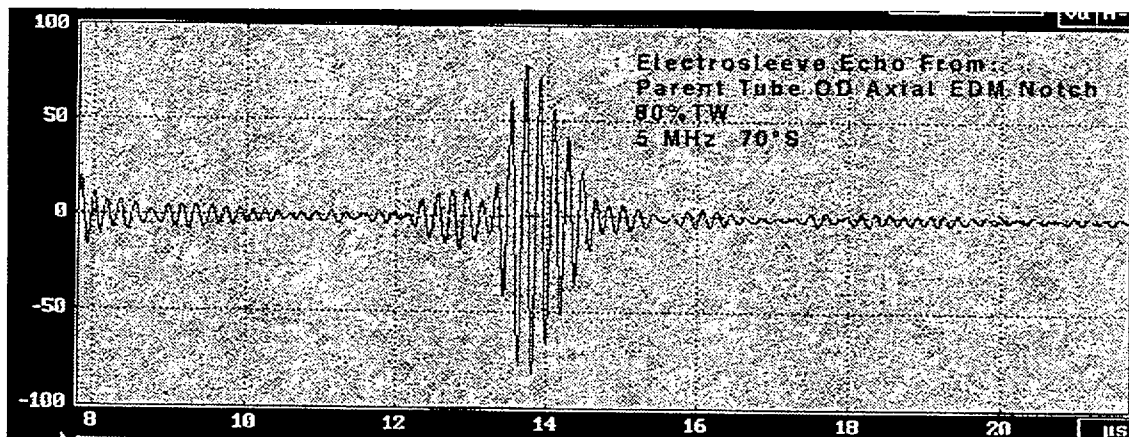
Fig. 5.3.   Ultrasonic (top) and EC (bottom) signals from 1-mm (0.040-in.)-deep (80% TW) OD
axial notch in parent metal of electrosleeved tube. Ultrasonic (70° shear) and EC flaw
signals are both clear.
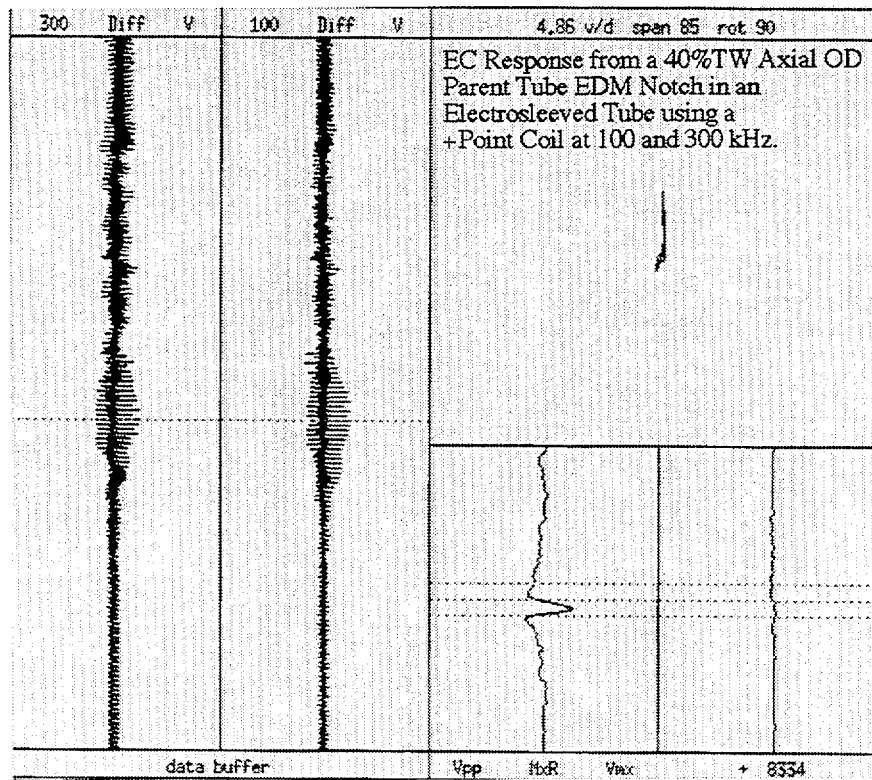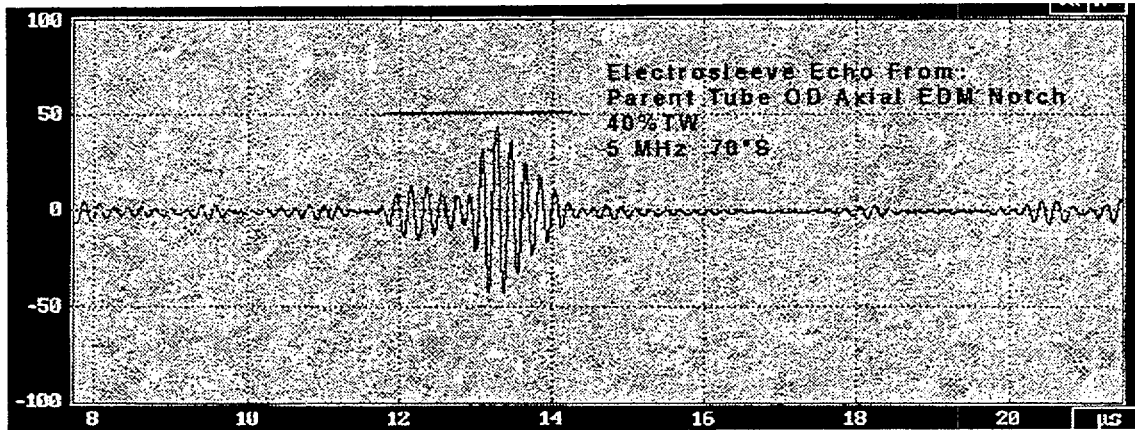
Fig. 5.4. *Ultrasonic (top) and EC (bottom) signals from 0.5-mm (0.020-in.)-deep (40% TW) OD axial notch in parent metal of electrosleeved tube. Ultrasonic (70° shear) and EC flaw signals are detectable but UT signal is better.*

results for a 0.5-mm (0.020-in.)-deep (40% TW) OD axial notch in the parent tube. Ultrasonic (70° shear) and EC flaw signals are both detectable, but the UT signal again has a significantly better S/N ratio. Use of 45° shear waves for axial notches show even better S/N ratios than the 70° shear.

The UT examination of ID cracks (or even notches) in the parent tube that do not extend into the sleeve is desirable to determine the adequacy of detection when a crack does not intersect the parent tube OD to form a strong ultrasonic reflector. Currently, a corner trap is needed to characterize an ID parent tube crack, and an ID parent tube crack would thus have to be 100% TW to be detected. However, while that situation may be the case for a 45° angle beam, the problem may be circumvented by use of 70° angle beams. Higher-angle-beam UT NDE, including use of surface waves, should be explored for detection of cracks that do not form corner reflectors. Possible variations in the acoustic properties of the electrosleeve should also be evaluated because such variations could cause the ultrasonic beam to be distorted, resulting in missed defects or false calls.

The sleeved tubes with EDM notches are useful as references but will not indicate sensitivity to detection of cracks. The intensity of a UT wave reflected from an SCC is considerably lower than that from a notch. The EDM notches may be useful in establishing the limiting case for detection (i.e., an SCC would have to be larger than the smallest EDM notch detectable).

5.1.2 Residual Stress

The Intense Pulsed Neutron Source at ANL has been used to estimate fabrication induced residual stresses in the sleeve and parent material of an electrosleeved Alloy 600 flaw free 30-cm (12-in.)-long 22.2-mm (7/8-in.)-diameter tube. While stresses are expected to be relatively small in these tubes, the experiments are helpful for developing and validating neutron diffraction techniques for determining (under laboratory conditions) bulk stresses in repaired thin wall tubing. In the future, experiments may be carried out on tubes repaired by other techniques.

Neutron diffraction techniques have been applied to determine the strains from which the stresses have been calculated. The strain was determined by measuring the shift of Alloy 600 and nickel diffraction peaks (related to lattice d-spacing) relative to strain-free reference material, which in this case was nickel powder and Alloy 600 without a sleeve. The resolution of the neutron detectors is good enough to separate the diffraction peaks (representing the lattice spacing of various crystallographic planes) for these materials. The d-spacing is determined from Bragg's Law, $2d \cdot \sin\Theta = n\lambda$, where Θ is the angle between incident and scattered beams and λ is the wavelength of the neutrons, which is directly related to the velocity of the neutrons that create the various diffraction peaks. By varying the area of interrogation, as seen in Fig. 5.5 and 5.6, the radial and hoop strains can be determined. The height of the beam is about 4 cm.

In order to estimate the axial and hoop stresses from measurements of strain in the hoop and radial direction, the stress (but not strain) in the radial direction is assumed to be zero (thin-wall tubing assumption). One can then show that for the hoop stress $[\sigma_\Theta]$,

$$\sigma_\Theta = [E / (1+\nu)] [\varepsilon_\Theta - \varepsilon_r],$$

Inconel 600 (1.25 mm wall)

Nickel (1 mm wall)

Incident
Neutron
Beam

Volume of Interrogation

Direction
of Strain
Measurement
(Radial)

Collimator

Scattered
Neutron
Beam

Neutron
Detector

NEUTRON
SPECTRUM

NEUTRON COUNTS

Diffraction peaks from
Inconel

d-SPACING

Diffraction peaks
from nickel
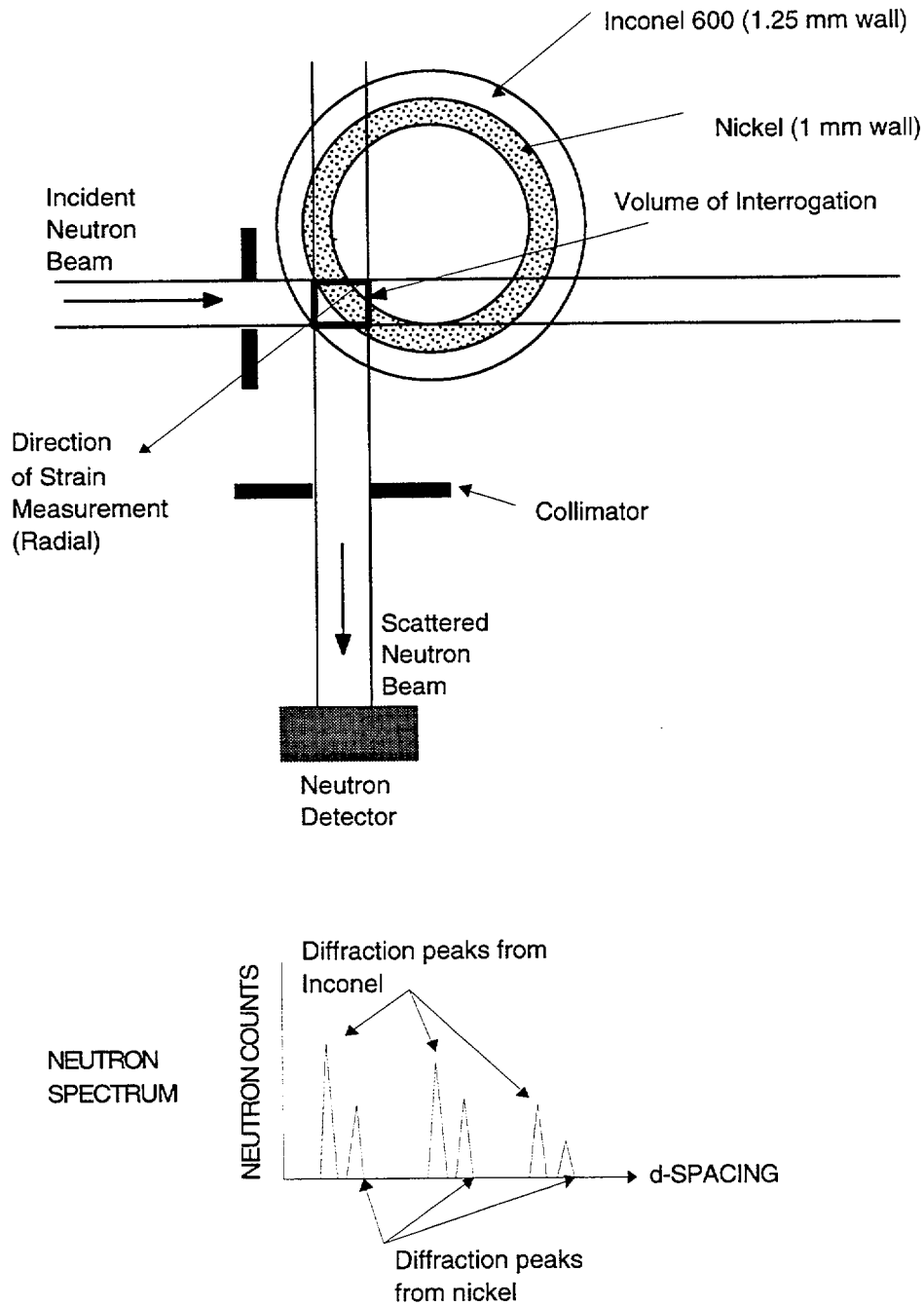
Fig. 5.5.   *Configuration of incident and scattered neutron beam from ANL IPNS used to simultaneously measure bulk* radial *strain in Alloy 600 parent tube and nickel sleeve. The diffraction peaks of nickel and Alloy 600 are easily separated, allowing strain relative to a reference to be determined.*
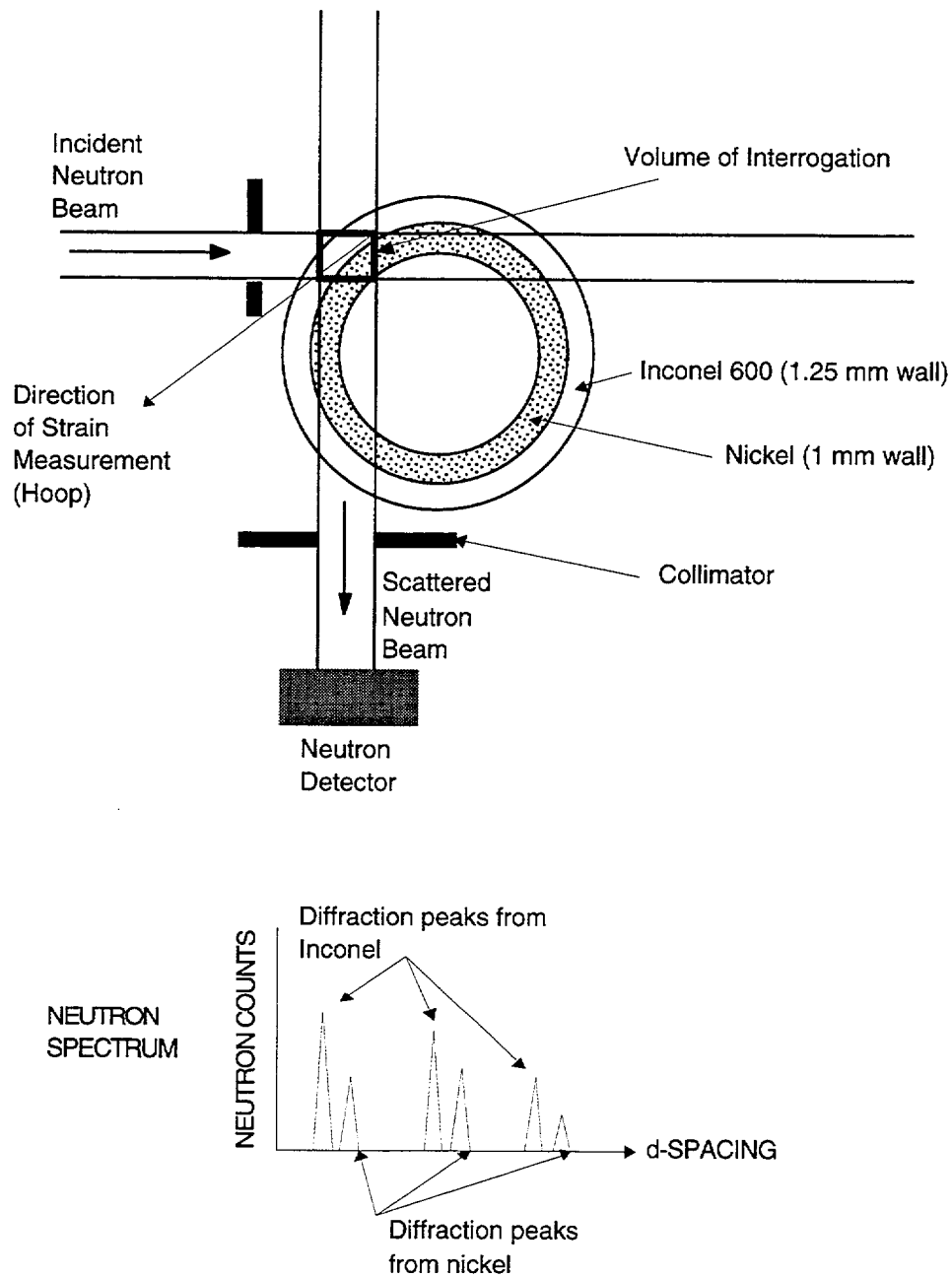
Fig. 5.6. *Configuration of incident and scattered neutron beam from ANL IPNS used to simultaneously measure bulk hoop strain in parent tube and nickel sleeve. The diffraction peaks of nickel and Alloy 600 are easily separated, allowing strain relative to reference material to be determined.*

and for the axial (z) stress $[\sigma_z]$

$$\sigma_z = - [E /(1+\nu)] [\varepsilon_\Theta + \varepsilon_r/\nu],$$

where E is the modulus of elasticity, ν is the Poisson ratio, ε_Θ is the hoop strain, and ε_r is the radial strain.

Examination of the relative amplitudes of various peaks, compared to the isotropic case, revealed texture in both the Alloy 600 parent tube and nickel sleeve. As a result, the shift of the (220) line was used to determine the hoop and radial strains in the Alloy 600 tube and the radial strain in the nickel sleeve, and the average of the four largest peaks was used to determine the hoop strain in the nickel sleeve. The results of strain measurements and calculated stresses are provided in Table 5.1.

Compressive hoop and axial residual stresses of approximately 100 MPa (14.5 ksi) in magnitude, with relatively large uncertainties, were calculated for the Alloy 600 parent tube material. Tensile residual stresses of $\approx$100 MPa (14.5 ksi) were calculated for the nickel sleeve material with similar uncertainties.

5.2 Normal Incident Ultrasonic NDE

An experiment with an electrosleeved tube was carried out to answer the question of whether a normal incidence longitudinal ultrasonic wave would reflect from the electrosleeve/parent-tube interface. A detectable echo from the interface would allow sleeve thickness to be determined and provide a reference for characterizing the depth of detectable cracks in either the parent tube or electrosleeve. Brief experiments with normal incidence longitudinal ultrasonic waves at about 10-15 MHz showed no discernible echo from the interface. In another experiment, the normal incidence longitudinal velocity of sound was measured in an electrosleeved Alloy 600 22.2-mm (7/8-in.)-diameter SG tube section to establish the impedance mismatch across the electrosleeve/parent material interface. Figure 5.7 shows the geometry of the tube on which the measurements were made and the data acquired. A 15 MHz longitudinal wave transducer with standoff was used in a pulse echo mode to make these measurements. The results are summarized in Table 5.2. The relative acoustic impedance is the acoustic impedance (Z) of the material of interest divided by the acoustic impedance of water, where Z = density x velocity and $V_{(H_2O)}$ = 1500 m/s.

The ultrasonic echo reflection coefficient at the electrosleeve/Alloy 600 tube interface is given by

$$R = (Z_{sleeve} - Z_{Alloy\ 600})/(Z_{sleeve} + Z_{Alloy\ 600}).$$

The reflection coefficient at the Ni/Alloy 600 interface is $\approx$5%, and, as a result, the echo from the Ni/Alloy 600 mismatch would be extremely difficult to detect, if at all. Sophisticated signal processing and deconvolution techniques would have to be applied to the ultrasonic data to reveal echoes from the Alloy 600/nickel interface.

Table 5.1.   *Hoop and axial residual strains determined from neutron diffraction data acquired at Argonne's Intense Pulsed Neutron Source and residual stresses calculated from strain data for an electrosleeved Alloy 600 30-cm (12-in.)-long tube.*

		Elastic Modulus (GPa)	Poisson's Ratio	Hoop Strain	Radial Strain	Hoop Stress (MPa)	Axial Stress (MPa)
Alloy Parent Tube	6	206	0.28	-0.00039	0.00028	-110±50	-97±50
Nickel Sleeve		201	0.31	0.00024	-0.00036	94±50	137±50

```
                                                            Alloy 600
  ↑    _____
  |    _____
  |         ↑              _____▁▁▁▁▁▁▁▁▁▁▁▁▁▁▁▁_____
  |         |             /▓▓▓▓▓▓▓▓▓▓▓▓▓▓▓▓▓▓▓▓▓▓▓▓▓▓\           Nickel Electrosleeve
22.23 mm  19.75 mm    ↑  ▓▓▓▓▓▓▓▓▓▓▓▓▓▓▓▓▓▓▓▓▓▓▓▓▓▓▓▓
  |         |       17.87 mm
  |         |          |  ▓▓▓▓▓▓▓▓▓▓▓▓▓▓▓▓▓▓▓▓▓▓▓▓▓▓▓▓
  |         ↓          ↓  \▓▓▓▓▓▓▓▓▓▓▓▓▓▓▓▓▓▓▓▓▓▓▓▓▓▓/
  |    _____↑▗_____↑▗_____
  ↓    _____▜_____▜_____
```

Round Trip   Round Trip
Transit Time   Transit Time
for Ultrasonic   for Ultrasonic
Echo through   Echo through
Parent Tube   Parent Tube
and Sleeve: Only:

t = 0.740 μs   t = 0.406 μs
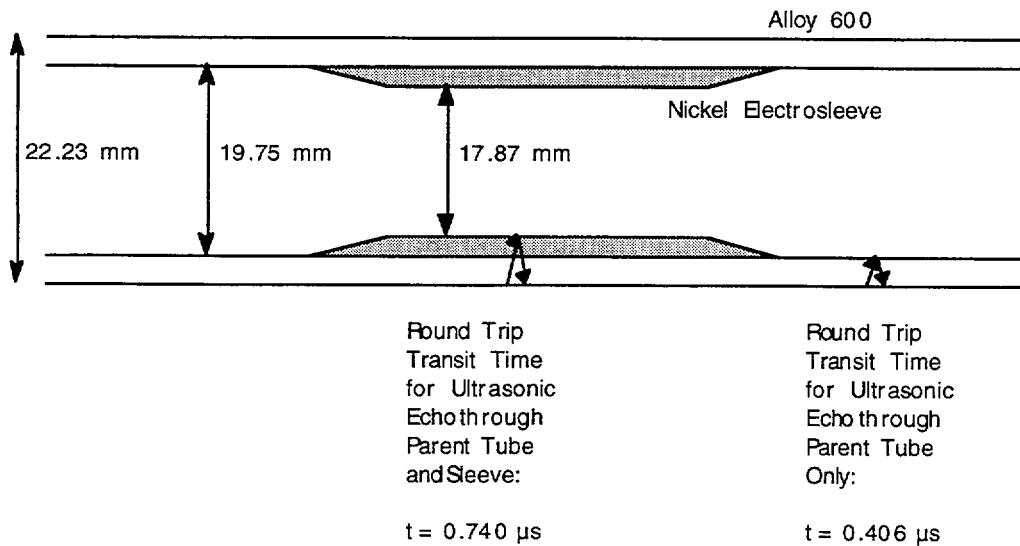
Longitudinal Velocity of Sound (Alloy 600) = (22.23 - 19.75)/ (0.406) = 6110 m/s

Longitudinal Velocity of Sound (Nickel Sleeve) = (19.75 - 17.87)/ (0.334) = 5630 m/s

Fig. 5.7.   *Schematic drawing showing dimensions of tube used to measure longitudinal velocity of sound (radial direction of propagation) for Alloy 600 parent tube and nickel electrosleeve, and backwall echo transit times for ultrasonic waves launched from OD of tube.*

Table 5.2.   *Density, longitudinal velocity of sound, and relative acoustic impedance of Alloy 60☐ and nickel*

Material	Density (gm/cm^3)	Longitudinal Velocity of Sound (m/s)	Relative Acoustic Impedance (Z/Z$_{H2O}$)
Alloy 600	8.47	6110	35
Nickel	8.86	5630	33

5.3 Review of Corrosion Resistance of Electrosleeve Material

A comprehensive critical review of the corrosion and cracking behaviors of tubes repaired by the electrosleeve process developed by Ontario Hydro Technologies was completed during the reporting period. The corrosion and stress corrosion cracking behaviors of pure Ni, nanophase Ni and Ni-P alloys, and selected commercial Ni-base alloys were reviewed for a variety of water chemistries, with emphasis on the steam generator operating environment. In particular, corrosion tests conducted by Framatome Technologies, Inc., on the electrosleeve material were carefully reviewed. The thermal stability of the nanophase microstructure was also considered.

It was concluded that there are substantial data and experience to indicate that Ni and the nanophase Ni electrosleeve material in particular are highly resistant to corrosion and SCC in a variety of environments. However, the variety and complexity of environments on the secondary side of steam generators makes it very difficult to assert with a high degree of certainty that these materials are immune to cracking in all of these environments. It was also noted that the long-term thermal stability of the nanophase material is not clear, in view of the range of activation energies for grain growth reported in the literature. A final letter report describing the results of this review was sent to the NRC project manager.

References

1. D. R. Diercks, S. Bakhtiari, K. E. Kasza, D. S. Kupperman, S. Majumdar, J. Y. Park, and W. J. Shack, Steam Generator Tube Integrity Program, Semiannual Report, October 1997—March 1998, NUREG/CR-6511, ANL-98/15, Vol. 5, U.S. Nuclear Regulatory Commission, Washington, DC (April 1999).

2. D. R. Diercks, S. Bakhtiari, K. E. Kasza, D. S. Kupperman, S. Majumdar, J. Y. Park, and W. J. Shack, Steam Generator Tube Integrity Program, Annual Report, October 1996 - September 1997, NUREG/CR-6511, ANL-98/15 Vol. 4, U.S. Nuclear Regulatory Commission, Washington, DC (January 1999).

3. R. A. Clark and R. L. Burr, Corrosion, Vol. 36, July 1980, pp. 382-383.

U. S. NUCLEAR REGULATORY COMMISSION

BIBLIOGRAPHIC DATA SHEET

(See instructions on the reverse)

1. REPORT NUMBER
(Assigned by NRC. Add Vol., Supp., Rev., and Addendum Numbers, if any.)

NUREG/CR–6511, Vol. 6
ANL–99/8

2. TITLE AND SUBTITLE

Steam Generator Tube Integrity Program:
Annual Report, October 1997—September 1998

3. DATE REPORT PUBLISHED

MONTH	YEAR
October	1999

4. FIN OR GRANT NUMBER
W6487

5. AUTHOR(S)

D. R. Diercks, S. Bakhtiari, K. E. Kasza, D. S. Kupperman, S. Majumdar, J. Y. Park, and W. J. Shack

6. TYPE OF REPORT
Technical; Annual

7. PERIOD COVERED (Inclusive Dates)
Oct. 1997—Sept. 1998

8. PERFORMING ORGANIZATION – NAME AND ADDRESS (If NRC, provide Division, Office or Region, U.S. Nuclear Regulatory Commission, and mailing address; if contractor, provide name and mailing address.)

Argonne National Laboratory
9700 South Cass Avenue
Argonne, IL 60439

9. SPONSORING ORGANIZATION – NAME AND ADDRESS (If NRC, type "Same as above"; if contractor, provide NRC Division, Office or Region, U.S. Nuclear Regulatory Commission, and mailing address.)

Division of Engineering Technology
Office of Nuclear Regulatory Research
U. S. Nuclear Regulatory Commission
Washington, DC 20555 -0001

10. SUPPLEMENTARY NOTES

J. Muscara, NRC Project Manager

11. ABSTRACT (200 words or less)

This report summarizes work performed by Argonne National Laboratory on the Steam Generator Tube Integrity Program during the period October 1997-September 1998. Under Task 1, progress is reported on the assembly of a steam generator tube mock-up for round-robin studies on nondestructive evaluation (NDE) procedures, on the evaluation of NDE techniques for characterizing the tubes going into the mock-up, and on the development of protocols and procedures for the round-robin. In addition, results are reported on the EC inspection of deplugged tubes obtained from the McGuire Nuclear Station. Under Task 2, results are reported on numerical and experimental results on the response of a bobbin coil probe to axial notches in calibration-standard tubes. Multivariate linear and nonlinear models for the correlation of eddy current data with tube structural integrity are also being evaluated. In Task 3, cracked tubes are being produced for the steam generator tube mock-up. Checkout, shakedown, and performance qualification of the Pressure and Leak-Rate Test Facility are described, and the results of initial tests are reported. In addition, a series of finite-element analyses was conducted for multiple collinear cracks with various ligament widths, a test matrix was developed for the testing of tubes with axial machined notches, a literature survey is being completed on the mechanisms of stress corrosion cracking, and the tubes removed from the McGuire steam generators are being decontaminated. Under Task 4, the results of eddy current and ultrasonic examinations of electrosleeved tubes are reported, and residual stresses in these tubes have been measured by neutron diffraction techniques. The results of a critical review of the corrosion resistance of electrosleeved material are also summarized.

12. KEY WORDS/DESCRIPTORS (List words or phrases that will assist researchers in locating this report.)

Steam Generator
Tubes
Stress Corrosion Cracking
Eddy Current Testing
Nondestructive Evaluation
In-service Inspection
Pressure Testing
Tube Burst
Leak Rate
Alloy 600, Inconel 600

13. AVAILABILITY STATEMENT
Unlimited

14. SECURITY CLASSIFICATION

(This Page)
Unclassified

(This Report)
Unclassified

15. NUMBER OF PAGES

16. PRICE

NRC FORM 335 (2–89)
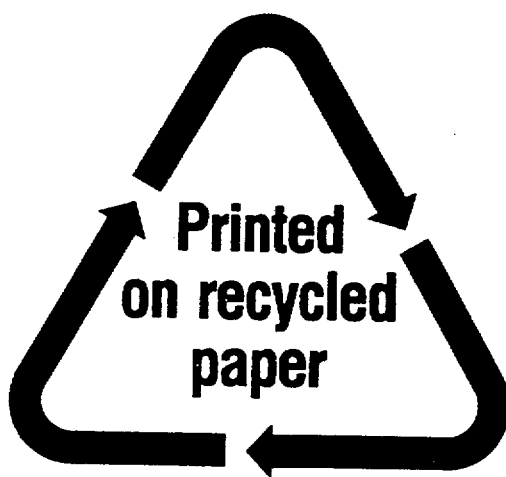
UNITED STATES
NUCLEAR REGULATORY COMMISSION
WASHINGTON, DC 20555-0001

OFFICIAL BUSINESS
PENALTY FOR PRIVATE USE, $300